A study of the fragmentation of quarks in ep collisions at HERA

Paul Dixon, *B.Sc.(Hons)*
Department of Physics, Lancaster University

This thesis is submitted in part fulfillment
of the requirements for the degree of Ph.D
from Lancaster University.

No part of this thesis has been, or will be,
submitted to any other university.

November 5, 1997

Abstract

Low–x deep-inelastic ep scattering data, taken in 1994 using the H1 detector at HERA, are analysed in the Breit frame of reference. The evolution of the peak and width of the fragmentation function is presented as a function of the magnitude of the four-momentum transfer of the exchanged photon (Q) and compared with e^+e^- results at equivalent centre of mass energies. Clear evidence for scaling violations in ep fragmentation functions as a function of Q is shown. Differences between the average charged multiplicity and the multiplicity of e^+e^- annihilations at low energies are discussed.

Contents

List of Figures

List of Tables

Acknowledgements

Where do I start? Firstly, I would like to thank Terry Sloan for phoning me up on a soggy summers day in 1993 and offering me the chance to do a PhD in high energy physics. I would also like to thank Terry for his warmth and guidance along the way. My greatest of thanks must go to Rob Henderson who as well as being my supervisor, managed to keep me smiling these last few years - usually with hilarious Monte-Python impressions. But before I become an ex-student, a few other people also deserve a mention. Thanks to Steve Burke, David Cussans and Michael Kuhlen for pointing me in the right direction and providing me with answers to my questions when I arrived at DESY. Thanks to (Prof.) Graham Thompson and the rest of the BHAG group for letting me in, and special thanks to Dave "hey Paul, I've just discovered another bug in H1PHAN" Kant for pointing out all my 'mistakes'.

I did my best at trying to crash the Lancaster computing cluster, but thanks to Rob and Alex Finch (who must have had the patience of a saint whilst clearing up after me), it was never down for very long. Will I get paid for beta testing DEC's HSM? Thanks to Roger Jones for proof reading this thesis and for not mentioning Dr Who too often. Greetings to Chris Davis and Susan Ketels. I must also mention here David Newton and Arthur Clegg. Thanks to Andrew Betteridge for putting up with me, especially those 10 days in Geneva - I suppose you got your own back by making me watch 'Hard Boiled'. Thank you Doc Jellyfish, your healing powers are amazing.

Dave Sankey, you're a star!

If I don't mention the QMW students here, they'll make my life hell. So greetings to Rob, Keef, Kostas, Martin, Caroline, Dan1, Dan2, Dan3, Dai and John.

Good luck to Gordon - the man with a real job (shudder), and best of luck to the Lancaster students: Phil, Lesley, Paul, Stephen, Nick, Kay (Manchester have been warned) and Mick (whatever you may be doing).

Special thanks go to Mark Williams for saving me from insanity. I'll miss our overly long tea breaks with chip barms and interesting(!) topics of conversation. I hate to use a cliché here, but you're the best.

Miss Golightly. My angled and pointy friend. I'll miss your unique point of view and wry observations (and the way you say pudding). I never did get those photocopied bananas (or that sloe gin).

To keep a tradition going, I must thank Paul Colrain for the Orange joke, and hope that he doesn't get into too much trouble on his travels around the globe.

I acknowledge the Particle Physics and Astronomy Research Council (PPARC), formerly known as the Science and Engineering Research Council (SERC), for their financial support.

Apologies to anyone I've missed.

Finally, I would like to thank my parents for all their love and support.

Preface

The purpose of this thesis is to compare the properties of fragmentation functions of the struck quark in deep inelastic scattering in the current region of the Breit frame to the fragmentation functions of quarks that are pair produced in e^+e^- interactions. Via the modified leading log approximation (MLLA), the ep fragmentation functions will be used as a test of perturbative QCD.

Chapter one introduces HERA and the H1 detector, focussing on the detector components used in this analysis. Chapter two gives an overview of the physics processes that occur at HERA. Chapter three gives a brief introduction to QCD and discusses elements of Monte-Carlo models along with the necessary theoretical background relevant to this analysis. Chapter four covers the selection of DIS events and investigates various methods by which DIS event kinematics are reconstructed. The boost to the Breit frame is discussed in chapter five and chapter six describes the method employed to acceptance correct data. The properties of the fragmentation function in the current region of the Breit frame as a function of Q are presented in chapter seven along with an account of systematic uncertainties.

Chapter 1

HERA and the H1 Detector

1.1 The HERA Collider

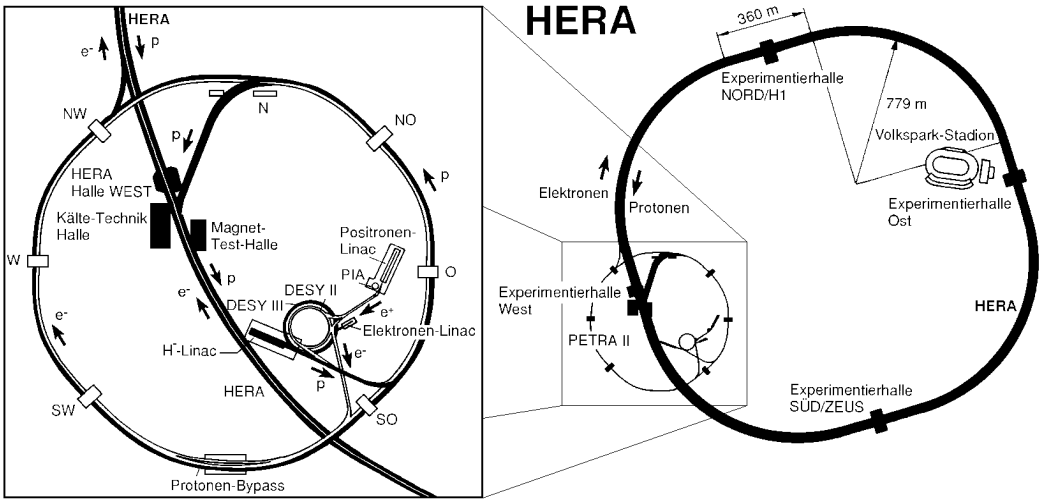

Figure 1.1: *The HERA collider.*

The electron-proton colliding beam facility HERA [3] consists of two independent accelerators designed to store 820 GeV protons and 30 GeV electrons respectively and to collide the two counter-rotating beams head-on at four interaction points spaced uniformly around its 6.3 km circumference. The overall layout of HERA, including pre-accelerators used to inject electron and proton beams into HERA,

is shown in Figure 1.1.

For the majority of the 1994 run period, positrons were used instead of electrons to reduce background due to positive ions in the beam pipe.

Electrons (positrons) are injected into a small storage ring from a 500 MeV linear accelerator. They are accumulated in a 60 mA single bunch and injected into DESY II where they are accelerated to 7 GeV and transferred to the modified PETRA II ring. This stage is repeated at a rate of 12.5 Hz until PETRA II has been filled with 70 bunches each approximately 28.8 metres apart. The bunches are then injected into the HERA main ring. The procedure is repeated two more times until there are 210 bunches in the main ring.

A new chain of pre-accelerators was built in order to inject protons into HERA. A 50 MeV linear accelerator is used to strip negatively charged hydrogen ions of their electrons and inject produced protons into DESY III. Here the protons are accelerated to 7 GeV and then transferred to PETRA II, where they are accelerated to 40 GeV before the final injection into the HERA ring.

To detect collisions between electron and proton bunches, two detectors, H1 [4] and ZEUS [5] have been built. As can be seen from Figure 1.1, the H1 and ZEUS detectors are located at the North and South halls respectively. A third experiment, HERMES [6] is situated at the East hall and a fourth experiment, HERA-B [7] is situated at the West hall. HERMES will study collisions between polarised electron and atomic beams thus enabling measurements to be made of the polarised nucleon structure functions [8]. HERA-B is an experiment to study CP violation in the B system using an internal wire target around the proton beam.

1.2 Overview of the H1 Detector

In the following sections, an overview of the H1 detector and its components will be given. A more detailed description can be found in reference [4].

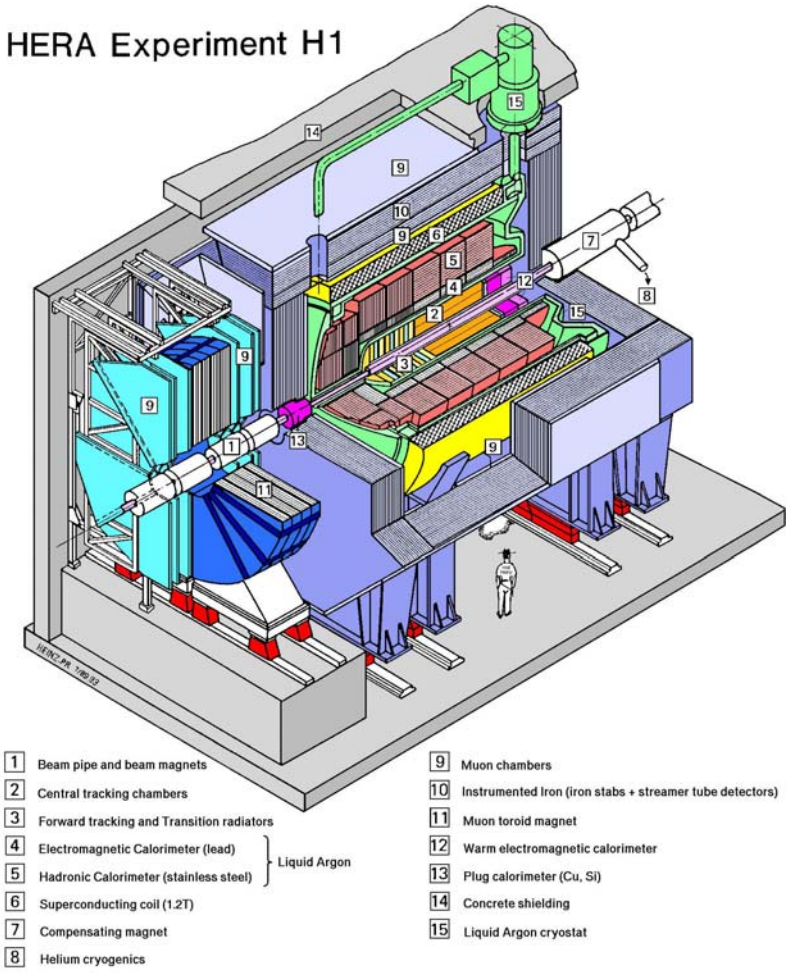

Figure 1.2: *A 3D view of the H1 Detector.*

1.3 Tracking

The H1 tracking system shown in Figure 1.3 has been designed with several aims. It must be able to cope with the high particle densities of the hadronic final state (particularly at small angles to the beam pipe) being able to reconstruct tracks with high efficiency and good momentum resolution even in dense multi-track environments. It must also provide a trigger system to suppress the high background, along with a fast event vertex determination. Multiwire proportional chambers exist which remove some of the background - they are discussed sepa-

rately in the following sections.

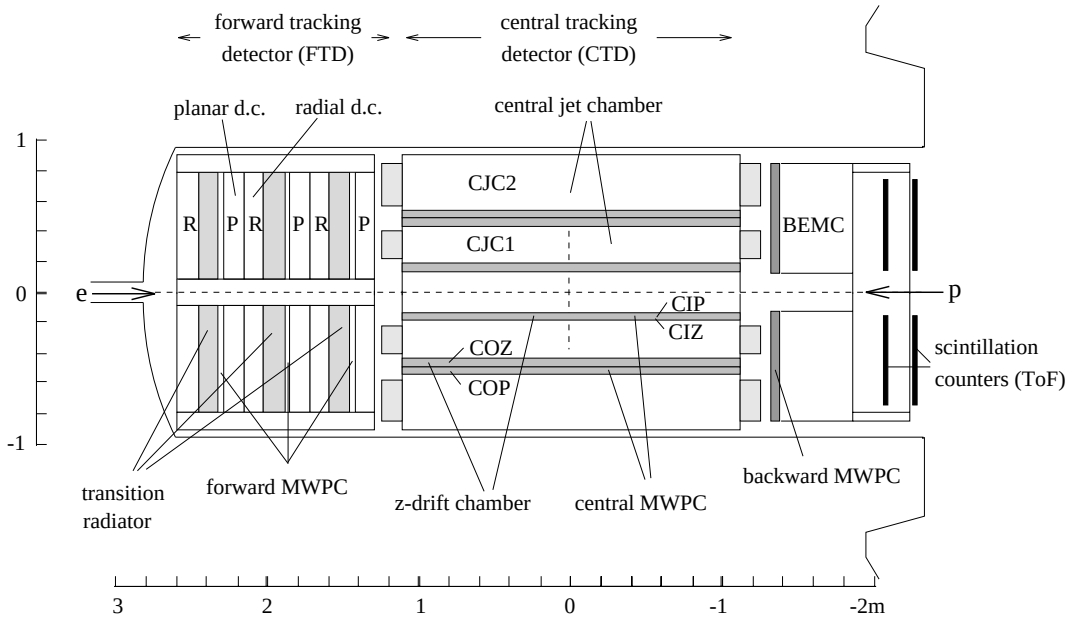

Figure 1.3: *The H1 Tracking system.*

1.3.1 The Central Tracking Detector

The central tracking detector completely surrounds the interaction region. It is designed to detect charged particles leaving the nominal interaction vertex over a polar angular range $25^\circ < \theta < 155^\circ$, as well as being used for triggering purposes. It is dominated by two large concentric jet chambers, the inner, CJC1 (200 mm $< r <$ 453.5 mm) and the outer, CJC2 (527 mm $< r <$ 843 mm), the design of which is based on the jet chambers of the JADE experiment formerly at the PETRA accelerator. Both the sense wires (or anode wires) and the field wires, which create and shape the uniform drift field of the two chambers are strung parallel to the z direction (the beam axis). In a view perpendicular to the z (beam) direction, these wires are arranged along radial spokes which curve away from the radial direction with increasing radius, Figure 1.4. Several advantages result from this, the most important one being that the chance of a track passing through both of the central jet chambers undetected is greatly diminished (resolving left-right ambiguities). Also, high momentum tracks will cross sense

wire planes in both of the central jet chambers allowing the particle (or bunch) crossing time to be accurately determined (t_o ~0.5 ns), enabling the tracks coming from different bunch crossings to be separated. Another advantage of this design is its ability to resolve the left-right ambiguity of a track.

The chamber has a track measurement resolution, in the $r-\phi$ plane, of $\sigma_{r\phi}$ =150 μm. The central chamber longitudinal (or z) coordinate resolution is limited, as the measurement is done by charge division. σ is of the order of 1% of the wire length, making $\sigma_z \approx 2-2.5$ cm for this sub-detector. However, this is sufficient to give a link to the central inner, CIZ (173 mm $< r <$ 193 mm, $16^\circ < \theta < 169^\circ$) and outer, COZ (456 mm $< r <$ 480 mm, $25^\circ < \theta < 156^\circ$) z drift chambers which, as the names suggest, have a wire configuration to provide an accurate z–coordinate for a passing charged particle.

As one of the main design aims of the tracking detectors is to minimise the construction material, to reduce the number of secondary interactions with the sub-detector walls, the CIZ and COZ share their 'housing' with their sub-detector neighbours. The CIZ and COZ also provide an approximate ϕ–coordinate for a passing charged particle. Their location, next to CJC1 and CJC2, means that these two sets of sub-detectors can be used for mutual calibration purposes.

The CIZ is a polygon ring arrangement, with 17 regions in ϕ. There are 15 rings along z, each of length 12 cm. The 4 sense wires are arranged along lines inclined at 45° to the chamber axis. These lines point back to the interaction region so forward of this region they slope forwards and backwards of this region they slope backwards. Tracks from the interaction point will then travel along these wire planes. However, because of the arrangement of ISO-crones, it will only give hits on 3 of the 4 wires. The left/right ambiguity is resolved by knowing which 3 wires data appears on. The z measurement resolution is $\sigma_z \approx 320$ μm for the polar range $20^\circ < \theta < 170^\circ$.

The COZ is also a polygon ring, but with 24 regions in ϕ - there are 24 rings each of length 9 cm. As with the CIZ, this chamber also has 4 sense wires.

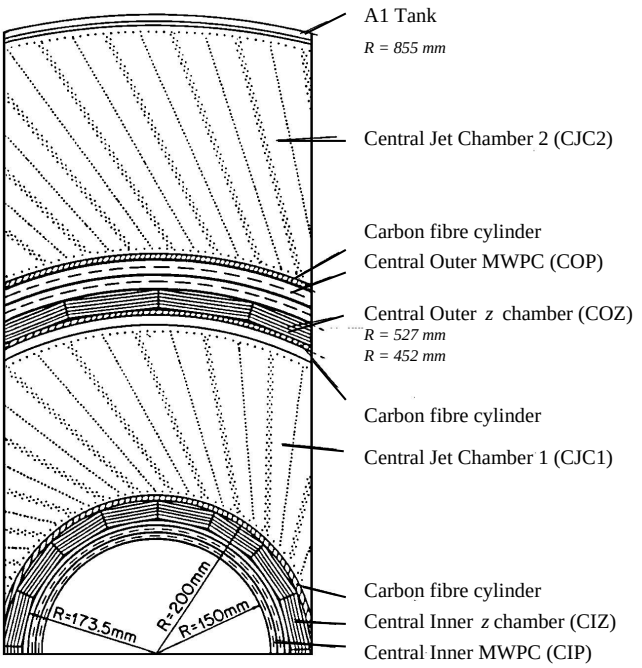

Figure 1.4: *Cross-section through the central track detector.*

However, given its radial distance from the beam axis and its reduced polar angular coverage, tracks will pass at a greatly increased angle than that found in the CIZ. For this reason the sense wires are strung around the chamber at a constant z–coordinate. There is no wire stagger and left/right ambiguities are removed in software. The point resolution depends on the angle of the particle as it crosses the COZ. The maximum resolution, obtained for a polar angle of 90° is $\sigma \approx 200$ μm, but it deteriorates to $\sigma \approx 500$ μm for low crossing angles.

The central tracker has two sets of proportional chambers, an inner, the CIP, located inside CJC1 and an outer, the COP, located between CJC1 and CJC2. The CIP, which is the sub-detector closest to the interaction region, consists of a double layer of proportional chambers. The inner layer is rotated by 22.5° relative to the outer and effectively produces a 16-fold segmentation in ϕ. A base width time resolution, determined using cosmic events, is ≈ 75 ns. The COP follows a similar design to the CIP.

Combinations of the CIP, COP and forward tracking detector (FTD) can be used to reconstruct the event vertex. The track information, using this vertex coordinate, can then be used together with calorimeter information.

1.3.2 The Forward Tracking Detector

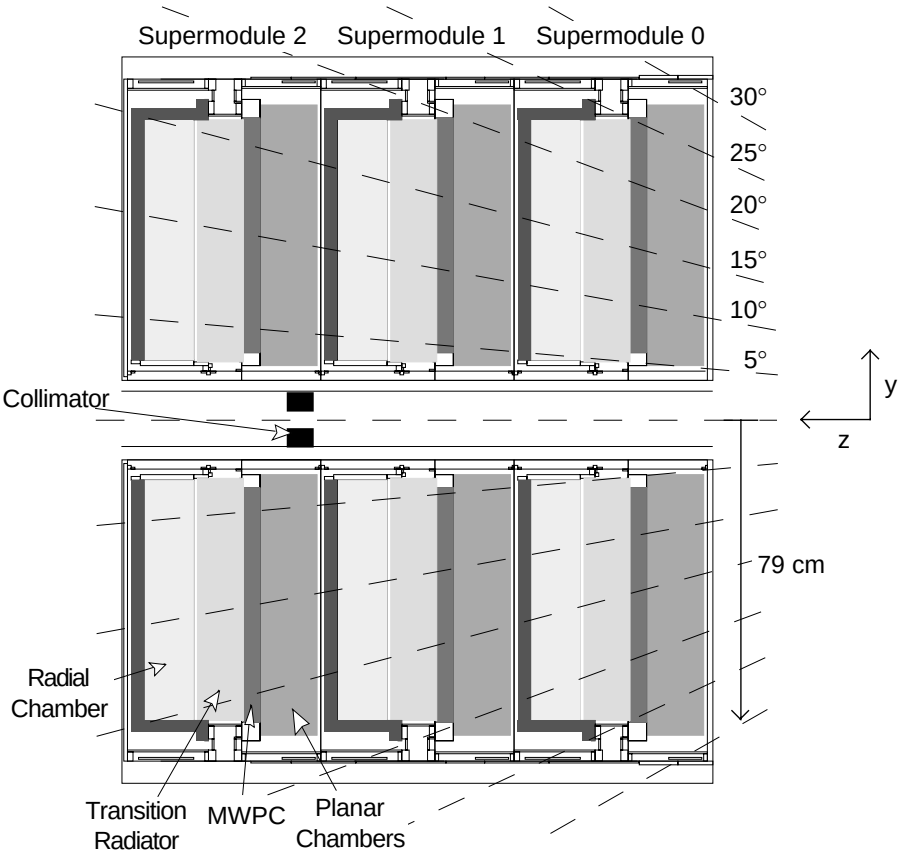

Figure 1.5: *The Forward Tracking Detector.*

The H1 Forward Tracking Detector, shown in Figure 1.5, covers the laboratory angles between 5° and 30° with respect to the proton beam direction. The sensitive region of the chambers is the cylindrical volume 134 cm $< z <$ 254 cm, and 15 cm $< r <$ 79 cm. This region is a particularly hostile environment for tracking. The primary track multiplicity (typically from low momentum products from fragmentation of the proton), is ∼10-15 and is strongly concentrated at small radii. In addition, material in the end wall of the CTD and around the

beam pipe produces a large number of secondary tracks.

The detector is realised as three identical sub-units, known as Super-modules, numbered 0 to 2 with increasing z. Each Super-module, when seen from the direction of the incoming proton, consists firstly of three layers of Planar drift chambers ($\sigma_{x,y} \approx 160\mu$m), oriented at 0°, +60° and -60° to the vertical, followed by a multi wire proportional chamber (FMWPC), then transition radiator material, and finally a Radial drift chamber (σ_R ~2 cm). Three independent and different gas mixtures are required - one per super-module.

The drift chambers have different wire geometries - the planars contain parallel wires whereas the radial wires radiate outwards from the beam pipe - all have wires strung perpendicular to the beam direction. The FMWPC's contain two planes of pad readout, a coincidence of which provides a fast ($\Delta t < 96$ ns) signal for bunch crossing timing and triggering purposes. After the FMWPC the particles traverse a transition radiator consisting of 400 polypropylene foils contained in its own gas volume. The transition radiation photons after passing through a thin mylar window are detected in the radial chamber which produces up to 12 accurate space track points from ionisation drift timing and charge division. To ensure that a track does not travel along a wire (cathode) plane in all three modules, the second and third radial modules are rotated by 3.75° and 2.5° (1/2 and 1/3 of a wedge) relative to the first. The interleaving of planar and radial chambers provides the optimum lever arm for momentum measurement.

1.3.3 The Backward Proportional Chamber

The Backward Proportional Chamber (BPC), is located in front of the Backward Electromagnetic Calorimeter (BEMC) and covers the polar angular range $155.5° < \theta < 174.5°$. Its most important tasks are to detect the scattered electron in low Q^2 DIS events and to aid e/γ discrimination.

The BPC has four wire planes, oriented vertically, horizontally and at ±45°. Hits on three of the four wire plans are required in coincidence with the BEMC, after

which the BPC, in conjunction with the reconstructed event vertex, can provide the scattering angle of the DIS electron with a systematic error of less than 2 mrad.

1.4 The H1 Magnet

The H1 magnetic field is provided by 4 super-conducting solenoids. They are situated outside the electromagnetic and hadronic calorimeters, which requires that they have a diameter of ∼6m.

The main elements are an aluminium clad super-conductor, wound on an aluminium former to support the large electromagnetic forces produced. The super-conducting material is a form of Niobium Titanium composite bound in copper. The closed iron structure, with its octagonal barrel and flat end-caps, serves as a flux return for the magnetic field. This field produces a force on each end-cap of the order of 1500 tonnes. A mapping of the magnetic field has shown that the central field (which is axial to the beam direction) is 1.15 Tesla and varies by less than 3% over the sensitive tracking region. The yoke is laminated and interleaved with plastic streamer tubes, which act as a 'tail catcher' for the hadronic calorimeter and also a muon detector system.

1.5 Calorimetry

The H1 detector was designed to provide clear identification and precise measurement of electrons, muons and penetrating neutral particles together with very good performance in the measurement of jets with high particle densities. To this end, the H1 detector contains a Liquid Argon (LAr) calorimeter covering a polar angle of $4^\circ < \theta < 153^\circ$ and a lead scintillator backward electromagnetic calorimeter (BEMC) covering a polar angle of $150^\circ < \theta < 177^\circ$. Complementing the LAr and the BEMC is a forward plug calorimeter in the proton direction

$\theta \leq 4°$, and a 'tail catcher' calorimeter to measure hadronic 'leakage' from the LAr and BEMC.

1.5.1 The Liquid Argon Calorimeter

The Liquid Argon calorimeter is subdivided into an inner electromagnetic section with lead plates and an outer hadronic section with stainless steel plates as absorbers. The total depth of the calorimeter varies between 4.5 and 8 absorption lengths (λ_I). The calorimeter was optimised for a precise measurement and identification of electrons and for stable energy calibration for electrons and hadrons. The energy resolution σ_E/E for electrons is $12\%/\sqrt{E} \oplus 1\%$ and $45\%/\sqrt{E} \oplus 1\%$ for charged pions as measured with test beams. Throughout this thesis, all energies expressed in resolution formulae are in GeV.

The hadronic energy measurement is performed by applying a weighting technique in order to account for the non-compensating behaviour of the calorimeter. The electromagnetic energy scale is known to a precision of 3%, a result obtained by comparing the measured track momentum of electrons and positrons with their corresponding energy deposition in the LAr calorimeter. The overall calibration of the hadronic energy is presently known to 6%, as determined from studies of transverse momentum balance in deep inelastic scattering (DIS) events.

1.5.2 The Backward Electromagnetic Calorimeter

The primary task of the Backward Electromagnetic Calorimeter (BEMC) is to trigger and measure scattered electrons in DIS events having a Q^2 value ranging from 5 to 100 GeV^2. In addition, the BEMC has to contribute to the measurement of hadronic material emerging from photo-production and medium to low-x, high-y hadronic final states. A description of the variables Q^2, x and y relevant for DIS kinematics is discussed in chapter 2.

The BEMC consists of 88 multi-layer lead-scintillator sandwich stacks, each with

a depth of 22.5 electromagnetic radiation lengths (X_0) corresponding to about 0.97 interaction lengths.

The energy resolution of the BEMC due to sampling fluctuations is $10\%/\sqrt{E}$. The average noise per stack was measured to be 150 MeV which implies that the noise contribution to the measurement of a typical scattered electron shower is about 450 MeV [4, 11]. The resolution is further affected by stack to stack inter-calibration estimated to be around 4%. Thus, for an electron the BEMC resolution can be expressed as:

$$\frac{\sigma_E}{E} = \frac{\sigma_{noise}}{E} \oplus \frac{\sigma_{sampling}}{\sqrt{E}} \oplus \sigma_{constant} \tag{1.1}$$

where $\sigma_{noise} = 0.45$, $\sigma_{sampling} = 0.1$ and $\sigma_{constant} = 0.04$.

The BEMC resolution is further subjected to a calibration uncertainty of 1.7%. The energy calibration can be checked by comparing the measured scattered electron energy with the derived energy using the angle of the electron and the angle of the momentum vector of the hadronic final state [12].

About 30% of all hadronic flow into the BEMC will not produce signals above threshold due to the low interaction length of the device. The hadrons which do interact typically deposit about 30% of their energy in the BEMC. By combining energy measurements in the BEMC and the instrumented iron, a hadronic energy resolution of about $80\%/\sqrt{E}$ is predicted from detailed simulation studies.

1.5.3 The Plug Calorimeter

The plug calorimeter (PLUG) has been designed to close the gap of acceptance for the energy flow measurements between the beam pipe ($\theta \approx 0.6^\circ$) and the forward part of the LAr ($\theta \approx 3^\circ$). It's main task is to minimise the missing part of the total transverse momentum due to hadrons emitted close to the beam pipe, which is important for charged current interactions where the event kinematics can only be determined from the hadronic final state. In addition, the energy emitted into a narrow cone around the beam pipe can can be used to separate the proton jet

as well as to veto beam gas and beam wall background.

The plug consists of 9 layers of copper absorber interspersed with 8 layers of silicon detectors. The total depth of the plug is roughly $4.3\lambda_I$.

The energy resolution for the plug is $150\%/\sqrt{E}$ which is determined by the poor shower containment, both longitudinally and laterally, and course energy sampling. Data taken by the plug calorimeter is not used in any part of the physics analysis presented in this thesis.

1.5.4 The Instrumented Iron (Tail Catcher)

One of the uses of the iron return yoke is to measure the hadronic energy flow leaking out of the LAr calorimeter, hence it is usually termed the (hadronic) tail catcher. It is also used for hadronic detection in the backward region, behind the BEMC as well as muon detection.

In order to meet these requirements the iron yoke is instrumented with streamer tubes and readout pads placed in the gaps of alternating layers of iron. The streamer tubes and the readout pads are orientated along the beam axis in the barrel region $25^\circ < \theta < 130^\circ$ and vertically in the forward and backward regions. The tail catcher covers the angular region $5^\circ < \theta < 175^\circ$ and has a depth of about 4.5 λ_I . The hadronic energy resolution of the tail catcher has been measured as $150\%/\sqrt{E}$.

1.6 The Forward Muon Detector

In addition to the streamer tube system (described in section 1.4) which provides muon detection in the central and backward region, further muon detection is required in the forward region. The forward muon spectrometer is located in H1 to measure high energy muons in the polar angular region $3^\circ < \theta < 17^\circ$ and in the momentum range 5-200 GeV. Muons with momenta less than 5 GeV are

detected in the forward tracker. The resolution achieved is $\frac{\delta p}{p} \approx 30\%$.

This sub-detector consists of two sets of drift chamber planes, 1 set mounted either side of a 1.2m thick toroidal magnet. Each set consists of two outer polar (θ) angle drift planes, which provide the momentum of the muon traversing the chambers, and one inner ϕ plane.

1.7 Luminosity System and Electron Tagger

The luminosity is determined from the rate of Bethe-Heitler events $ep \to ep\gamma$ which have a large and precisely calculable cross section [13]. The main source of background is bremsstrahlung from the residual gas in the beam pipe, $eA \to eA\gamma$ which has a larger cross section and an almost identical signature. The background is measured experimentally using electron and proton pilot bunches. The luminosity is calculated as:

$$\mathcal{L} = \frac{R_{tot} - (I_{tot}/I_0)R_0}{\sigma_{vis}} \tag{1.2}$$

where R_{tot} is the total rate of the bremsstrahlung events, R_0 is the rate from the electron pilot bunches, I_{tot} and I_0 are the corresponding electron beam currents and σ_{vis} is the visible part of the $ep \to ep\gamma$ cross section, taking into account the acceptance and the trigger efficiency of the whole system. The luminosity monitor detects scattered electrons and outgoing photons in coincidence. Therefore it contains two arms, the electron tagger (ET) and the photon detector (PD). The detectors are situated close to the beam pipe and very far away from the interaction region because the angular distribution for both the electrons and the photons are strongly peaked in the direction of the primary e-beam. At 30 GeV the polar angles are of the order of $\theta \simeq \mathcal{O}(m/E) \simeq 17$ μradians. The general view of the luminosity system is shown in Figure 1.6. The ET and PD are situated at z = -33 m and z = -103 m, respectively.

The scattered electrons are deflected into the ET by a set of warm quadrupoles and a bending magnet located in the region -5.8 m $< z <$ -23.8 m. The photons

leave the beam pipe via the photon exit window at z = -92.3 m where they enter the photon tagger.

1.8 Time-of-Flight Counters and The Veto Wall

The scintillator arrays discussed in this section are located in the backward region of the detector and are designed to reject background associated with proton beam interactions at the first level trigger.

The time of flight device (ToF) is located upstream of the interaction region at $z \approx$ -2 m. This position represents a compromise between good coverage of the detector and time resolution. The mean separation of particles from proton background and those from ep collisions at this point is $\sim$ 13 ns. ToF is a hodoscope consisting of two walls mounted perpendicular to the beam pipe. Each wall consists of 3 cm plastic scintillator sandwiched between 6.5 mm ($1.1X_0$) of lead. The lead absorber both protects the scintillator from damage and limits the number of triggers from synchrotron radiation.

The ToF is readout by 24 photo-multiplier tubes. These signals are discriminated and strobed in three time windows: background, interaction and global. A trigger signal is sent to the central trigger logic (CTL) if a logical OR between the two walls in any of the three time windows gives a coincidence. Most important is the background trigger which is used to suppress triggers from other sub-detectors, leading to an overall 99% decrease in the overall trigger rate, and subsequent reduction in dead-time. The interaction and global ToF signals are used in conjunction with other trigger elements to form physics and cosmic ray triggers [14]. The total time taken for a trigger decision to reach the CTL is 250 ns. The device as a whole has a time resolution of 4 ns, while individual counters have a resolution of the order of 2 ns. In addition to the ToF device two double scintillator veto walls are installed at a distance of z = -6.5 m (large veto wall) and z = -8.1 m (small veto wall).

1.9 Triggering and Data Acquisition

Collecting the data from H1 is an enormous task due to the complexity of the detector and the short bunch crossing interval. The time between successive bunch crossings at HERA is about 96ns. However, the time required to read out the information from all the detector components is much longer than this. In order to make efficient use of the available luminosity it is necessary to initiate the complete readout of the detector (a process which takes of the order of 1 ms) only when it is probable that an ep collision has occurred.

The number of analogue readout channels totals over a quarter of a million, and this results in nearly 3Mbytes of raw information for a triggered event. Consequently, various levels of triggering, filtering and data compression are necessary to reduce the average event size to 50-100Kbytes, at a rate of around 50Hz.

Full descriptions of the triggering/filtering and data acquisition systems are found in a number of references [15].

1.9.1 The H1 Trigger

The overall triggering/filtering levels can be seen schematically in Figure 1.7. At each successive level the criteria used to select the desired events increase in sophistication.

The level 1 trigger system (L1) is a purpose–built hardware system. It uses information from several sub-detectors which are logically OR-ed together. Bunch crossings selected by L1 introduces dead-time. The initial selection here is carried out in 2μs (this is equivalent to 22 bunch crossings, which equals 22 HERA clock cycles).

Information such as pulse heights from the scintillator photo-tubes and wire hit maps can be rapidly accessed from proportional and drift chambers, making them ideal sub-detector candidates for a trigger level system operating under such

restricted time constraints. All tracking detectors use Flash-ADC's, which have a sampling rate of 10 times the HERA bunch crossing frequency.

Since tracks can generally be traced back to their point of origin, this factor can be used to aid the suppression of background events. This priority task for the L1 system means that at least one of the sub-detectors must have good time resolution properties. This then allows the correct bunch crossing to be identified and the event interaction time (t_o) to be determined - this is used to home in on the interaction vertex. Proportional chambers, with their fast response and good time resolution are ideal for this purpose. They are complimented by drift chambers, such as the central z-chamber (CIZ), which provides a z–coordinate for the interaction vertex. Further elimination of background events, such as proton-wall and synchrotron radiation backgrounds, can be done using the central drift chamber, CJC1. Through its ability to find tracks which have a distance of closest approach (DCA) of less than 2 cm from the nominal beam axis, the unavoidable ambiguities in spatial resolution can be minimised and tracks not originating from the interaction vertex can be removed very effectively.

The main veto for the proton induced background is the ToF detector. Its complimentary role in determining the event interaction time (t_o) means that this sub-detector is of central importance to the L1 system.

The calorimetric system is also used - it has an analogue pipeline which switches capacitors to sample and hold the charge signal deposited in the barrel, forward and backward regions. The HERA clock is used to synchronise the trigger signals from the various L1 sub-detectors which are encoded in trigger elements, i.e. yes/no decisions represented in bits. These represent, for example, energy thresholds or coincidences of hits in proportional chamber systems. Different physical characteristics result in individual cable delays. To overcome these, bits are transferred to the Central Trigger Logic (CTL) with the relevant clock pulse, which is then used by the CTL to introduce the appropriate delays to synchronise all groups of elements supplied from the sub-detectors.

If after 2 μs the event satisfies the L1 trigger, the pipeline of the front end is stopped and the necessary systems are made aware that a trigger has occurred. Dead-time starts accumulating from this point.

The level 2 trigger (L2) is similar to the L1 trigger and is hardware based. However, a more sophisticated treatment of the CJC trigger elements, allowing more complex pattern matching, enables the track momentum to to be determined. Specifically the trigger is based on the combined output of special hardware classifying the event topology.

The L2 trigger occurs 20 μs after the relevant bunch crossing. If an L2-reject occurs, this initiates the restart cycle and it takes a few microseconds before the experiment becomes 'alive' again. If an L2-keep occurs, the level 3 (L3) stage begins and dead-time continues to be accumulated.

The L3 trigger is software based. It utilises processes with access to restricted trigger data, based on the calorimeters linked with other detector components. It also uses changes to topological triggers to help filter out unexpected backgrounds. Here, a decision time of up to a few hundred microseconds is required. The restart cycle is initiated by either an L3-reject or after a dead-time of 800 μs, the maximum time required to read out the information from a complete event from all the front end buffers.

The level 4 trigger (L4) (also known as the L4 filter farm) for online filtering and reconstruction, is a software trigger running on 32 RISC (MIPS 3000) processor boards in parallel. The resulting computing power is necessary to analyse the full event in detail whilst allowing filtering in a real-time environment. Any event which has passed the first 3 trigger levels is likely to be complex and require a time-consuming examination to be accepted or rejected. Special rejection algorithms specifically designed for the filter farm are used, along with part of the off-line reconstruction analysis. The rejection strategies used concentrate on getting a much more precise interaction vertex, using the 3-dimensional reconstruction of the vertex, which is available at this stage. This aids the further

suppression of the proton induced backgrounds. There are also algorithms which aid the suppression of backgrounds due to synchrotron radiation.

The events accepted by L4 may be accepted in a different order to the one in which they occurred because of the parallel nature of the filter farm, thus retaining the event number as part of the event information ensures that this is not a problem in future analysis. Primary dead-time is not a problem at this level of filtering, however, there is a major problem in that any event passing L4 will be transmitted to the DESY computer centre for storage and use in physics analysis. To reduce the event rate to the maximum data logging rate, the L4 filter farm must reject, on average, 70%-80% of events.

1.9.2 The H1 Data Acquisition System

As already indicated, the scale of the data acquisition task is enormous. The responsibilities of the H1 system can be divided into three primary charges:

- Collecting information from the various sub-detectors/branches. To allow for the asynchronous readout, the event number is part of the information transferred.
- Merging the information, from the 12 branches currently available into one complete event in the event coordination system, processing these events though the L4 filter farm, monitoring and logging data (with the final full event record being transferred to the central IBM facility at DESY, for storage, off-line processing/reconstruction and analysis).
- System supervision.

One advantage of this system is that it is hardware is based on industrial standards, namely the IEEE VMEbus , and so can make use of commercially available components. The system 'backbone' is a fast multi-mode optical fibre ring, allowing transfer speeds of up to 55 Mbytes/s. The system protocol has been written

'in-house', with the main emphasis placed on speed and efficiency. As it has been developed within the framework of international protocols, the system can be monitored directly from the home institutes of the international collaboration.

The complete VMEbus system is interfaced to a system supervisor Macintosh, from which it can be controlled and monitored.

1.10 The H1 Software Chain

Once an event has successfully passed the L4 trigger, it is fully reconstructed by the H1 reconstruction software H1REC [16], and put onto 'production output' tapes (POTs). The POT data contains a large fraction of background events which passed the online triggers and so further event reduction is done using software algorithms which look for event characteristics associated with types of physics processes. Events which pass these off-line selections are assigned a (physics) class number and are put onto data summary tapes (DST). This level of data selection is sometimes referred to as 'level 5' (L5).

The physics analysis package H1PHAN [17] uses the reconstructed data from simulated or real data (POT's or DST's) and converts them into meaningful physical measurements which are expressed as four-vectors. It provides the routines to allow determination of event kinematics, simple particle identification and jet reconstruction. The user must provide physics analysis code for their study which can then be used within the framework of H1PHAN. H1PHAN can also be used to analyse generated data.

The H1 simulation program H1SIM [18] is based on the GEANT [19] package. H1SIM provides an accurate detector simulation which can then be used to fine tune physics analysis programs, study trigger efficiencies and energy flow properties in the different calorimeters. It simulates all the physics associated with the passage of particles through the various sub-detectors. H1SIM produces response banks which have the form of those produced by the real detector, the output of

which can then be reconstructed using the H1REC software chain. The process can be summarised as generated Monte Carlo (m/c) $\rightarrow$ H1SIM $\rightarrow$ simulated m/c $\rightarrow$ H1REC $\rightarrow$ reconstructed m/c.

During data taking, parts of the detector may contain dead regions. Therefore, in order to compare the real data with reconstructed Monte Carlo, the dead regions are accounted for during the reconstruction of the H1SIM data. This allows the performance of the detector to be better understood

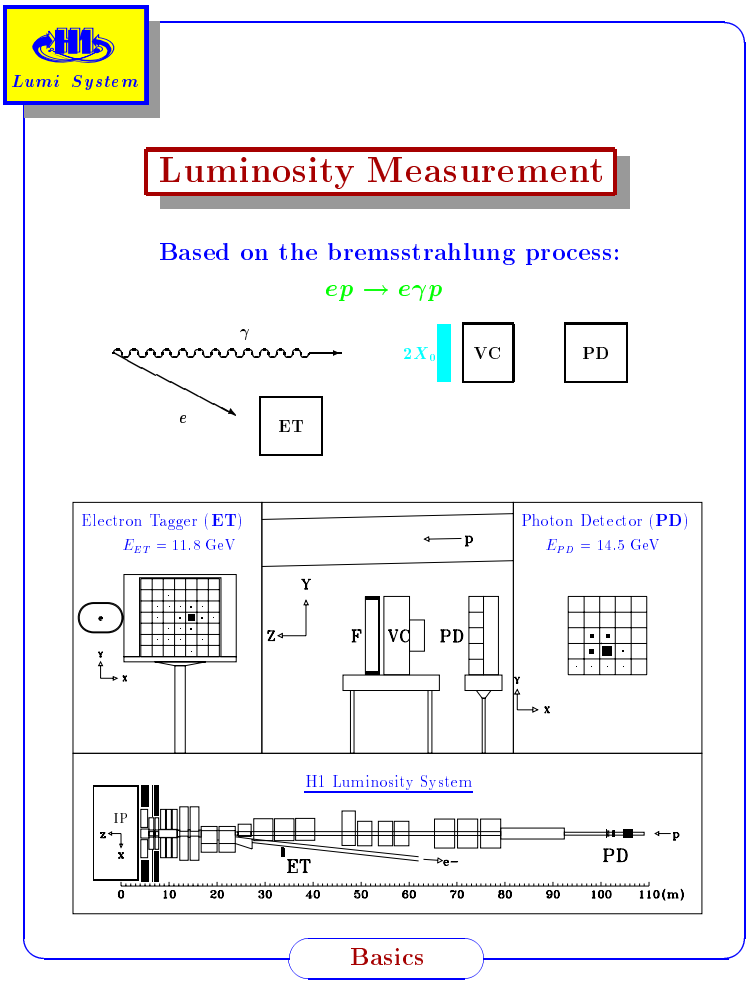

Figure 1.6: *The Luminosity System.*

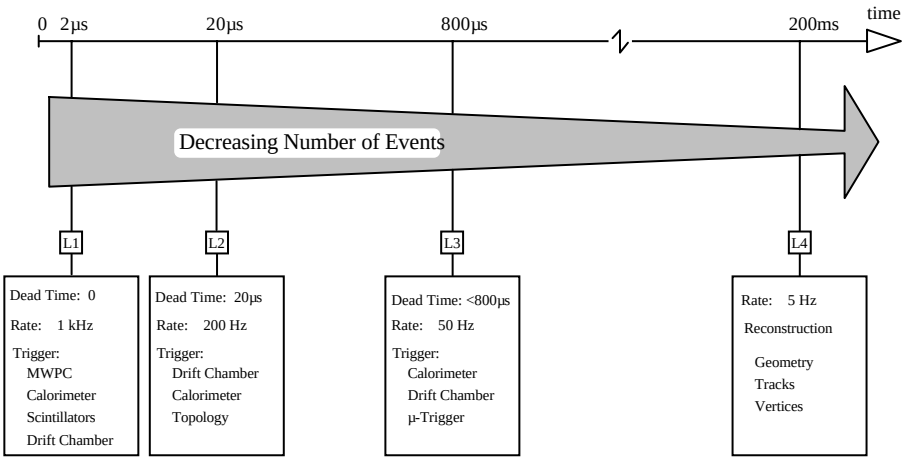

Figure 1.7: *The H1 trigger/filtering stages.*

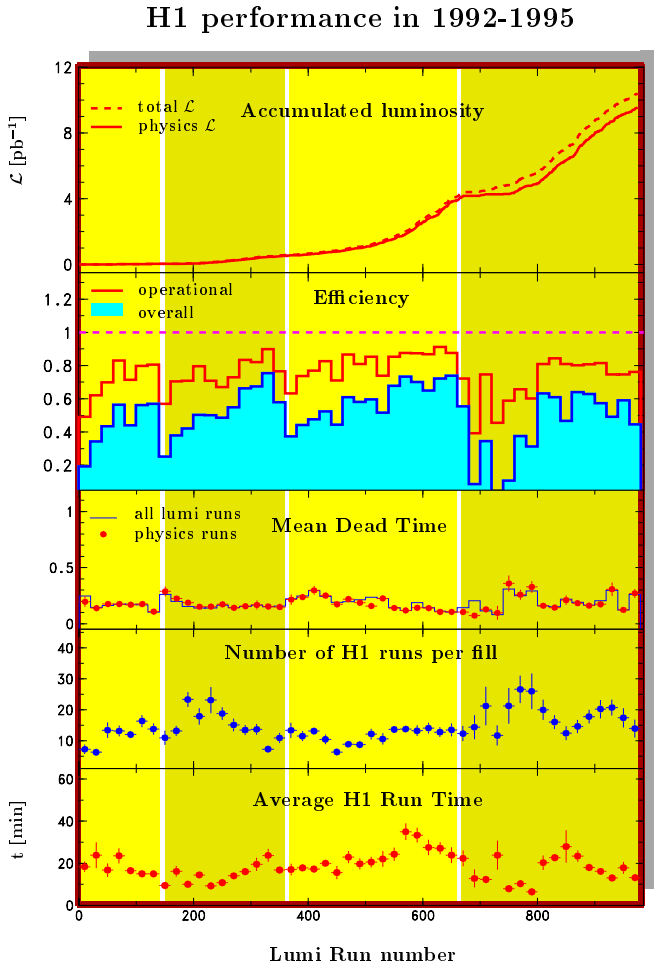

Figure 1.8: *Performance of the H1 detector for the years 1992 - 1995.*

Chapter 2

Physics at HERA

2.1 Introduction

This chapter will define the kinematics relevant to this thesis and give a brief overview of the dominant physics processes at HERA.

2.2 Kinematics

To first order, the lepton-proton deep inelastic scattering (DIS) diagram for the process $ep \to e' + X$ is shown in Figure 2.1 and defines the four-vectors involved in the kinematics. The kinematics of this process at a fixed centre of mass energy, $\sqrt{s}$, is determined by two independent variables chosen from Q^2 and the scaling quantities x and y. Q^2 is the negative four-momentum transfer squared between the incident and scattered lepton. In the rest frame of the incident proton, x in the naive quark parton model (QPM) is the fraction of the incident proton momentum carried by the struck parton (Bjorken x), and y is the fraction of energy transferred from the incident lepton to the hadronic system in the proton rest frame.

As the H1 experiment measures both the scattered lepton and the hadronic final

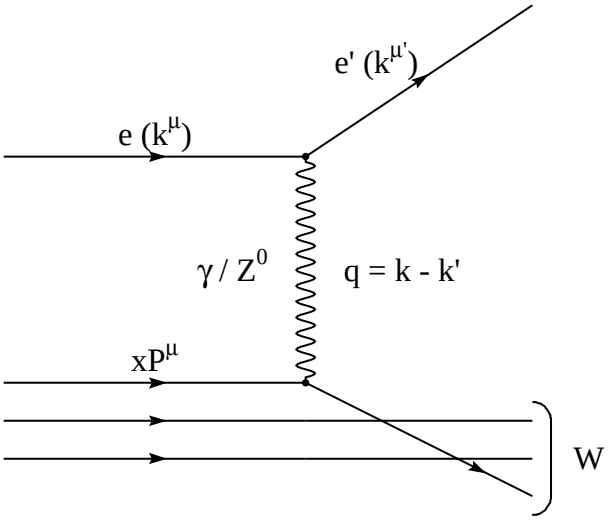

Figure 2.1: *Born term diagram for deep inelastic scattering.*

state produced between the struck parton and the proton remnant, the collision kinematics are over constrained and can be determined from lepton variables, hadronic variables or a mixture of both.

The kinematic variables are defined as follows:

$$Q^2 = -q^2 = -(k - k')^2 \tag{2.1}$$

$$y = \frac{P \cdot q}{P \cdot k} \tag{2.2}$$

$$x = \frac{Q^2}{2P \cdot q} \tag{2.3}$$

where

- k^μ is the four-momentum of the incident lepton,
- $k^{\mu\prime}$ is the four-momentum of the scattered lepton,
- P^μ is the four-momentum of the incident proton and,

- q^μ is the four-momentum transfer of the exchange boson.

Neglecting the proton mass, the invariant mass of the hadronic final state, W, is given by:

$$W^2 = (P+q)^2 \approx Q^2 \left(\frac{1-x}{x}\right) \tag{2.4}$$

The centre of mass energy squared (s), neglecting the mass of the proton and electron is given by:

$$s = (k+P)^2 \approx 4E_e E_p \tag{2.5}$$

where E_e and E_p are respectively the energies of the incident lepton and proton. With the current HERA beam energies, s reaches 87600 GeV^2. Due to this high centre of mass energy and using the relation:

$$Q^2 = sxy \tag{2.6}$$

HERA can reach down to $x \sim 10^{-4}$ in the deep inelastic regime ($Q^2 > 10$ GeV^2). For small Bjorken x, y approximates to $\sim W^2/s$.

The kinematic variables in this thesis are determined from the polar angle (θ) and energy (E'_e) of the scattered lepton through the relations:

$$Q^2 = 2E_e E'_e(1+\cos\theta) \tag{2.7}$$

$$y = 1 - \frac{E'_e}{2E_e}(1-\cos\theta) \tag{2.8}$$

Polar angles such as θ are measured with respect to the proton beam (forward) direction. The kinematics for the scattered lepton in the (x, Q^2) plane is shown in figure 2.2. For a large region of the plane, corresponding to $\sim y < 0.1$, the energy of the scattered lepton is close to the incident lepton beam energy. This leads to a peak in the scattered lepton energy spectrum (termed the 'kinematic peak') which serves beneficially for calibration purposes.

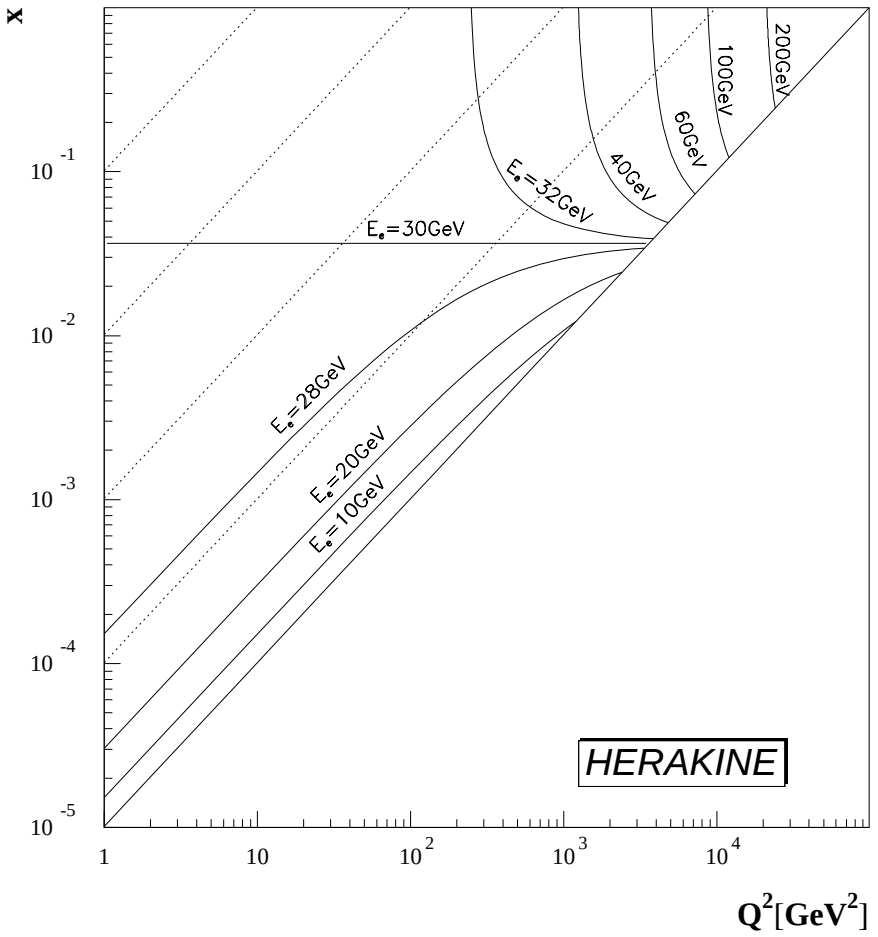

Figure 2.2: *Lines of constant energy for the scattered lepton in the (x, Q^2) plane for DIS events. The dotted lines running at 45° are lines of constant y, with the solid 45° line indicating the edge of the kinematic region where $y = 1$.*

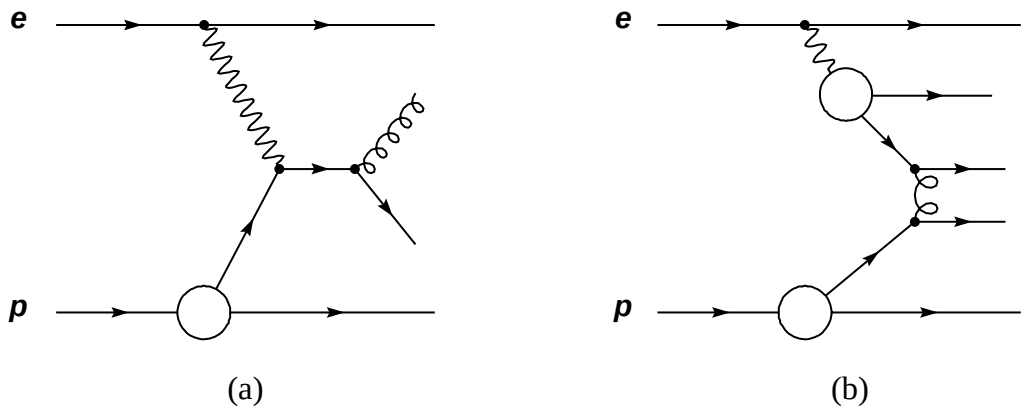

Figure 2.3: *Examples of diagrams for (a) direct and (b) resolved photon processes in lepton–proton scattering.*

2.3 Photo-production

In lepton-proton collisions at HERA, the cross section is dominated by photo-production [20] processes where the lepton radiates a quasi-real photon which then interacts with the proton. Due to the large cross section, photo-production constitutes a large background for DIS studies. In the framework of QCD, the photon couples either directly to a parton in the proton, or indirectly via the photon's own parton content. The first are called *direct* processes, which include QCD-Compton and photon-gluon fusion (Figure 2.3a), while the latter are usually referred to as *resolved* processes (Figure 2.3b) characterised by the photon structure functions.

2.4 Deep Inelastic Scattering (DIS)

A prime task of HERA is the investigation of the structure of the proton [21]. Measurements of the inclusive lepton-proton scattering cross section have been crucial for the understanding of proton substructure. Early electron-proton scattering experiments have discovered point-like proton constituents by observing a

scale invariant dependence of the structure function $F_2(x, Q^2)$ on Q^2 at Bjorken $x \geq 0.1$ and Q^2 values of about 5 GeV^2. Subsequent neutrino scattering experiments have established the Quark Parton Model (QPM) as a valid picture of the valence and sea quarks as constituents of the proton. The interaction of these partons as mediated by gluons is successfully described by by Quantum Chromodynamics (QCD) which has been tested with high precision in muon-nucleon DIS experiments. Experiments at HERA extend the previously accessible kinematic range up to very large Q^2 ($Q^2 > 10^3$ GeV^2), and down to very small values of Bjorken x ($x < 10^{-4}$). At low x ($x < 10^{-2}$), the measurement of the structure function $F_2(x, Q^2)$ shows a strong rise with decreasing x [22, 23]. It is not clear if the rise is fully described by the QCD evolution equations, such as the conventional DGLAP evolution [24] in logQ^2 or by the BFKL evolution [25] in $\log(1/x)$.

For momentum transfers small compared with the mass of the Z^0, the cross section for deep inelastic lepton-proton scattering in lowest order (Born cross section) can be expressed in terms of a single structure function F_2 and the ratio of the cross sections for longitudinally and transversely polarised photons on protons, $R = \sigma_L/\sigma_T$:

$$\frac{d^2\sigma}{dxdQ^2} = \frac{2\pi\alpha^2}{xQ^4}\left(2(1-y) + \frac{y^2}{1+R}\right) F_2^P(x, Q^2) \tag{2.9}$$

The ratio R [8] has not yet been measured at HERA and is expected to be sizable at large y.

2.5 Transverse Energy Flow - E_T

A more sensitive method of determining whether low x physics is described by the BFKL or DGLAP evolution equations may be in the measurement of transverse energy (E_T) flows. At low Bjorken x, the dominant parton dynamics are based on a virtual photon-gluon fusion to a quark and an anti-quark which is shown in Figure 2.5 with additional contributions from a 'ladder' of parton exchange.

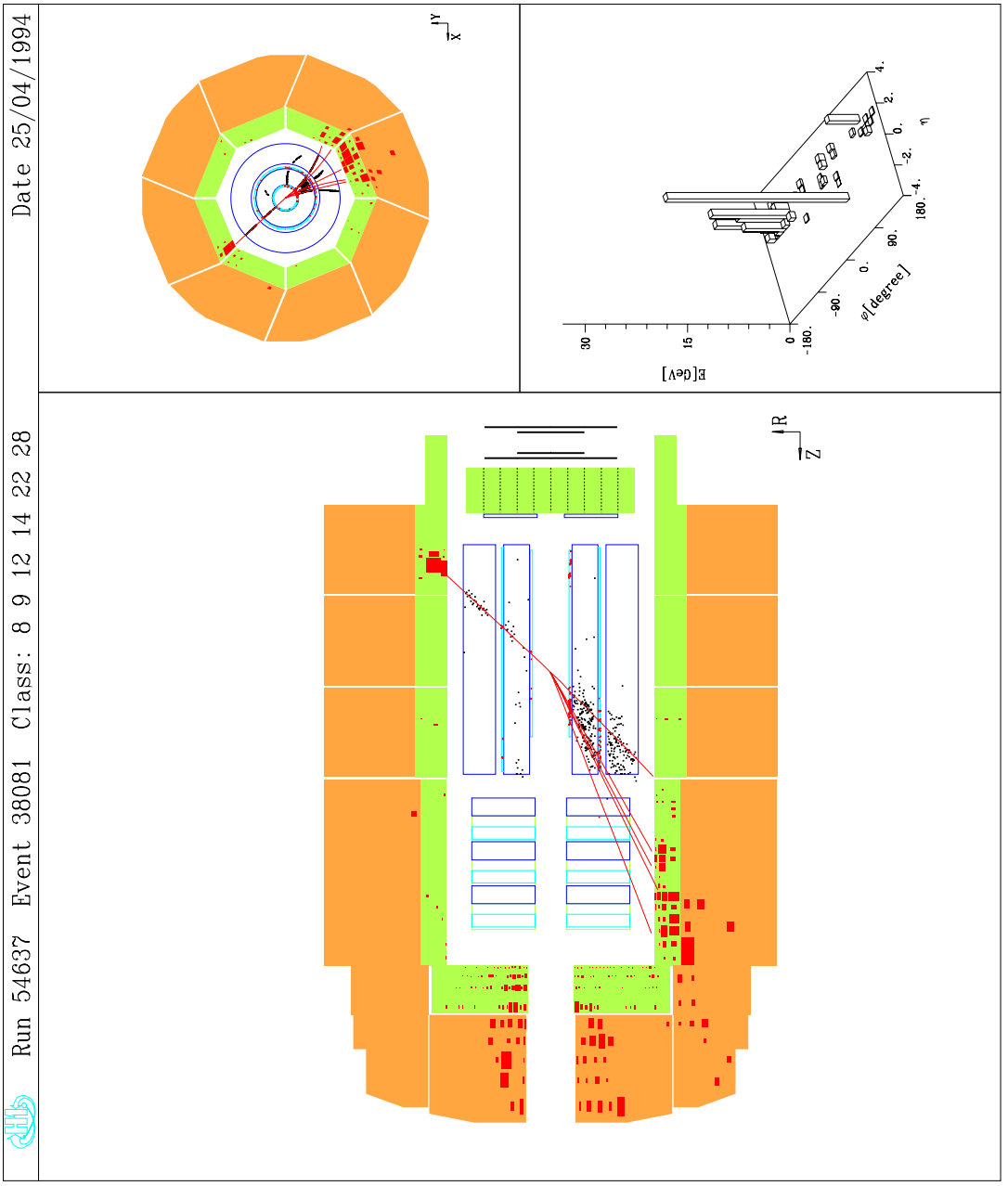

Figure 2.4: *A neutral current Deep Inelastic Scattering event in the H1 detector.*

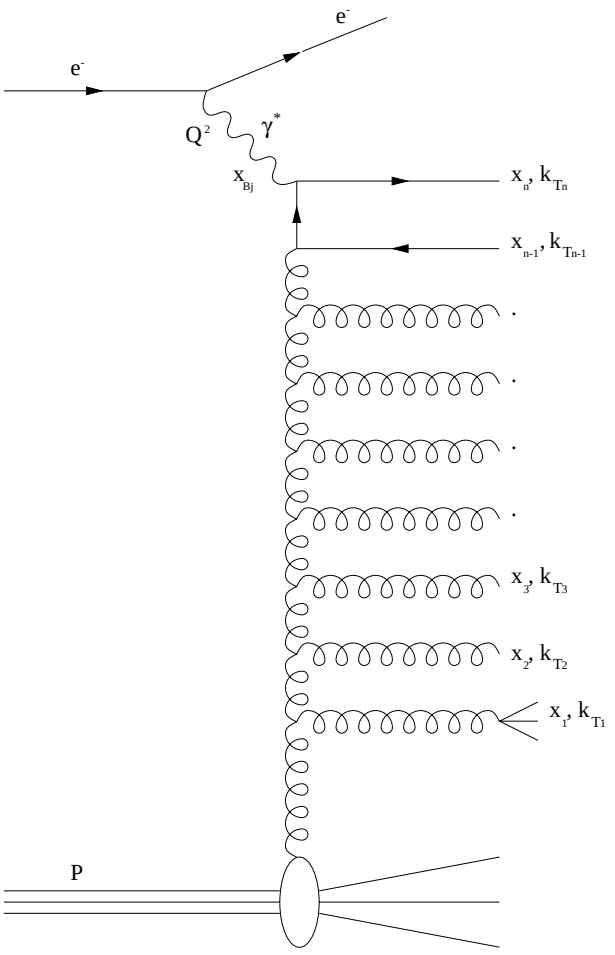

Figure 2.5: *Schematic Feynman diagram for ep DIS at low Bjorken x illustrating how QCD can give rise to hadron production from partons produced between the 'struck' or 'current' quark at $x = x_n = x_{Bj}$ and the proton remnant.*

In the DGLAP scheme, the parton cascade is evolved in Q^2 leading to a strong ordering in transverse momenta $k^2_{T_n} >> k^2_{T_{n-1}} >> \ldots >> k^2_{T_1}$, while there is only a soft ordering for the longitudinal parton momentum scaled by the proton momentum, $x_n < x_{n-1} < \ldots < x_1$. In the BFKL scheme, the cascade follows a strong ordering in fractional momentum $x_n << x_{n-1} << \ldots << x_1$, while there is no ordering in transverse momentum, k_T. As a consequence, the BFKL approximation to QCD expects more E_T between the remnant and the struck quark than other schemes.

2.6 Large Rapidity Gap Events

Observations by the HERA experiments H1 and ZEUS have shown the presence of events with a large 'rapidity gap' in DIS. Figure 2.6 [26] shows the distribution of the gap in pseudo-rapidity, $\eta = -\ln(tan(\theta/2))$, measured with respect to the forward edge of the LAr calorimeter (a polar angle of $\theta = 5°$, $45°$, $90°$, $135°$ and $175°$, corresponds to an η of 3.1, 0.88, 0, -0.88 and -3.1 respectively) to the first significant energy deposition, for all DIS events.

A typical DIS event exhibits energy flow associated with the direction of the proton remnant which, in terms of the colour string picture, results from the fragmentation of the colour string between the struck quark and the proton remnant. Thus large rapidity gap events are interpreted as an interaction between the probing virtual photon with a colourless piece of the proton which carries very little of its parent's momentum (leaving the proton relatively unscathed) as shown in Figure 2.7. Events with such a rapidity gap amount to $\sim 7\%$ to 8% of the DIS sample.

For many years this colourless exchange was considered phenomenologically to be the exchange of the pomeron. However, recent results [27] demonstrate that an understanding of the energy/momentum transfer of the pomeron is possible in terms of the exchange of gluons, and that there is a suggestion that one gluon carries most of the momentum transfer.

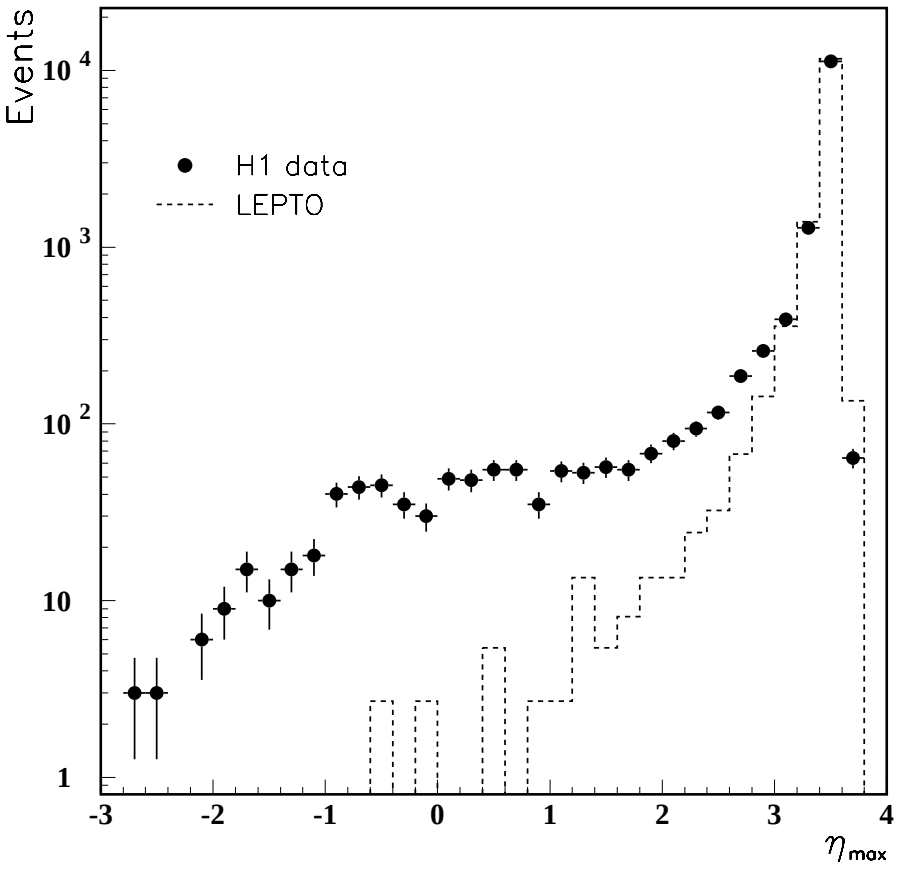

Figure 2.6: *Distribution of the measured η_{max} for all DIS events together with the expectation from the LEPTO Monte Carlo which reveals a clear excess of events in the plateau below $\eta_{max} \approx 2$.*

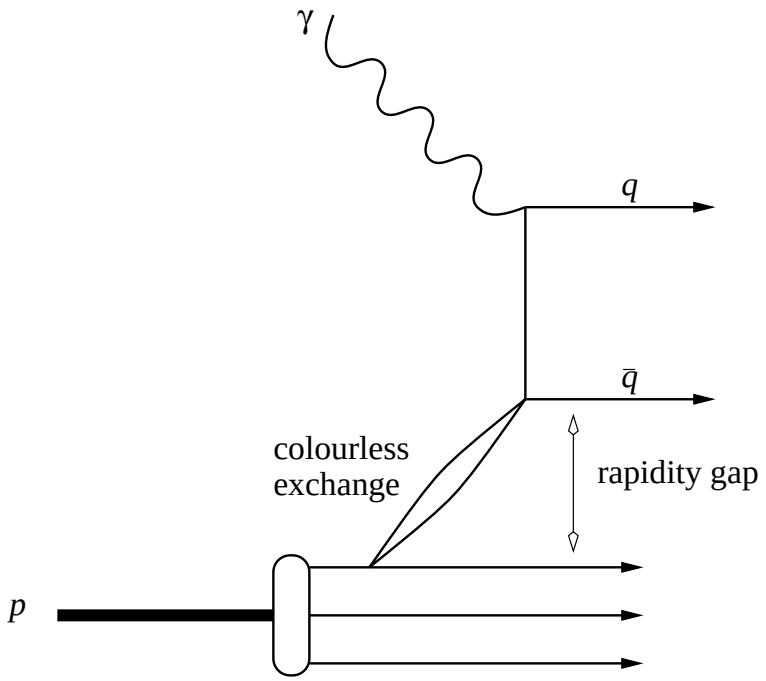

Figure 2.7: *Diagram for a deep inelastic event where the virtual photon scatters off a colourless object within the proton.*

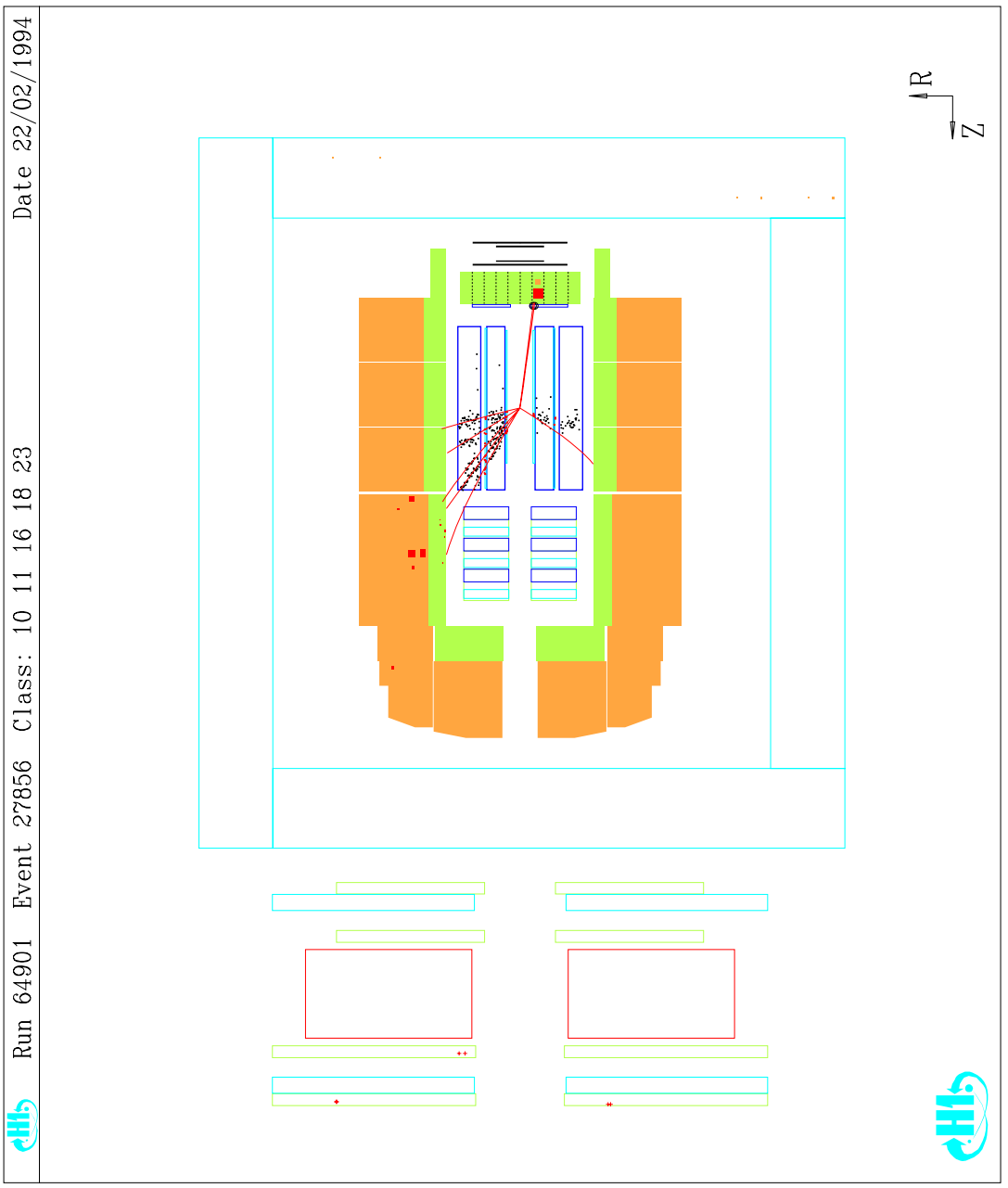

Figure 2.8: *A Rapidity Gap event in the H1 detector.*

Chapter 3

QCD Models

3.1 Quantum Chromodynamics

Quantum Chromodynamics (QCD) is the current theory of the strong interaction between quarks.

Flavour	Electric Charge
u	+2/3
d	-1/3
c	+2/3
s	-1/3
t	+2/3
b	-1/3

Table 3.1: *The physical properties of quarks.*

In the standard model the quarks are the only matter fields which couple to the mediators (gluons) of the strong force. It is the effect of this force which produces the clusters of quarks that are detected by experiment - a free particle with a fractional charge has never been experimentally observed, implying that free quarks are not found in nature. The residual effects of this force hold the constituents of nuclei together, and this was the first phenomenological effect of

the strong force to be experimentally observed. The true nature of the strong force was discovered when deep inelastic scattering experiments implied that nucleons had substructure, and thus the quark was discovered [2].

Following this discovery, it was shown that there exists a class of gauge invariant quantum field theories that are both renormalisable and which produce a mechanism to explain quark confinement [1], i.e. a force that is small in magnitude for distances less than 10^{-15}m but whose strength increases dramatically as this limit is exceeded. This is known as asymptotic freedom. The member of this class of field theories with properties that match experimental observations has the properties of the gauge group $SU(3)$.

The charge of the strong gauge group $SU(3)$ is colour, and can take one of three values - red, green or blue. Thus one of these three charges is assigned to each quark, whilst the anti-quarks are either anti-red, anti-green or anti-blue. Therefore, for calculations involving effects of the strong force the quarks are placed in triplet representations of $SU(3)_C$. Due to the non-abelian nature of the gauge group, the gauge bosons are coloured (giving rise to an octet of gluon fields) and therefore self-couple. It is this facet of the theory which gives rise to asymptotic freedom.

The vacuum polarisation contribution to quark-quark scattering causes the coupling constant of the theory, α_s, to decrease as the energy scale, Q^2, increases. To leading order, the coupling constant can be written as:

$$\alpha_s(Q^2) = \frac{12\pi}{(33 - 2N_f)\,\ln(Q^2/\Lambda^2)} \tag{3.1}$$

where N_f is the number of quark flavours and Λ is a free parameter that must be determined experimentally. Λ governs the dependence of α_s on energy and characterises the scale at which α_s becomes sufficiently large that perturbative QCD breaks down. This constant represents the boundary between the world of quarks and gluons and the physical world of hadrons.

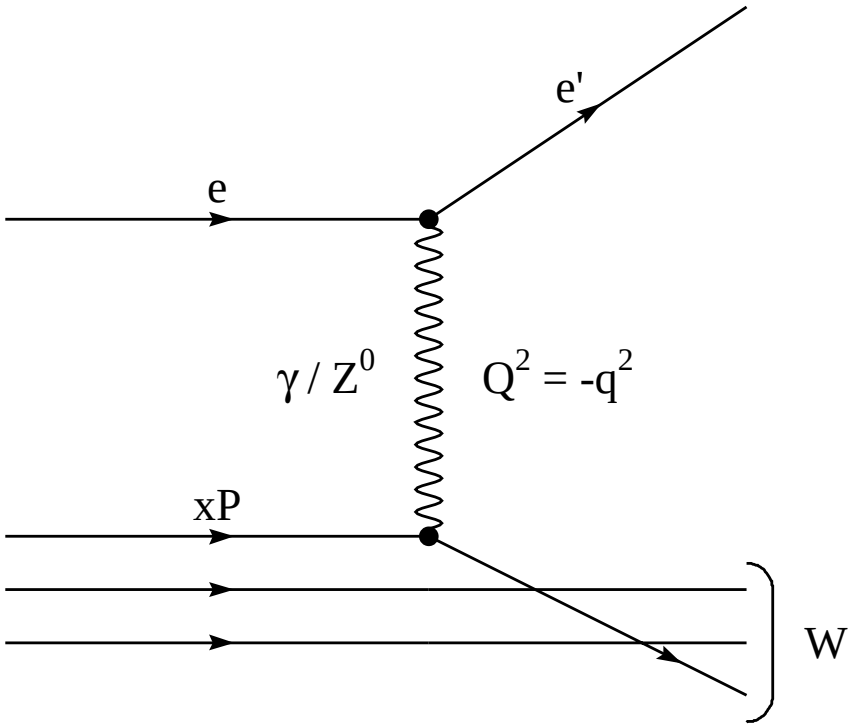

Figure 3.1: *DIS in the Quark Parton Model.*

3.2 The Quark Parton Model

The Quark Parton Model may be considered as being 0^{th} order QCD. Since QCD radiation is neglected, the proton is viewed as consisting of three 'valence' quarks accompanied by many quark-antiquark pairs (mainly $u\overline{u}$, $d\overline{d}$ and $s\overline{s}$), known as sea quarks, which share the proton's momentum while having little intrinsic transverse momentum. The DIS process described by this model involves scattering off a single valence or sea quark which is carrying a fraction, x, of the proton's momentum, Figure 3.1

The structure of the proton can be probed when the wavelength of the photon is sufficiently less than the proton diameter (10^{-15} m), which implies a probe

momentum above 1 GeV ($p = hc/\lambda$). In early DIS experiments, the proton structure function, $F_2(x, Q^2)$ was observed to be roughly independent of Q^2 at a given x (as the structure functions were examined for variations over only a limited range of Q^2, predominantly in the mid x regions where there is no variation). This scaling behaviour, known as *Bjorken* scaling, was interpreted as evidence for the existence of point like partons.

In the absence of weak interactions, the un-polarised differential cross section for the DIS process can be written in terms of two dimensionless structure functions, $F_1(x, Q^2)$ and $F_2(x, Q^2)$:

$$\frac{d^2\sigma}{dxdQ^2} = \frac{4\pi\alpha^2}{xQ^4}[(1-y)F_2(x,Q^2) + xy^2F_1(x,Q^2)] \tag{3.2}$$

Callan and Gross showed that in the quark parton model, the structure functions should be related [1]:

$$F_2(x) = 2xF_1(x) \tag{3.3}$$

which is a consequence of the quarks having spin $\frac{1}{2}$ and is well borne out by the data.

The structure functions essentially measure how the proton momentum is distributed amongst partons of various charges. If we say that the ith type of parton with charge e_i has the probability $f_i(x)$ of carrying a fraction x of the nucleon momentum, then it is possible to relate the overall structure functions of the proton to the following parton momentum distributions:

$$F_2(x) = x\sum_i e_i^2 f_i(x) \tag{3.4}$$

3.3 Matrix Elements

First order QCD matrix elements are necessary to describe more complex scattering. The basic processes are QCD Compton (QCDC), in which a gluon is radiated

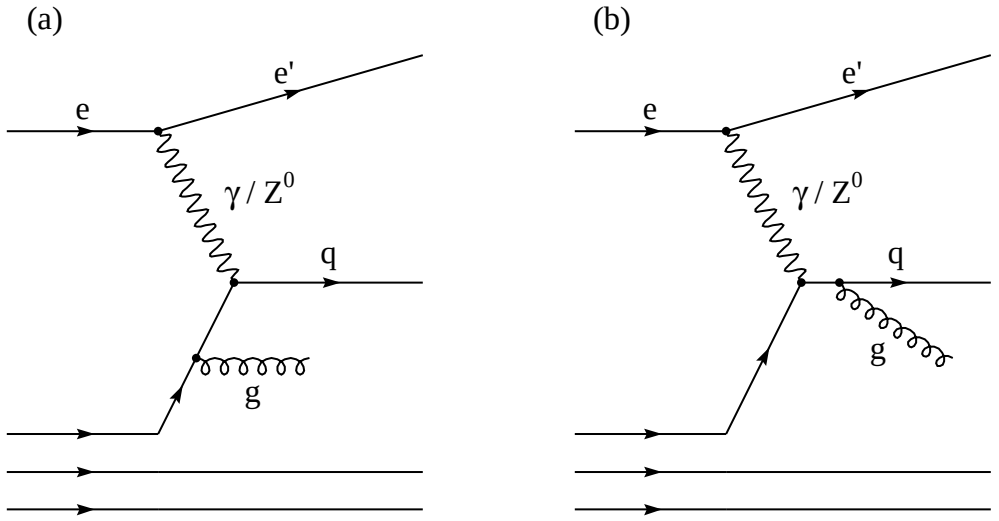

Figure 3.2: *First order Feynman diagram for QCD compton scattering.*

off a quark either before or after the quark interacts with the photon, Figure 3.2, and Boson Gluon Fusion (BGF) where one of the proton's quarks radiates a gluon, Figure 3.3. This virtual gluon goes on to decay into a quark-antiquark pair and it is this pair that takes part in the interaction with the photon. The matrix elements for the diagrams shown in Figure 3.2 and Figure 3.3 have been calculated exactly.

3.4 Leading Logarithmic ($\ln Q^2$) Parton Showers

In addition to the basic DIS process of γq scattering there are higher order QCD processes which describe the emission of further partons before and after the boson vertex. In principle, some of the higher order matrix elements are calculable, although in practice this can be extremely difficult. Instead, a scheme of initial

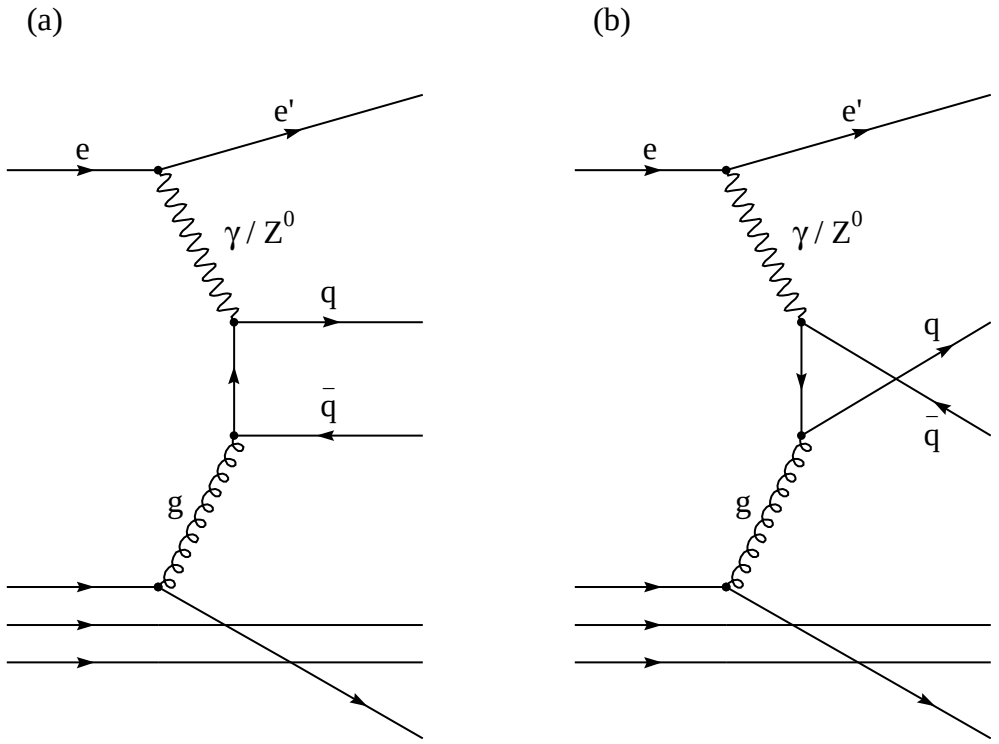

Figure 3.3: *First order Feynman diagram for Boson Gluon fusion.*

and final state parton showers can be used.

This scheme allows the splitting of a parent parton into two daughters with the possibilities $q \to qg$, $g \to q\overline{q}$ and $g \to gg$. For each possibility, the probability $\mathcal{P}_{a\to bc}(z)$ of splitting is defined as a function of z, the energy fraction taken by daughter b. Final state showering commences with partons emerging from the hard subprocess and uses the parton mass as a virtuality scale by which emissions are ordered. Monte-Carlo techniques are used to select the mass and energy fraction of an emerging parton. The daughters then become prospective parents until a cut–off virtuality is reached. In the case of initial state radiation, the process runs in reverse where the highly virtual hard scattering partons are known and the parent parton energies must be derived. Because the squared masses involved in initial state showers are negative whilst those of final state showers are positive, they are often referred to as space-like and time-like showers.

In the leading logarithmic approximation (LLA), the probability for a branching

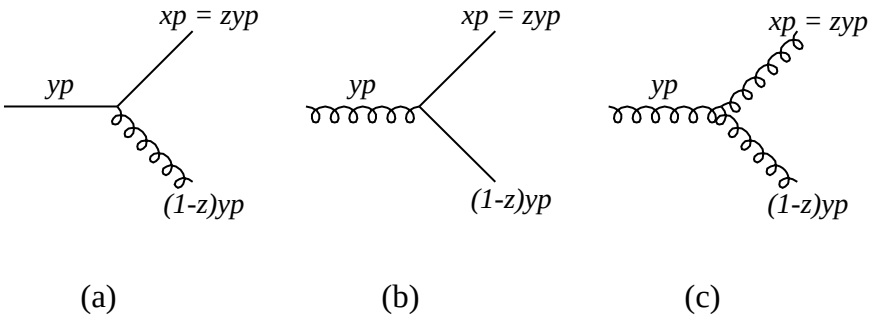

Figure 3.4: *Basic parton processes described by the splitting probability functions (a)* $\mathcal{P}_{qq}(z)$*, (b)* $\mathcal{P}_{gq}(z)$*, (c)* $\mathcal{P}_{gg}(z)$*.*

$a \to bc$ to take place during a small change $dt = dQ^2_{evol}/Q^2_{evol}$ of the evolution parameter $t = \ln(Q^2_{evol}/\Lambda^2)$ is given by the DGLAP equations [24]:

$$\frac{d\mathcal{P}_{a\to bc}}{dt} = \int dz \frac{\alpha_s(Q^2)}{2\pi} \mathcal{P}_{a\to bc}(z) \tag{3.5}$$

where $\mathcal{P}_{a\to bc}(z)$ are the splitting kernels and describe the probability that a parton of four-momentum zp will be found in what started as a parton of initial momentum p before the branching. The splitting functions are:

$$\mathcal{P}_{qq}(z) = \frac{4}{3}\left[\frac{1+z^2}{1-z}\right] \tag{3.6}$$

$$\mathcal{P}_{qg}(z) = \frac{1}{2}\left[z^2 + (1-z)^2\right] \tag{3.7}$$

$$\mathcal{P}_{gq}(z) = \frac{4}{3}\left[\frac{1+(1-z)^2}{z}\right] \tag{3.8}$$

$$\mathcal{P}_{gg}(z) = 6\left[\frac{(1-z)}{z} + z(1-z) + \frac{z}{(1-z)}\right] \tag{3.9}$$

the diagrams for which are shown in Figure 3.4.

3.5 Expectations from the Modified Leading Logarithmic Approximation

The inability of long wavelength gluons to resolve individual colour charges of partons within the parton cascade reduces the available phase space for soft gluon emission to an angular ordered region due to interference effects. This is known as colour coherence. This is modelled in the Modified Leading Log Approximation (MLLA) and gives rise to a characteristic 'hump-backed' plateau in the parton momentum spectrum. The model has been developed to describe the properties of soft particles produced with relatively small momenta in e^+e^- interactions [47]. The MLLA predicts the form of the inclusive momentum distribution for massless partons radiated from a high energy source, $E^* = \sqrt{s_{ee}}$. The analytical form is given by a limiting spectrum, $\overline{D}^{lim}(\xi, Y)$ [47]. The variables are $\xi = \ln(1/x_p)$ where the scaled momentum $x_p = 2p_{hadron}/E^*$ and the dimensionless variable $Y = \ln(E^*/2\Lambda_{eff})$. The free parameter Λ_{eff} sets the scale of the mass of the final state fragmented hadrons and is not directly related to $\Lambda_{\overline{MS}}$.

The MLLA predictions are used in conjunction with Local Parton-Hadron Duality (LPHD) which is described later in this chapter.

The limiting spectrum is a hump–backed plateau and the MLLA results can be directly applied to the observed distributions such that:

$$\frac{1}{\sigma}\frac{d\sigma}{d\xi} = \kappa^{ch}\overline{D}^{lim} \tag{3.10}$$

where the parameter κ^{ch} is the constant of proportionality used to relate the hadron spectrum to the analytical spectrum from the MLLA.

The MLLA result can be approximated by a Gaussian distribution about the peak position given by:

$$\frac{1}{\sigma}\frac{d\sigma^{e^+e^-}}{d\xi} \approx N(Y)\left(\frac{c_1}{\pi Y^{3/2}}\right)^{1/2} exp\left(\frac{-c_1[\xi-\xi_{max}]^2}{Y^{3/2}}\right) \tag{3.11}$$

where $c_1 = \sqrt{36N_c/b}$ and $b = 11N_c/3 - 2N_f/3$ are constants which depend on the

number of flavours, N_f and number of colours, N_c. $N(Y)$ is the average charge particle multiplicity which, within the assumption of LPHD, is proportional to the soft parton multiplicity predicted by the theory.

If Q is taken to be equivalent to $\sqrt{s_{ee}}$ and is normalised by an effective energy scale to give a variable $Y = \ln(Q/2\Lambda_{eff})$ then, assuming gluon coherence, the predicted MLLA behaviour of the peak position and width is [47]:

$$\xi_{peak} = 0.5Y + c_2\sqrt{Y} + \mathcal{K} \tag{3.12}$$

$$\xi_{width} = \sqrt{Y^{3/2}/2c_1} \tag{3.13}$$

where $c_2 = B\sqrt{b/16N_c}$, $B = (\frac{11}{3}N_c + \frac{2}{3}N_f/N_c^2)/b$ and $\mathcal{K}$ contains higher order corrections.

In equation 3.12, it can be seen that apart from the higher order correction, Λ_{eff} is the only free parameter and even that is constrained to be a few hundred MeV. Once a value has been determined, the peak position and width can be predicted at any value of Q and is the subject of this thesis.

3.6 The Colour Dipole Model

The Colour Dipole Model (CDM) [33] as implemented in Ariadne [36] has had considerable success in describing data from both e^+e^- [34] and lepto-production [9] experiments.

The CDM treats most QCD coherence effects by describing the gluon bremsstrahlung in terms of radiation from colour dipoles between partons, instead of treating partons as independent emitters.

Ariadne is one of the Lund family of Monte Carlo programs and only generates the QCD cascade process. For full event generation, Ariadne has to be interfaced to other programs - LEPTO [9] which generates the electro-weak part of the scat-

tering process and JETSET [37] which performs the hadronisation and particle decays.

The CDM is based on the fact that a gluon emitted from a $q\overline{q}$ pair can be treated as radiation from the colour dipole between the q and the $q\overline{q}$, and that to a good approximation, the emission of a second softer gluon can be treated as radiation from two independent dipoles, one between the q and g and one between the g and $\overline{q}$. In the CDM, this is generalised so that the emission of a third, still softer gluon, is given by three independent dipoles etc. For gluon emission there are three different kinds of colour dipoles to be considered – $q\overline{q}$, qg (or $\overline{q}g$) and gg dipoles. The cross section for each of these can be calculated from the relevant Feynman diagrams in Figure 3.5.

3.6.1 Radiation from extended sources

In Deep Inelastic Scattering (DIS) of leptons on hadrons, the CDM does not divide the QCD cascade into an initial and final state as conventional parton cascades do. Instead, it assumes that all radiation can be described as radiation from the colour dipole formed between the struck quark and the hadron remnant. In this way, the situation is very similar to the e^+e^- case with one important modification. In e^+e^- both the q and $\overline{q}$ can be considered point-like, but for DIS only the struck quark is point–like[1] while the hadron remnant is an extended object. As emissions of small wavelengths from an extended antenna is suppressed and that for an antenna of transverse size l, effectively only a fraction proportional to the emitted wavelength $\lambda \propto 1/k_T$ is participating in the emission. In the CDM, this is taken into account and means that the available phase space is reduced compared with the e^+e^- case leading to a suppression of the radiation in the target region.

[1] At low–x, even this is no longer true.

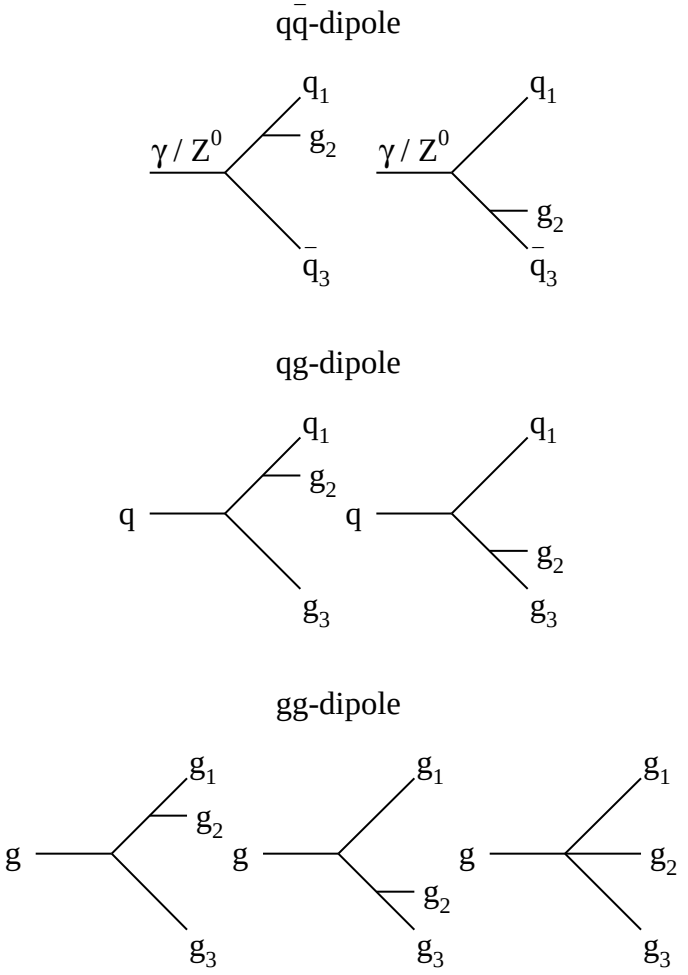

Figure 3.5: *The relevant Feynman diagrams for gluon emission from a $q\overline{q}$, qg and a gg dipole.*

3.6.2 CDM and Boson-Gluon Fusion

In the CDM, the Boson-Gluon fusion (BGF) process is not described at all. Therefore a matching procedure has been introduced for the first emission in a DIS event [35]. In this procedure, the initial dipole between the struck quark and the hadron remnant can either emit a gluon according to the $\mathcal{O}(\alpha_s)$ matrix element or "emit" the anti-partner of the struck quark according to the BGF matrix element. The selection process is made by the Sudakov [38] form-factor prescription. In the case of BGF, there are then two dipoles connecting each of the struck quarks with the hadron remnant, which continue to radiate independently.

3.7 Fragmentation

The closest one can get to observing the dynamics of individual partons is through the study of hadrons. Fragmentation is thought to be a two stage process - (a) the perturbative phase of gluon emission and (b) the low momentum, non-perturbative, or hadronisation stage. Due to the breakdown of perturbative techniques in the limit $Q \sim \Lambda_{\overline{MS}} \sim 100 - 400$ MeV (equation 3.1), the fragmentation of quarks and gluons occur at too low an energy to be treated perturbatively. This insufficient understanding of the confinement mechanism in QCD means that phenomenological models, of which there are several, must be used instead.

3.7.1 Local Parton-Hadron Duality

Local Parton-Hadron Duality (LPHD) assumes that the general features of the final state (e.g. energy flows), are the same at the parton and hadron level. This has the advantage that results of analytical calculations, obtained in suitable approximation schemes, can be directly compared to measured hadron distributions without invoking any hadronisation model.

3.7.2 Independent Fragmentation

The Independent Fragmentation Model was first proposed by Feynman and Field in 1978 [28]. It will not be described here other than to say that the two ends of the colour string fragment without reference to each other (i.e. independently). It is little used due the basic deficiency that it cannot conserve both energy and longitudinal momentum simultaneously.

3.7.3 String Fragmentation

Lattice QCD studies [29] tend to support the confinement picture, where the energy stored in a dipole field between the quark and the anti-quark increases linearly with the separation between them. So, in the simplest case, with no gluon emission, the struck quark attempts to leave the proton and in doing so causes the chromodynamic flux between it and the proton remnant to spread out in a narrow tube, the string. At a point where the potential energy of the colour field is sufficient, a quark-antiquark pair can tunnel out of the vacuum, i.e. the string breaks into two less energetic strings, which continue to separate, Figure 3.6. If the invariant mass of either of these two strings is large enough, further breaking occurs. In the Lund String Model [30] this process of string breaking is assumed to proceed until only "on mass-shell" hadrons remain.

3.7.4 Cluster Fragmentation

The formation and decay of colourless clusters is implemented by HERWIG [32]. After the perturbative stage of parton generation, all final gluons are split non-perturbatively into essentially light (u or d) quark and anti-quark pairs. It then combines nearby coloured objects into colourless clusters which subsequently decay into hadrons according to the available phase space and the branching ratios of the particle data tables.

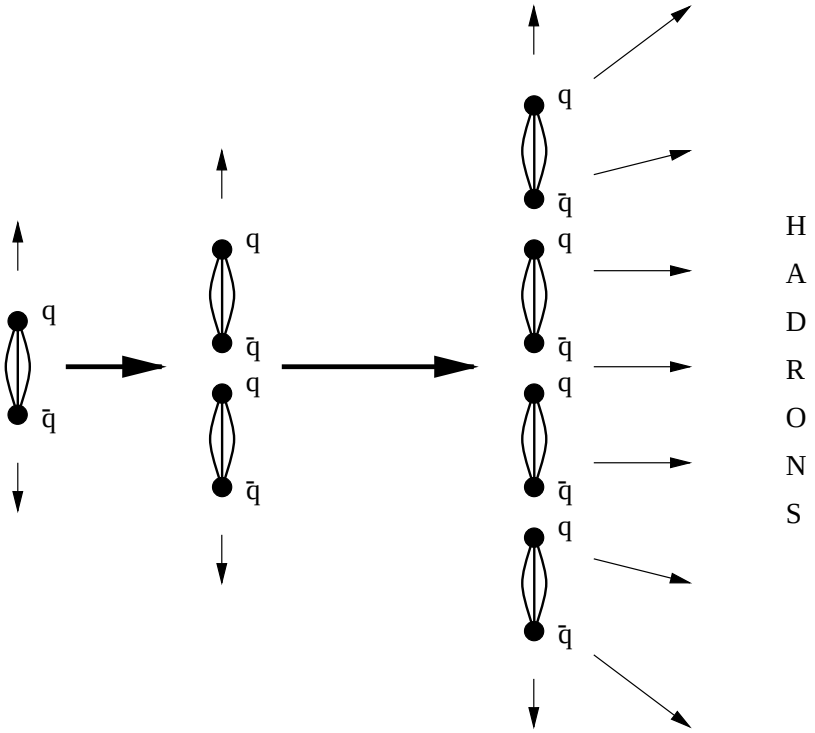

Figure 3.6: *The string fragmentation model.*

Chapter 4

DIS Event and Track Selection

4.1 Introduction

This chapter will investigate several methods of reconstructing kinematic variables and detail event and track selection criteria.

4.2 Reconstruction of Event Kinematics

As the analysis described in this thesis involves a boost into the Breit frame (discussed in the next chapter), it is important to determine the kinematic variables, x and Q^2, with as much precision as possible in order to minimise any uncertainties in the boost. There are several methods [8] which we can utilise to determine the event kinematics, but first it is necessary to introduce the following variables:

$$
\begin{aligned}
E_e &= \text{electron beam energy} \\
E_p &= \text{proton beam energy} \\
E'_e &= \text{energy of scattered electron} \\
\theta_e &= \text{polar angle of scattered electron} \\
\gamma &= \text{polar angle of outgoing struck quark}
\end{aligned}
$$

Using these variables, several methods of determining the event kinematics have been studied.

4.2.1 The Electron Method

With this method, the boost to the Breit frame can be calculated independently of the hadronic system. Using the electron variables:

$$Q_e^2 = 2E_e E'_e(1+\cos\theta_e) \tag{4.1}$$

$$y_e = 1 - \frac{E'_e}{2E_e}(1-\cos\theta_e) \tag{4.2}$$

$$x_e = \frac{E_e E'_e(1+\cos\theta_e)}{E_p(2E_e - E'_e(1-\cos\theta_e))} \tag{4.3}$$

where x_e is obtained from $Q_e^2 = s x_e y_e$.

4.2.2 The Jacquet-Blondel (JB) Method

For charged current (CC) DIS events, where the scattered neutrino goes undetected, the Jacquet-Blondel, or hadrons-only method was developed to determine the event kinematics from the hadronic final state. This method provides a precise measurement of y at low to medium y ($y < 0.2$), which degrades at high y. This method gives a poor measurement of Q^2 due to the loss of hadrons down the beam pipe, but is the only possible method for CC events.

$$y_{JB} = \frac{\Sigma_h(E_h - p_{z,h})}{2E_e} \tag{4.4}$$

$$Q^2_{JB} = \frac{(\Sigma_h p_{x,h})^2 + (\Sigma_h p_{y,h})^2}{1 - y_{JB}} \tag{4.5}$$

$$x_{JB} = \frac{Q^2_{JB}}{s y_{JB}} \tag{4.6}$$

where the subscript h represents hadrons.

4.2.3 The Double Angle (DA) Method

The double-angle (DA) method uses the angle of the scattered electron θ_e, and the inclusive angle of the the hadronic final state γ. Assuming an homogeneous energy measurement over the full solid angle, it can be shown that the DA method is independent of the absolute energy calibration.

$$Q^2_{\theta_e\gamma} = 4E_e^2 \frac{\sin\gamma(1+\cos\theta_e)}{\sin\gamma + \sin\theta_e - \sin(\theta_e+\gamma)} \tag{4.7}$$

$$y_{\theta_e\gamma} = \frac{\sin\theta_e(1-\cos\gamma)}{\sin\gamma + \sin\theta_e - \sin(\theta_e+\gamma)} \tag{4.8}$$

$$x_{\theta_e\gamma} = x_o \frac{\sin\gamma + \sin\theta_e + \sin(\theta_e+\gamma)}{\sin\gamma + \sin\theta_e - \sin(\theta_e+\gamma)} \tag{4.9}$$

where $x_o = E_e/E_p$.

γ can be obtained by inverting the Jacquet-Blondel variables

$$\cos\gamma = \frac{Q^2_{JB}(1-y_{JB}) - 4E_e^2 y^2_{JB}}{Q^2_{JB}(1-y_{JB}) + 4E_e^2 y^2_{JB}} \tag{4.10}$$

4.2.4 The Σ Method

Using the Σ method [40], it is possible to determine y and Q^2 independently of initial state QED radiation by reconstructing the incident electron energy. From energy-momentum conservation, the measured quantity Δ is equal to twice the electron beam energy, if no particles escape detection:

$$\Delta \equiv \Sigma + E'_e(1-\cos\theta_e) = 2E_e \tag{4.11}$$

where $\Sigma = \Sigma_h(E_h - p_{z,h})$.

Substituting Δ into the expression for y_{JB}, we obtain the following:

$$y_\Sigma = \frac{\Sigma}{\Sigma + E'_e(1-\cos\theta_e)} \tag{4.12}$$

$$Q^2_\Sigma = \frac{{E'_e}^2 \sin^2\theta_e}{1 - y_\Sigma} \tag{4.13}$$

$$x_\Sigma = \frac{Q^2_\Sigma}{s y_\Sigma} = \frac{{E'_e}^2 \sin^2\theta_e}{s y_\Sigma (1 - y_\Sigma)} \tag{4.14}$$

4.2.5 The Mixed Method

The mixed method uses the y measurement obtained from JB and Q^2 from the electron. It is particularly useful in that it allows to extend the F_2 measurement done with the DA method or electron method towards lower y.

$$x_{MI} = \frac{Q^2_e}{s y_{JB}} \tag{4.15}$$

4.3 Q^2 and x Resolution

The resolutions in x and Q^2 due to the different reconstruction methods are determined by subjecting reconstructed monte–carlo events to the same series of cuts applied to the real data (no cuts are applied to the generated monte–carlo). The resolutions are measured in terms of Δx and ΔQ^2 given by the following equations:

$$\frac{\Delta x}{x_T} = \frac{x_R - x_T}{x_T} \tag{4.16}$$

$$\frac{\Delta Q^2}{Q^2_T} = \frac{Q^2_R - Q^2_T}{Q^2_T} \tag{4.17}$$

where x_T and Q^2_T are the generated (true) values of x_R and Q^2_R, the reconstructed values determined by each method. The x and Q^2 resolutions from each method can be seen in table 4.1. The table clearly shows that for low Q^2 events, the electron method is by far the best at reconstructing x and Q^2 with the resolution in Q^2 less than 5% and the resolution in x in the region of $20 \rightarrow 30\%$. For high Q^2 events, it can be seen that the Double Angle method is a good rival to the

Electron method for the Q^2 resolution, producing better results in three out of the five high Q^2 bins. For the x resolution, the Electron method is the best in only two out of the five bins. The Sigma method is best in two of the remaining bins, with the Double Angle method producing the best resolution in the remaining bin.

4.3.1 Analysis Bins

For consistency, the analysis bins chosen for this analysis are the same as those used in a previos analysis [46, 51] and are shown in table 4.1. In addition, a further bin has been added in the region $80 < Q^2 < 100$ GeV^2 due to improvements in measuring the energy of the scattered electron in the region between the BEMC and the LAr calorimeter.

4.3.2 Conclusions

Table 4.1 clearly shows that all methods apart from the Jacquet-Blondel method provide a reasonably well reconstructed x and Q^2 measurement. The Mixed method (used only for reconstructing x) is also very poor. However, because the bulk of the data resides at low Q^2 due to the $1/Q^4$ dependence of the DIS cross-section, the electron method is favoured and is used in this analysis.

4.4 Event Selection

In 1994, H1 collected approximately 3.4 pb^{-1} of data of which only a small portion are neutral current (NC) deep inelastic scattering (DIS) events. The events collected by H1 are given an event classification (ECLASS) dependent on the event topology. The classes of interest to this analysis are NCLQSQ and NCHQSQ, Low Q^2 Neutral Current and High Q^2 Neutral current DIS events respectively.

The initial requirements for the event selection are runs which do not have signif-

icant noise in the analogue channels caused by external electrical sources, are of a good quality and were taken when all the high voltage systems of the detector were on. The data are then divided into two samples, low Q^2 (NCLQSQ) and high Q^2 (NCHQSQ). The selection criteria for each sample is detailed below.

4.4.1 Low Q^2 Neutral Current Events

Events must have an electron candidate in the BEMC. The most energetic BEMC cluster must have an energy greater than 8 GeV and be associated with a hit in the BPC. The cluster must be well contained within the BEMC, avoiding regions of poor acceptance such as the innermost part of the BEMC.

The low Q^2 selection requires that the BEMC electron candidate is limited to the region $157^\circ < \theta_e < 172.5^\circ$. The upper limit of 172.5° is to ensure the full containment of the electron shower in the BEMC. The most energetic BEMC cluster must be associated with a space point in the BPC within 5 cm of the weighted cluster centre. The BPC hit must lie less than 60 cm from the beam line which corresponds to the lower angular limit in θ_e of 157°.

4.4.2 High Q^2 Neutral Current Events

Events must have an electron candidate in the barrel or forward region of the LAr. An electron candidate is defined as a reconstructed cluster with an electromagnetic energy fraction of more than 50%. In addition, the event is required to balance in p_t by requiring the missing transverse momenta, p_t^{miss} to be less than 40 GeV. An event is then classified as high Q^2 if there is at least one good central or forward track and the electron candidate is found in either one of the following regions:

- $10^\circ \leq \theta_e \leq 45^\circ$ and $E_t^e \geq 8$ GeV
- $45^\circ \leq \theta_e \leq 160^\circ$ and $E_t^e \geq 5$ GeV

The loose electromagnetic energy fraction and p_t^{miss} cut means that the event classification does not reject many high Q^2 events due to reconstruction and detector effects.

The high Q^2 selection requires the scattered electron to lie within the polar angle $10^\circ < \theta_e < 150^\circ$ for good calorimeter calibration.

4.4.3 Common Event Selection

This section details selection criteria that are performed on both the low and high Q^2 data samples.

- $E'_e > 14$ GeV. In photoproduction events, the electron can scatter through a small angle and disappear down the beam-pipe without being detected. In this case, photoproduction remnants (e.g. low energy pions) can give rise to false, low energy electron candidates.

- $10^\circ < \theta_{quark} < 150^\circ$. The polar angle of the struck quark is calculated using four momentum conservation with the scattered lepton, assuming a massless quark. This selection is used to maintain good detector acceptance.

- $-30 < z_{vertex} < 30$ cm. This requirement ensures that the kinematic variables are well determined from the properties of the scattered electron. The z position of the event vertex is provided by the H1 tracking system.

- Removal of diffractive events. Most DIS events have considerable energy deposits in the forward region of the detector. However, around 6% of DIS events have very little forward energy. These events stem from diffractive like processes which are not included in the standard QCD models used in this analysis, and so are removed from the sample. To remove these diffractive-like events, we demand that for each event, the summed calorimetric energy in the forward region of the LAr, $(4.4^\circ < \theta_{LAr\ cluster} < 15^\circ)$ has to be greater than 0.5 GeV.

- $W^2 > 4400$ GeV^2. To minimise QED radiative corrections in the problematic low y region, the sum of the invariant mass of the hadronic system, W^2 (calculated using both the electron and Jacquet-Blondel methods), is required to be larger than 4400 GeV^2.

4.5 Track Selection

The H1 tracking system (as described earlier), consists of a central and forward tracking system. Tracks which originate from the primary vertex are referred to as primary tracks, whilst secondary tracks are associated with secondary vertices from, for example, K^0_S decays or background interactions.

Tracks which pass through the central tracking system only are subject to central track selection whilst those which pass through the forward tracker are subject to forward track selection. Tracks which pass though both the central and forward tracker are subject to a 'combined' track selection. The rest of this section describes the necessary track selection criteria required to select primary charged tracks originating from the interaction point [41].

4.5.1 Central Track Selection

1. $p_t^{min} > 0.15$ GeV. This cut ensures that tracks can pass through both chambers of the CDC avoiding reconstruction problems where the track finding efficiency deteriorates because of low momentum tracks curling back on themselves.
2. $\theta < 158°$. No restriction is placed on the polar angle of a track.
3. $\mathrm{DCA}_{\mathrm{max}} < 2.0$ cm. The track has to be constrained to the vertex with a distance of closest approach in the $x-y$ plane to the z axis (DCA) less than 2.0 cm. The z-coordinate of that point is Z_0 and the track is further required to point in the local region of the vertex position, Z_{vertex}, such that $|Z_0 - Z_{vertex}| \leq 30.0$ cm.

4. Length > 10.0 cm. This essentially removes points that are not from the same track and are associated randomly.

5. $\delta p/p < 1.0$. The momentum of a track is determined by its curvature in the magnetic field of the tracking system. Energetic tracks will have very little curvature and the momentum error, $\delta p/p$, will be large.

4.5.2 Forward Track Selection

1. $p^{min} > 0.5$ GeV. This cut is used to suppress low momentum scattering in non-sensitive materials in or between different sub-detectors such as the end wall of the CJC.

2. $\delta p/p < 1.0$. (see above)

3. $8^\circ < \theta < 30^\circ$

4. $R_0 < 2.0$ cm. To see if the track extrapolates close to the vertex, the distance in the $x-y$ plane between the track and the vertex, R_0, must be less than 2.0 cm.

5. $\chi^2_{vertex\ fit} < 10$. The $\chi^2_{vertex\ fit}$ is used to determine whether the track originates from the primary vertex. Tracks with large χ^2 have a low probability of originating from the vertex and are therefore discarded.

6. $\chi^2_{track\ fit} < 25$. This cut is used to suppress tracks that have been associated with wrong hits in the forward tracker.

7. There must me at least one primary segment from the planar chambers, as these are much less contaminated by random signals than the radial segments.

4.5.3 Combined Track Selection

Combined tracks are those tracks which pass through both the central and forward track detectors.

1. $p_t^{min} > 0.15$ GeV
2. $5.7^\circ < \theta < 34.4^\circ$
3. $\chi^2_{vertex\ fit} < 10$
4. $\chi^2_{link\ fit} < 25$
5. $\delta p/p < 1.0$

4.6 Summary

Plots of event and track variables for both data and reconstructed monte–carlo after the selection criteria have been applied can be seen in Figures 4.6 and 4.7. It is clear from these plots that after the event and tack selection criteria have been applied, data and monte–carlo are in good agreement with one another.

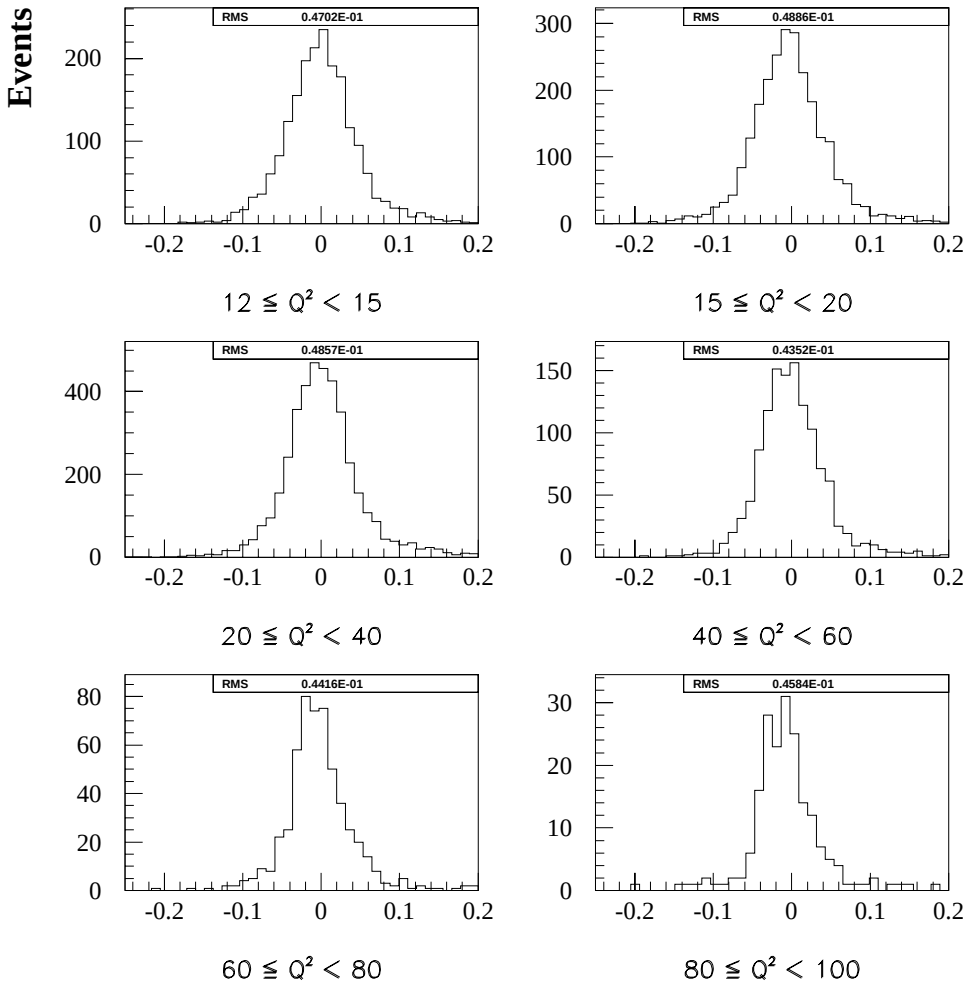

Figure 4.1: $\Delta Q^2/Q^2$ *for the low* Q^2 *monte–carlo using the Electron Method.*

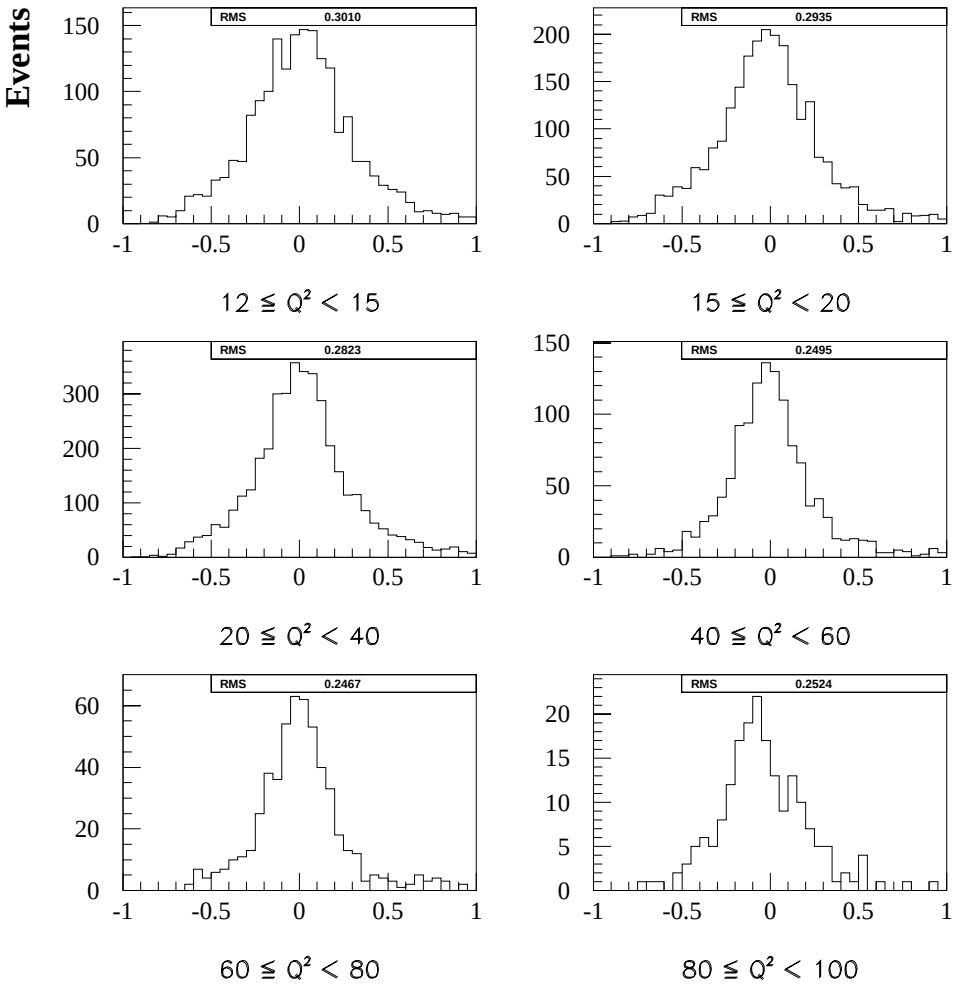

Figure 4.2: $\Delta x/x$ *for the low* Q^2 *monte–carlo using the Electron Method.*

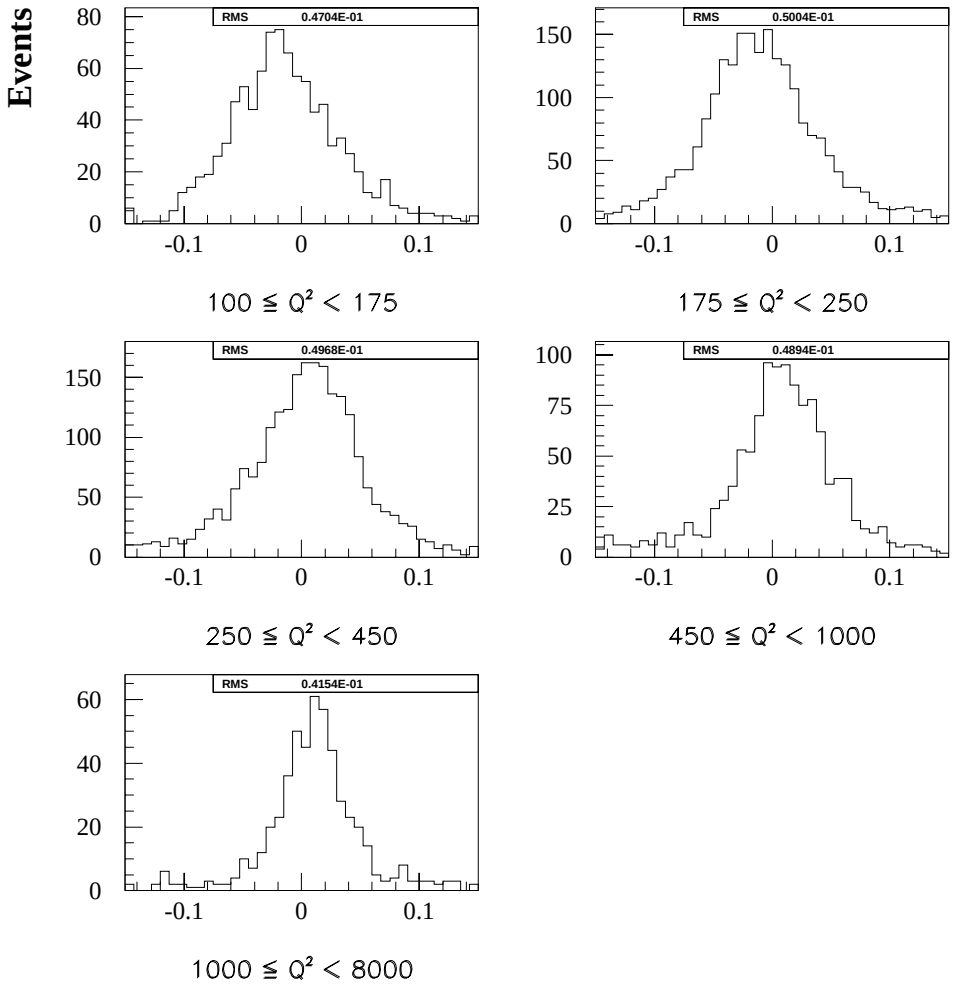

Figure 4.3: $\Delta Q^2/Q^2$ *for the high* Q^2 *monte–carlo using the Electron Method.*

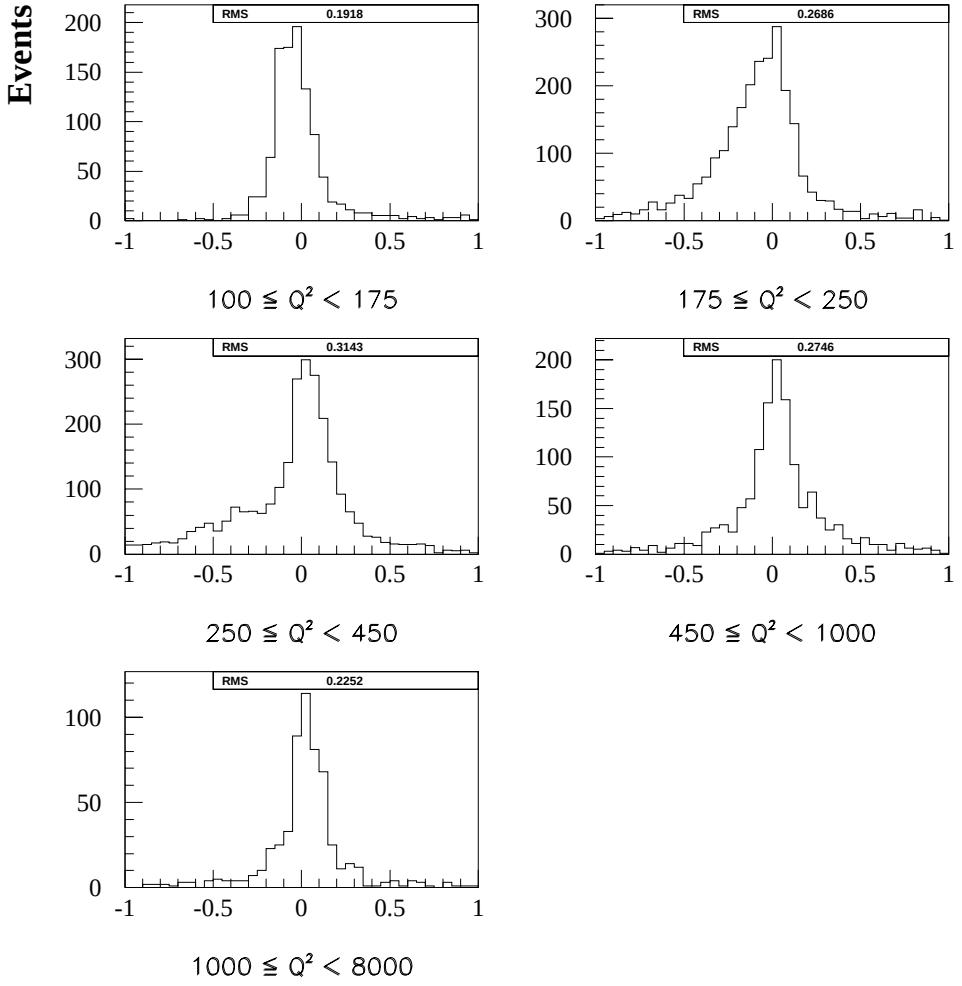

Figure 4.4: $\Delta x/x$ *for the high* Q^2 *monte–carlo using the Electron Method.*

Q^2 Interval	$\Delta Q^2/Q_T^2$ %				$\Delta x/x_T$ %				
(GeV^2)	EL	DA	Σ	JB	EL	DA	Σ	MI	JB
12-15	4.7	6.7	6.4	60.9	30.1	56.7	39.9	59.3	70.8
15-20	4.9	6.3	6.7	59.5	29.4	51.0	39.8	58.8	65.3
20-40	4.9	6.4	6.9	55.3	28.2	48.0	38.1	56.7	60.6
40-60	4.4	6.1	7.0	48.9	25.0	41.4	34.0	50.7	54.4
60-80	4.4	5.7	6.8	42.9	24.7	37.9	34.2	52.2	46.0
80-100	4.6	4.7	6.1	43.3	25.2	36.9	28.7	43.4	46.6
100-175	4.7	6.2	10.6	49.7	19.2	28.4	23.2	40.3	58.1
175-250	5.0	4.6	9.4	43.7	26.9	26.9	26.2	37.7	51.9
250-450	5.0	4.4	9.6	44.2	31.4	28.2	26.7	36.4	47.8
450-1000	4.9	4.4	10.1	45.4	27.5	25.6	28.2	38.8	44.7
1000-8000	4.2	4.9	10.0	40.6	22.5	29.6	34.1	49.0	44.4

Table 4.1: *Percentage error in x and Q^2 for the Q^2 bins of this analysis.*

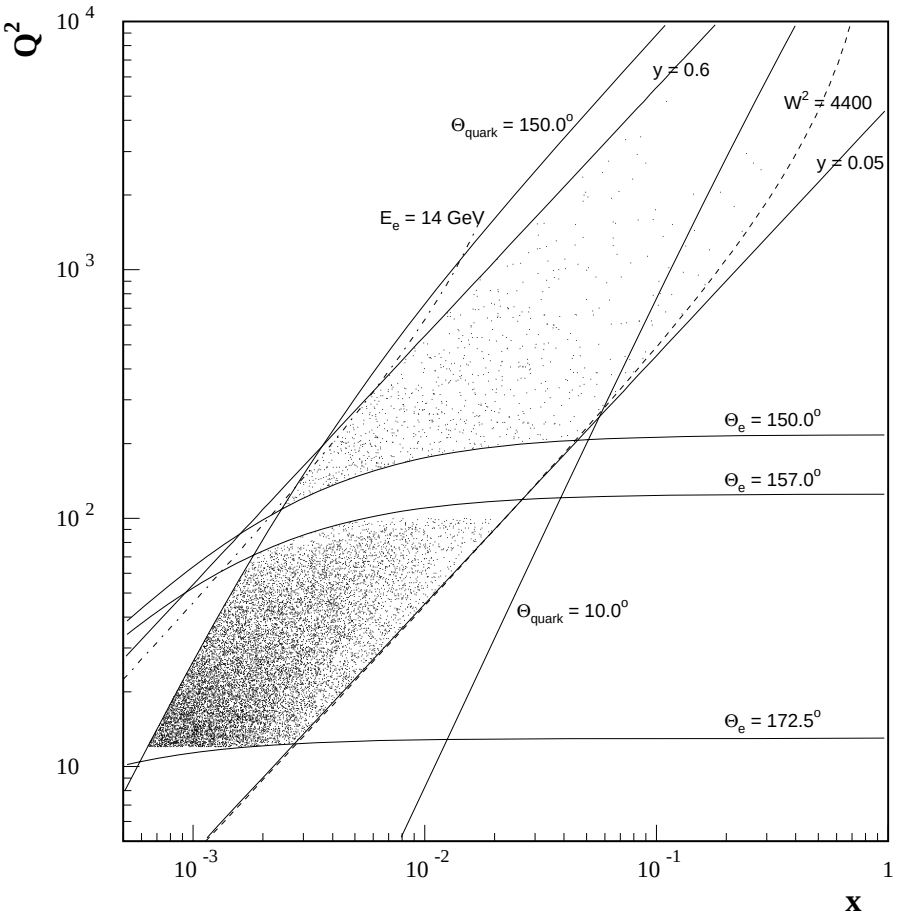

Figure 4.5: *HERA kinematics (calculated via the electron method) available in 1994 data. The data are split into two samples - the low Q^2 sample in the lower half of the plot and the high Q^2 sample in the upper half of the plot. The various lines indicate the cuts used to select events in this analysis.*

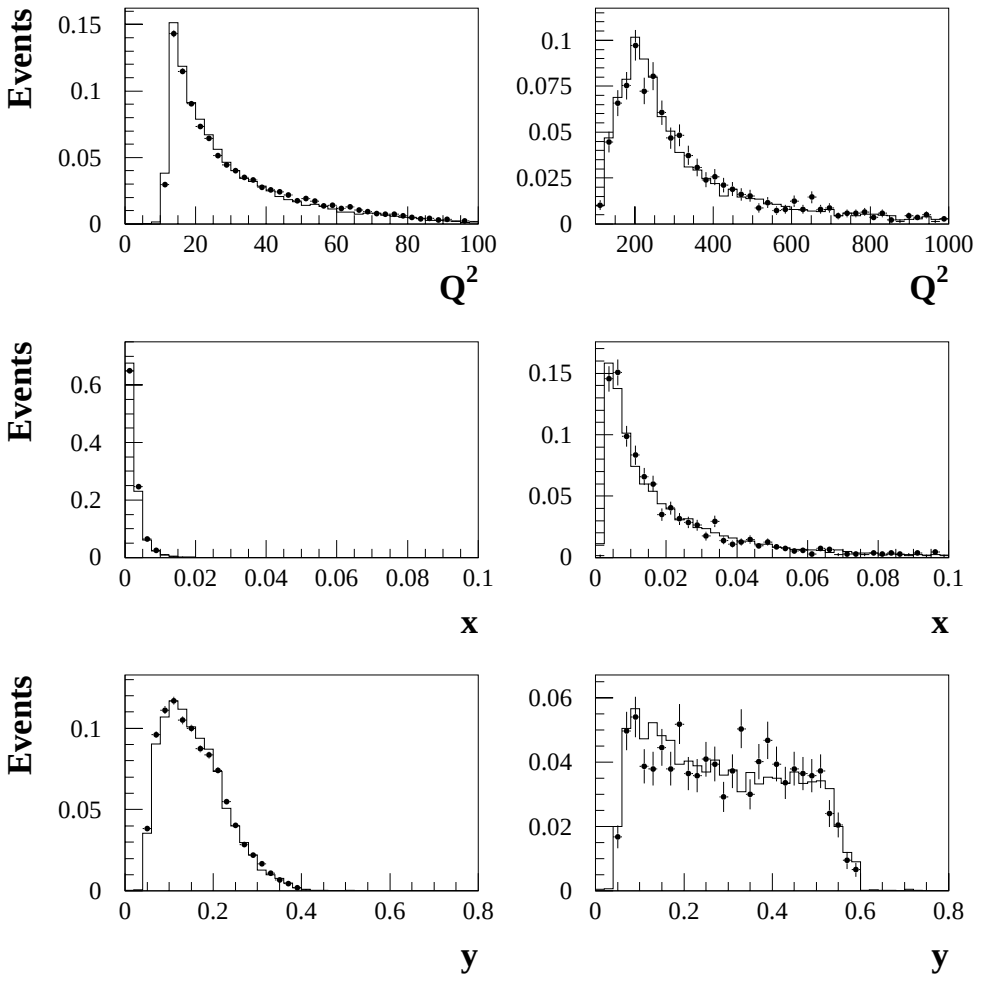

Figure 4.6: *Plots of event variables after the data selection described in this chapter for the low Q^2 (left) and high Q^2 (right) data samples (solid circles). The solid line is reconstructed DJANGO monte-carlo with the same data selection.*

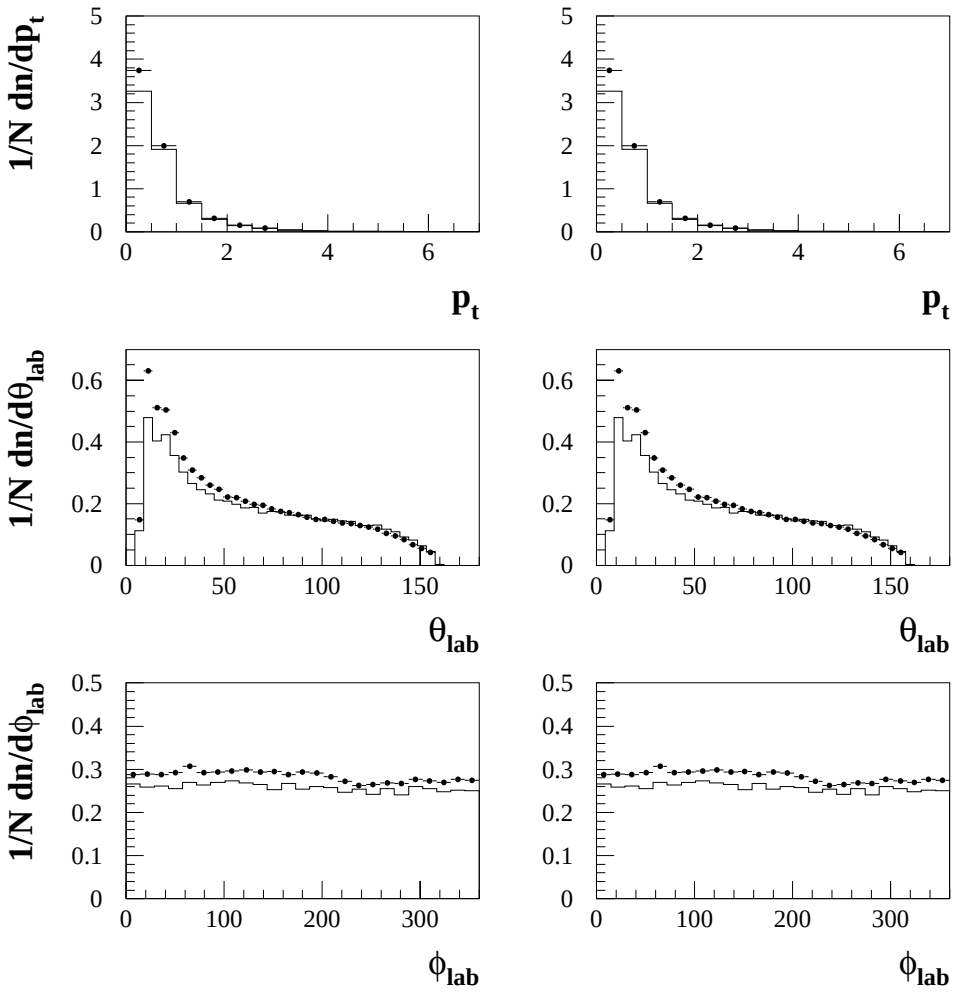

Figure 4.7: *Plots of track variables after the data selection described in this chapter for the low Q^2 (left) and high Q^2 (right) data samples (solid circles). The solid line is reconstructed DJANGO monte–carlo with the same data selection. It can clearly be seen that the monte–carlo under–estimates the multiplicity in the forward region. However, only the highest Q^2 bin in this analysis has a contribution ($\approx 8\%$) of tracks from the forward tracking detector.*

Chapter 5

The Breit Frame

5.1 The Breit Frame of Reference

The ep Breit frame is collinear with the hadronic centre of mass (HCM) but boosted along a common z direction such that the incident virtual photon has zero energy, zero transverse momentum and a z component of momentum $-Q$. As with the laboratory frame of reference, we choose the positive z axis to be in the direction of the incoming proton. The negative z direction is referred to as the 'current' hemisphere of the interaction. A previous Breit frame analysis [46] showed that multiplicities in the current region of the Breit frame depend on Q and not on Bjorken x ($\sim Q^2/W^2$), as opposed to the HCM where multiplicities depend on the natural scale, W [42]. In the naïve quark parton model (QPM) the massless incoming quark has energy $Q/2$ and z component of momentum $+Q/2$, carrying a fraction x of the proton's momentum. After scattering it still has energy $Q/2$, with momentum $-Q/2$, Figure 5.1. By comparison, we thus take the equivalent to the e^+e^- centre of mass energy, E^*, to be Q.

It can be shown [43] that the simultaneous agreement of average charged track multiplicities in the 'current hemisphere' of the Breit frame with e^+e^- results at $E^* = Q$, and multiplicities in the 'current hemisphere' of the hadronic CMS with e^+e^- results at $E^* = W$, are a result of Feynman scaling [28]. The flat

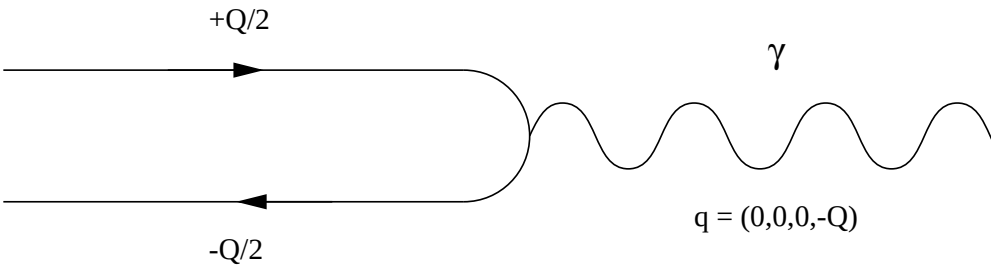

Figure 5.1: *The Breit frame.*

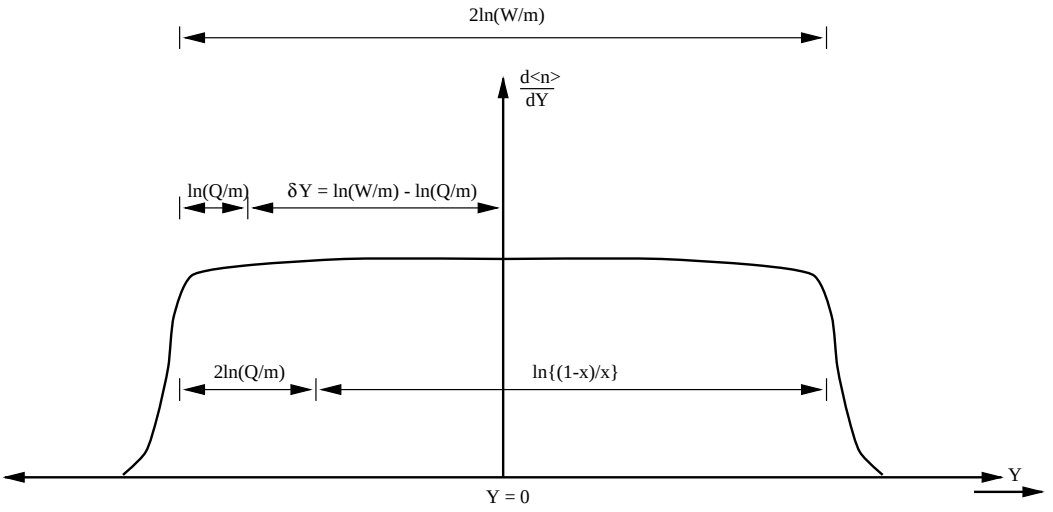

Figure 5.2: *A simplified version of the rapidity distribution as seen in the hadronic CMS system.*

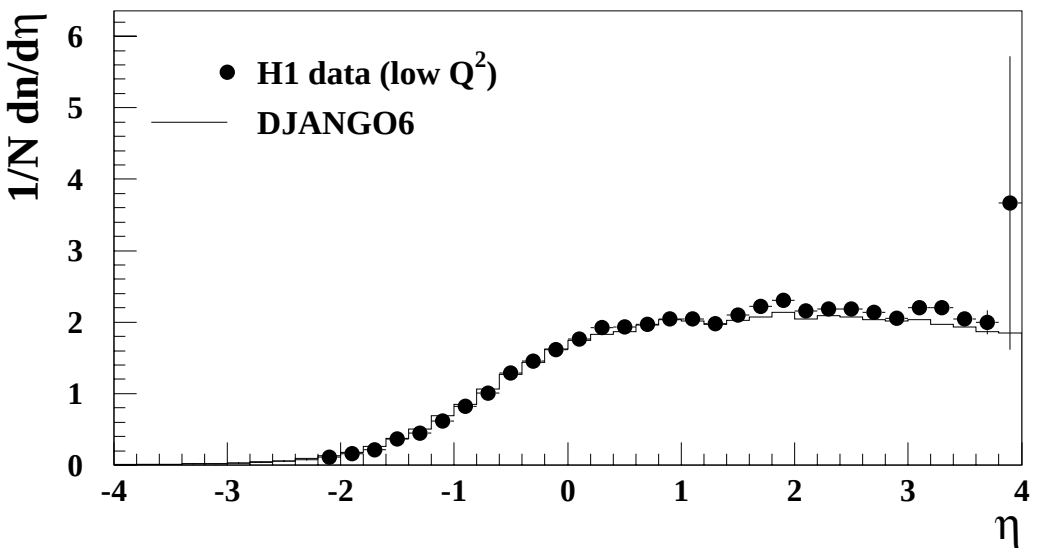

Figure 5.3: *A pseudo-rapidity distribution as seen in the Breit frame for the low Q^2 data sample (solid circles) along with the predictions of the DJANGO Monte Carlo. The Breit fame origin is at $\eta = 0$.*

rapidity plateau for particles of mass m at a centre of mass energy W expected as a result of limited p_t interactions has a total width of $\Delta Y = 2\ln(W/m)$ [44]. The expression (neglecting the mass of the proton) $W^2 = Q^2(1/x - 1)$ where x is the Bjorken scaling variable, gives us $2\ln(W/m) = 2\ln(Q/m) + \ln((1-x)/x)$. We can thus picture a rapidity plateau (Figure 5.2) made up of the partitions shown. In this picture, the area to the left of $Y = 0$ gives the observed multiplicity in one hemisphere of the hadronic CMS. The simplified version depicted here indicates the same multiplicity in both hemispheres. For the following scaling argument to hold it is only necessary for the plateau height to be approximately constant within one half hemisphere, Figure 5.3.

Given such a flat plateau, the ratio of the multiplicity in the rapidity interval $\ln(W/m)$ to that in the rapidity interval $\ln(Q/m)$ is simply $\ln(W/m)/\ln(Q/m)$, which is what we would expect as a ratio of the multiplicities of e^+e^- events at two different energies (given a simple logarithmic dependence on E^* [52]). It can be shown [43] that the $Y_{BF} = 0$ point occurs at a shift from $Y = 0$ of $\delta Y = (\ln(W/m) - \ln(Q/m)) = (\ln W - \ln Q)$ (assuming $m << W, Q$) which

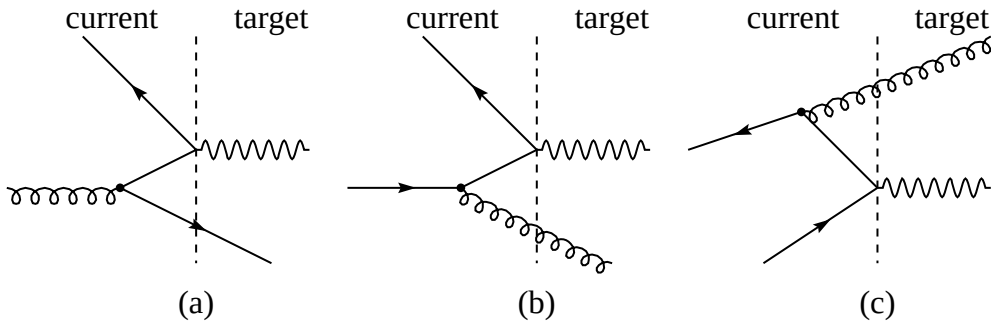

Figure 5.4: *The current hemisphere of the Breit frame can be depleted by higher order QCD processes: BGF events (a) and Initial State QCDC (b) do not occur in e^+e^- events. However, Final State QCDC (c) occurs in both e^+e^- and ep collisions.*

proves simultaneous first order agreement of Breit frame current hemisphere multiplicities with e^+e^- data at $E^* = Q$ and CMS current hemisphere multiplicities with e^+e^- data at $E^* = W$.

Compared with the HCM the Breit frame current hemisphere is dominated by the fragments of the struck quark alone - the 'spectator' proton remnants go entirely into the 'target' hemisphere with much higher momentum. There is excellent acceptance for the current hemisphere in the central H1 detector. For example, even in the highest Q^2 interval of this analysis there is only an $\sim$8% contribution of tracks from the Forward Track Detector. The HCM current hemisphere, in contrast, has an energy scale of $W/2$ rather than $Q/2$ and generally can not be seen in its entirety. This makes comparisons with a complete e^+e^- interaction hemisphere somewhat easier in the Breit frame.

5.2 Higher Order Processes in the Breit Frame

When QCD corrections to the parton model are taken into account, the masses of the $q\overline{q}$ pairs produced is not negligible. QCD also introduces the possibility for qg pairs to be produced. BGF and initial state QCDC (processes which have no analogue in e^+e^- interactions) are also present. These processes, along with

final state QCDC (which does occur in e^+e^- interactions) can de-populate the current region of the Breit frame [45], leading to a current hemisphere which may be empty, Figure 5.4. Empty current hemispheres are included in this analysis.

Chapter 6

Track Quantities, Resolutions and Corrections

6.1 Introduction

This chapter will introduce the track quantitites used in this analysis and investigate their resolutions. The results of the resolution studies will motivate the method chosen to correct distributions of these quantities for detector acceptance.

6.2 Separation of the Current and Target Hemispheres

Track properties in the Breit frame are investigated starting with the cosine of the polar angle for charged tracks, $cos\theta_B$. Distributions for both the low and high Q^2 data samples are shown in figure 6.1. Charged tracks are assigned to the current fragmentation region by their longitudinal momentum component in the Breit frame, $p_z < 0$ ($cos\theta_B < 0$) which defines the z axis. The distributions show an obvious peak in the positive-z (beam) direction and in the negative-z (quark) direction, particularly at high Q^2.

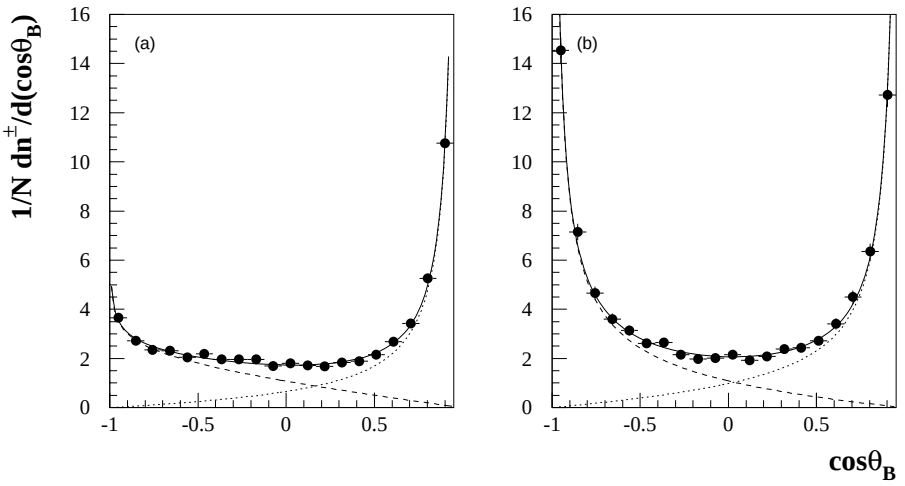

Figure 6.1: *The cosine of the Breit frame polar angle for tracks of (a) the low Q^2 and (b) the high Q^2 data samples with statistical errors only. The solid line corresponds to the empirical fit described by equation 6.2 where the dashed line corresponds to the nominal quark contribution and the dotted line that of the target.*

It is clear from Figure 6.1 that two distinct regions (current and target) exist. The problem arises, however, on how we separate the current and target hemispheres at low Q^2. To estimate the possible losses and contamination involved in selecting one of the Breit frame hemispheres as a result of poor resolution, two methods were investigated.

6.2.1 Resolution in $cos\theta_B$

The first investigation seeks to see what the net migration/immigration into a region caused by poor resolution of the kinematic variables. The accuracy of the boost to the Breit frame is dependent on the correct reconstruction of the kinematic quantities x and Q^2. If the reconstructed quantities deviate from the true (generated) values, then the reconstructed and true axes will not coincide. In such cases, particles which were generated with $p_z < 0$ can have $p_z > 0$ viewed in the reconstructed frame.

The level of migration due to detector resolution effects was investigated using the DJANGO Monte–Carlo [53]. The generated energy and momentum components of stable charged hadrons were boosted into the Breit frame using the generated virtual photon and the virtual photon reconstructed from the scattered electron quantities. Table 6.1 presents the number of particles generated in the current and target regions and the number of particles that migrate from one region to the other due to boost reconstruction. Table 6.1 shows that in the current region, $< 12\%$ of the particles generated in the current hemisphere migrate into the target region. This percentage is Q^2 dependent and generally becomes smaller as Q^2 increases. The percentage of generated particles in the target region which migrate to the current region, however, is generally constant and less significant at $< 2\%$.

The resolution of $cos\theta_B$ is dominated by the boost to the Breit frame and can be found from

$$\sigma_{boost}(cos\theta_B) = rms(cos\theta_B^{rpge} - cos\theta_B^{rpre}) \tag{6.1}$$

Q^2 Interval	Current Hemisphere		Target Hemisphere	
(GeV^2)	Generated	Migrate to Target	Generated	Migrate to Current
12-15	1547	181	20116	263
15-20	2413	268	26020	341
20-15	5362	479	45704	689
40-15	2536	205	15545	225
60-15	1232	86	6786	83
80-100	533	43	2364	38
100-175	2991	181	14238	147
175-250	7148	816	27292	303
250-450	8533	714	27411	603
450-1000	5901	431	14862	358
1000-8000	3507	122	6520	126

Table 6.1: *Particle migrations studied using the DJANGO Monte–Carlo at the generated level*

where $cos\theta_B^{rpge}$ is measured using the reconstructed particles boosted to the Breit frame with the *generated* virtual photon. $cos\theta_B^{rpre}$ is measured using reconstructed particles boosted to the Breit frame using the *reconstructed* virtual photon. The resolution due to the boost is shown in figure 6.2(a,b) and is $\approx 0.18(0.16)$ at low (high) Q^2.

6.2.2 Empirical Fits

The second investigation assumes there are two coherent sources of hadronic fragments, the current and the target. These sources produce hadrons on either side of $cos(\theta_B) = 0$ in the Breit frame due to poor resolution. An empirical fit [51] is performed to the data of the form:

$$f(x) = \underbrace{A(1-x)e^{a(1+x)^{\alpha}}}_{current} + \underbrace{B(1+x)e^{b(1-x)^{\beta}}}_{target} \tag{6.2}$$

where $x = cos\theta_B$.

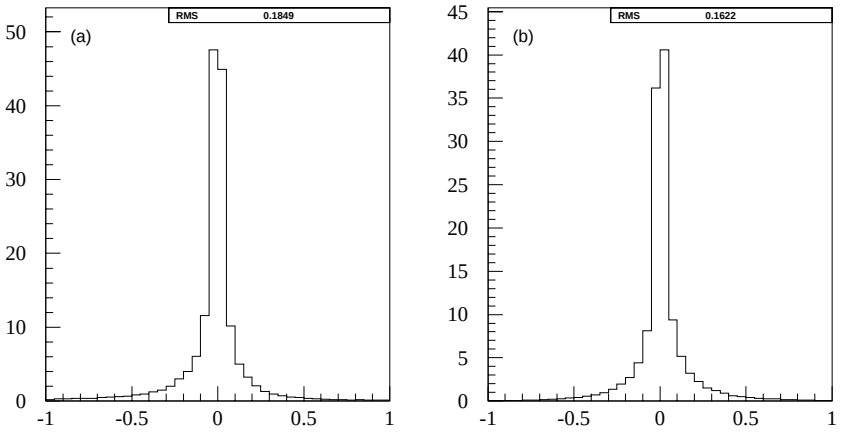

Figure 6.2: *The resolution of $cos\theta_B$ due to the boost to the Breit frame for (a) the low Q^2 and (b) the high Q^2 data samples.*

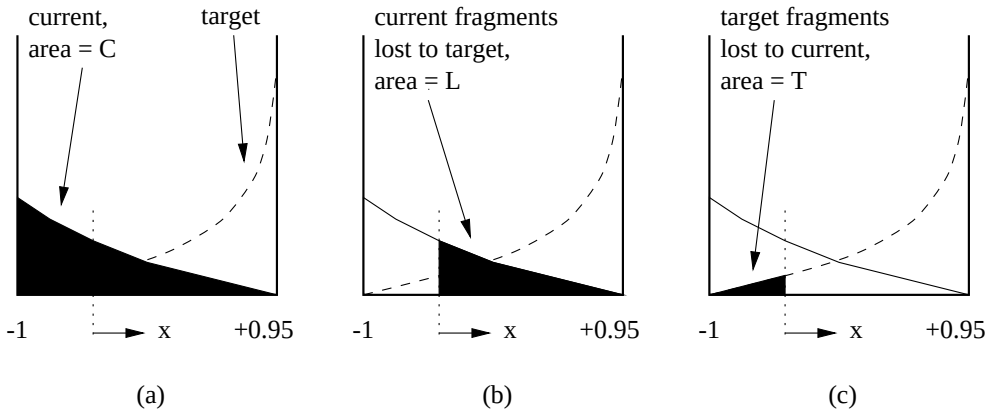

Figure 6.3: *An empirical fit is used to describe the current and target. In (a), the current (solid line) and target (dashed line) are shown as a function of $x = \cos\theta_B$. The area indicated in (a) is the total average charged multiplicity associated with the current quark. The area shown in (b) is the average charged multiplicity lost to the target region - a consequence of defining one section of the Breit frame to represent the quark fragmentation region (the area to the left of the dotted line). In (c), the shaded area shows the tail of the target related fragments which contaminate the current region.*

This fit suggests that, in the Breit frame, the selection $cos\theta_B = 0.0$ roughly equalises loss and contamination between the quark (current) and target regions and that they are $\approx 5\%$ at high Q^2 and $\approx 20 - 25\%$ at low Q^2.

6.3 Fragmentation Functions

The momentum distribution of the hadrons from quark fragmentation in e^+e^- interactions scales roughly with $\sqrt{s_{ee}} = E^*$, the overall centre of mass (CMS) energy. The ratio of the momentum of a given charged hadron to the maximum energy that the hadron could have, $x_p = 2p^{\pm}_{hadron}/E^*$ is a variable in which e^+e^- experiments have described hadronic spectra. In the Breit frame, the equivalent variable is $x_p = 2p^{\pm}_{hadron}/Q$, where $Q \equiv E^*$ [46]. The distribution is defined as

$$D^{\pm}(x_p) = (1/N) \times dn^{\pm}_{tracks}/dx_p \tag{6.3}$$

which is an event normalised charged track density termed the fragmentation function.

The fragmentation function is a 'soft' function, rising rapidly as x_p decreases then turning over near $x_p = 0$. Figure 6.4 shows the fragmentation functions for the low and high Q^2 data samples.

Changing the fragmentation variable to $\xi = \ln(1/x_p)$ expands the turn over region and the Modified Leading Log approximation (MLLA) to perturbative QCD predicts that for partons, the shape of the ξ distribution is approximately Gaussian. Assuming Local Parton Hadron Duality (LPHD), the same behaviour is expected for hadrons. Redefining the fragmentation function to be $D(\xi) = (1/N) \times dn^{\pm}_{tracks}/d\xi$ results in the Gaussian shape of Figure 6.5. As Q^2 increases, the area under the fragmentation function (average multiplicity) increases, as does the mean value of ξ. Figure 6.6 clearly shows that the fragmentation functions for reconstructed DJANGO events describe the data shown in Figure 6.5.

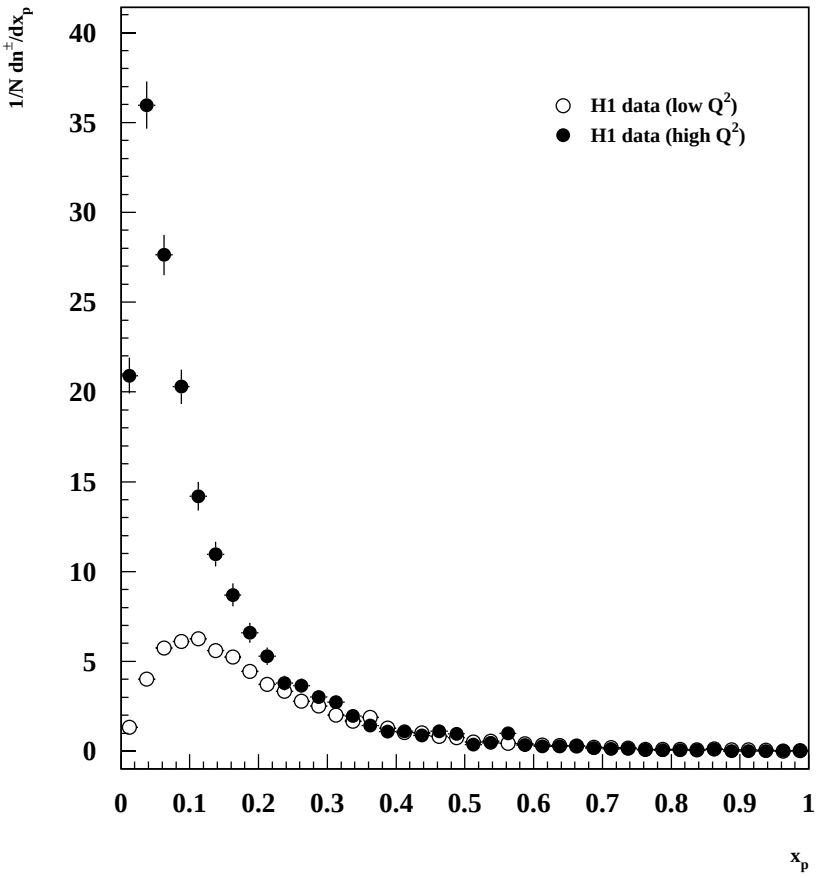

Figure 6.4: *The fragmentation functions,* $1/N dn^{\pm}/dx_p$*, for the current hemisphere of the Breit frame (statistical errors only).*

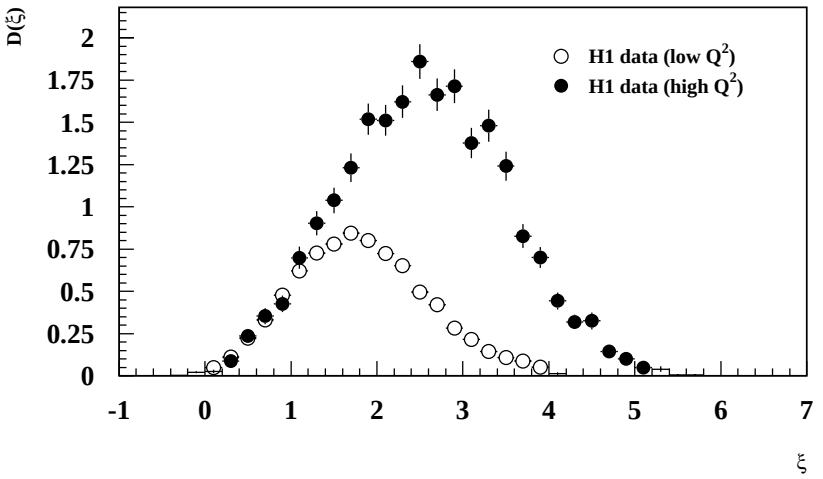

Figure 6.5: *The fragmentation functions, $D(\xi)$, for the current hemisphere of the Breit frame (statistical errors only).*

6.4 Resolution in x_p and ξ

As with $cos\theta_B$, the resolution of both ξ and x_p consists of a small contribution from track reconstruction and a large contribution from boost reconstruction. The boost resolutions for x_p and ξ in the current region of the Breit frame are shown in Figures 6.7 and 6.8 respectively. The bin widths of x_p and ξ have been chosen to be commensurate with these resolutions.

6.5 Data Correction

In this thesis, all distributions relating to event properties are normalised by the number of events in a given analysis bin and are corrected for detector acceptance effects. As the analysis bins of the track quantities used in this analysis are well within their individual resolutions, the bin-by-bin method has been chosen.

To correct for acceptance losses, we utilise the DJANGO6 [53] Monte–Carlo event generator. This combines a leading order perturbative QCD matrix element cal-

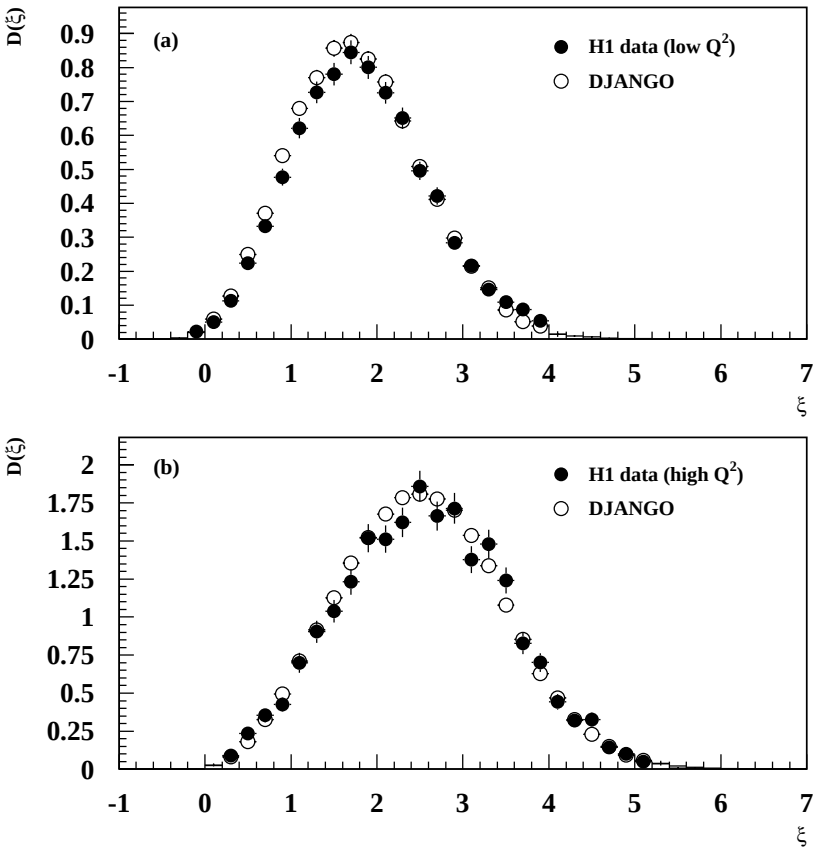

Figure 6.6: *The fragmentation functions, $D(\xi)$, for the current hemisphere of the Breit frame compared with the DJANGO Monte–Carlo for (a) the high Q^2 and (b) low Q^2 data samples (statistical errors only).*

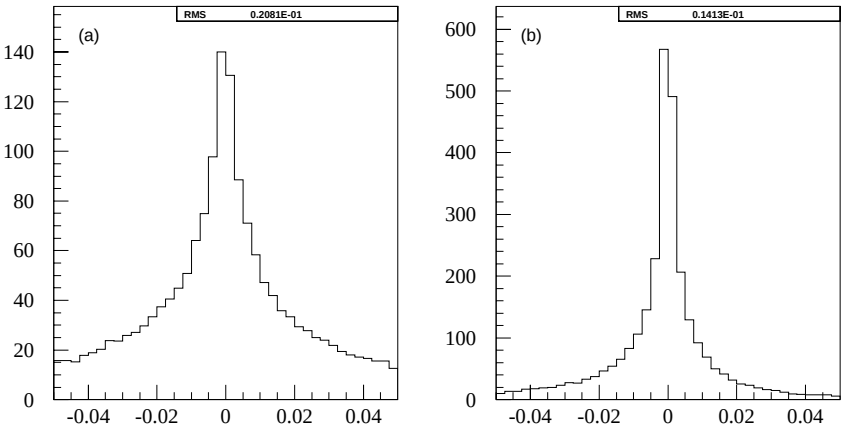

Figure 6.7: *The resolution of x_p due to the boost to the Breit frame for (a) the low Q^2 and (b) the high Q^2 data samples.*

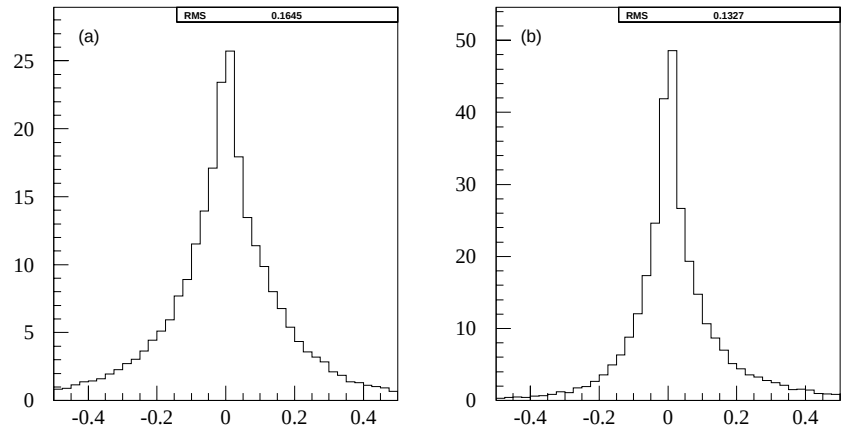

Figure 6.8: *The resolution of ξ due to the boost to the Breit frame for (a) the low Q^2 and (b) the high Q^2 data samples.*

culation and the colour dipole model of hadronisation with a calculation of QED radiative effects. Radiative effects remaining after our event selections have been corrected by comparing results of Monte–Carlo calculations with and without the inclusion of QED radiative effects which are at the few percent level. The correction function, C_i, for the i^{th} bin in a distribution is thus

$$C_i = \frac{n^{gen}_{non-radiative}}{n^{rec}_{radiative}} \tag{6.4}$$

where n is the number of entries in the i^{th} bin of the distribution.

For the reconstructed Monte–Carlo, the detector response is simulated using a program based on the GEANT [19] package. The simulated events are reconstructed and selected using exactly the same analysis chain as used on real data.

The total bin-by-bin corrections made throughout this thesis are generally well within $\pm 20\%$ and vary smoothly in any given distribution.

Chapter 7

Charged Particle Spectra in the Breit Frame

7.1 Introduction

The fragmentation properties of the partons that form the current jet are studied in the Breit frame of reference and compared with one hemisphere of an e^+e^- annihilation interaction. The equivalent to the e^+e^- centre of mass energy, E^*, is taken to be Q, where $q^2 = -Q^2$ is the square of the four-momentum transferred from the incident lepton.

In the context of the naïve quark parton model (QPM), the massless incoming and exiting quark has energy and magnitude of momentum $Q/2$, and a fraction of the proton's momentum given by the invariant Bjorken x. As compared to the Hadronic Centre of Mass system (HCM) the Breit frame thus concentrates on that kinematic area characteristic of the scattered quark only, the 'spectator' proton remnants falling entirely into the 'target' hemisphere. There is almost 100% acceptance of the current hemisphere for HERA detectors.

7.2 Evolution of the Fragmentation Function with Q

The data have been divided into 11 intervals of Q^2 as described in chapter 4. This allows us to the study the scaling properties of x_p and the evolution of the area, peak and width of $\ln(1/x_p)$ with Q.

7.2.1 Scaling Violations of the Fragmentation Function

At high energies and for light final state particles, the fragmentation function, rising rapidly at small x_p and turning over just before $x_p = 0$, approximately scales with Q. As the energy imparted to the initial parton increases, $D(x_p, Q^2)$ evolves into a softer function with increased probability for low x_p hadrons at the expense of high x_p hadrons. The evidence for this scaling *violation* may be seen in Figure 7.1 where the fragmentation function is plotted as a function of Q for different intervals of x_p and compared with equivalent data from e^+e^- experiments [52] plotted as a function of $E^\star$. Most published e^+e^- results refer to *event* multiplicities. Here, as elsewhere in this analysis, track multiplicity data from e^+e^- experiments have been halved to correspond to results for each *quark*.

Figure 7.1 also displays a prediction from a leading order Monte Carlo (DJANGO6) [53] calculation. The scaling violation effect is directly comparable with the scaling violations in structure function studies [59].

A next to leading order (NLO) calculation, as implemented in CYCLOPS [56], may be used to test perturbative QCD. The scale evolution of fragmentation functions is governed by a renormalisation group equation [58]:

$$\frac{\partial D_{h/j}(z,\mu_D^2)}{\partial \ln \mu_D^2} = \frac{\alpha_s(\mu_D^2)}{2\pi} \int_z^1 \frac{\mathrm{d}u}{u} K_{k\leftarrow j}\left(u, \alpha_s(\mu_D^2)\right) D_{h/k}\left(\frac{z}{u}, \mu_D^2\right) \qquad (7.1)$$

In DIS, the scaling variable, μ_D, has to be the photon virtuality Q. The total hadronic energy, W, cannot be used as it is not directly related to the hard

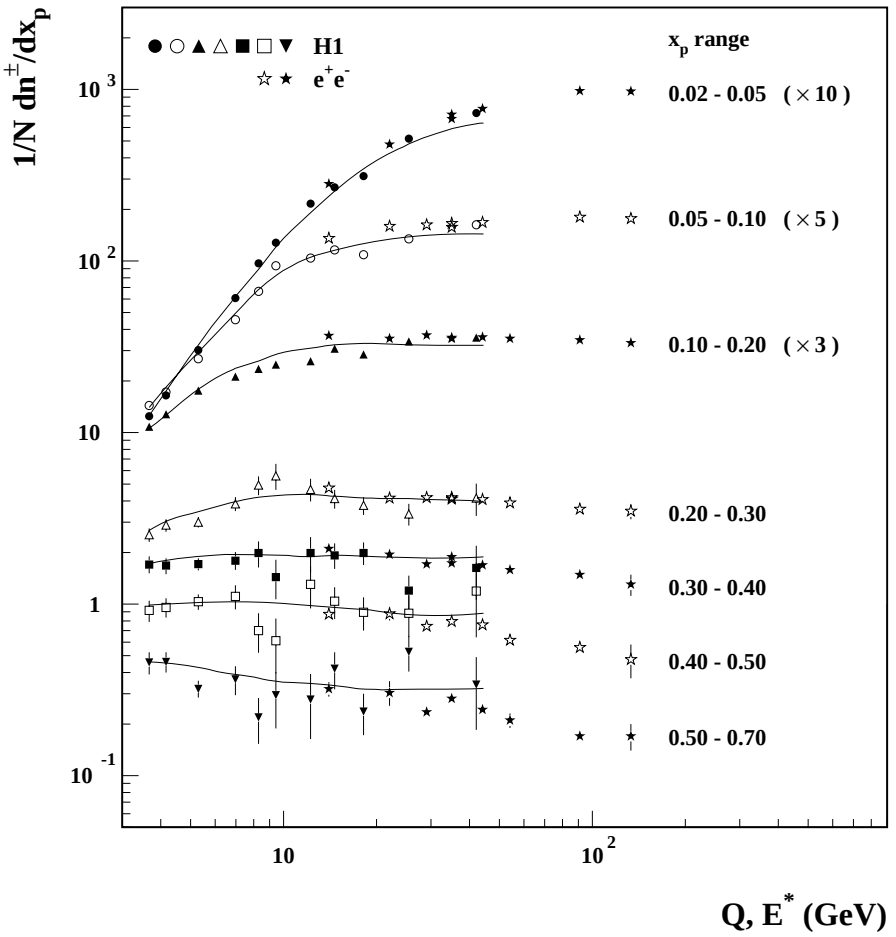

Figure 7.1: *Scaling violations of the fragmentation function shown as $F(Q)$, or $F(E^*)$ for e^+e^- results (starred symbols), within the indicated intervals of the scaled momentum, x_p. Statistical and systematic errors are added in quadrature. The solid line indicates the prediction of a leading order Monte–Carlo, DJANGO6.*

scattering process because it contains contributions from the proton remnant jet. Thus, a multi-parameter fit of fragmentation functions over a wide range of Q would permit a determination of the fundamental QCD parameter $\Lambda_{\overline{MS}}$.

However, the comparison of theory with data breaks down at small x_p (of the order of 0.1) and at small Q^2 ($Q^2 < 100$ GeV^2) even for moderate x_p [57]. This is the case because, looking at rapidities in this kinematical regime, the particle is not a fragmentation product of the current quark, but is produced somewhere during the "initial state radiation" process. Thus, the fragmentation function formalism has to fail [57]. Such an analysis will, therefore, require high statistics due to the $1/Q^4$ dependence of the DIS cross-section.

7.2.2 Multiplicity Evolution of the Fragmentation Function

The integrated area of the fragmentation function for any given Q^2 interval gives the average charged track multiplicity (ACM) of events in that interval. By plotting the area of the fragmentation function as a function Q, we can see the energy dependence of the ACM. As one would expect, the ACM increases with energy as shown in Figure 7.2. A table of the results are presented in Table 7.7

In e^+e^- experiments, there are a number of phenomenological models [49] which propose to describe the energy evolution of the average charged track multiplicity. An empirocal curve fit using the following function:

$$< n_{ch} >= a + by + cy^2 + dy^3 + ey^4 + fy^5 + gy^6 \tag{7.2}$$

where $y = 2\ln(E^\star)$ and $a = 1.574$, $b = -0.317$, $c = 0.228$, $d = -3.222 \times 10^{-2}$, $e = 4.614 \times 10^{-3}$, $f = -2.983 \times 10^{-4}$ and $g = 7.270 \times 10^{-6}$, was used as a parameterisation [50].

For comparison with ep data, the fit has been reduced by a factor of two to correspond with results from a single e^+e^- hemisphere. A further 8.1% reduction has been made to account for K^0 and Λ decays. The results of the fit are shown

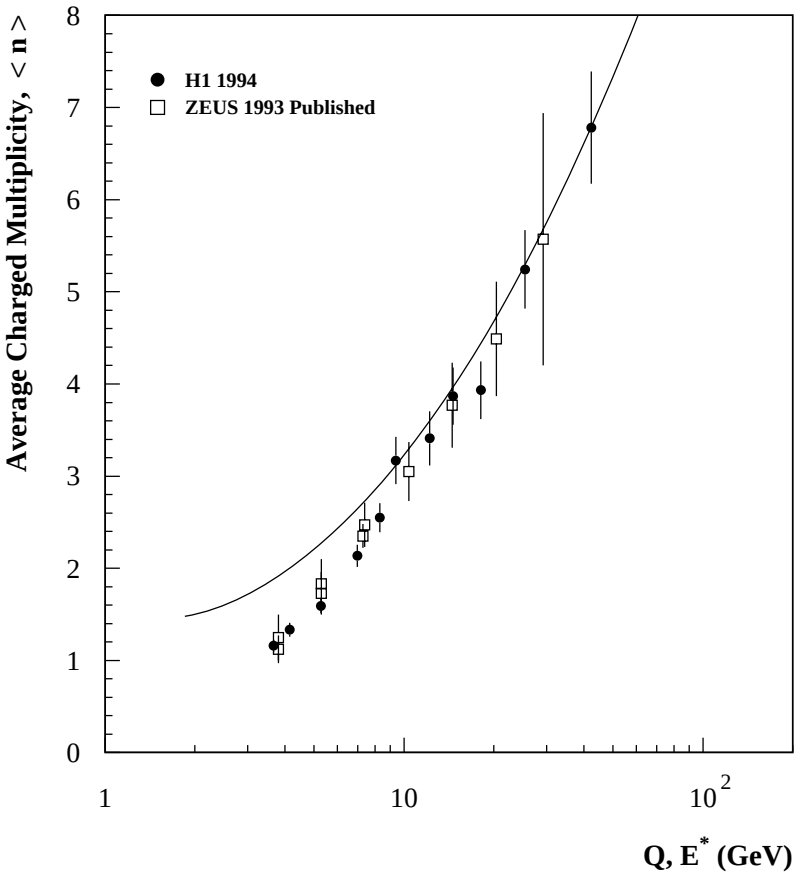

Figure 7.2: *Average charged multiplicity in the current hemisphere of the Breit frame as a function of Q for this analysis (solid circles) and for the ZEUS 1993 analysis (open squares). Statistical and systematic errors from all sources are added in quadrature. The solid line is a fit to many e^+e^- results as a function of the centre of mass energy, E^*.*

in Figure 7.2 (solid line).

There are predictions [54] that not only should the ACM agree with that of e^+e^- experiments but so should its evolution with Q^2. As previous results indicated, although there was very good agreement between H1 and ZEUS [55] analyses and those of e^+e^- at high $Q(E^*)$, the DIS analyses give smaller average charged multiplicities at low values of $Q(E^*)$. The data, even after upward corrections for radiative effects, show this to be a large effect.

In order to investigate this further, we add the four–momenta of all energy clusters in the current region of the Breit frame and plot the resultant total energy, $E_{z<0}$, expressed as a fraction of the event Q, against the corresponding resultant cosine of the Breit frame polar angle, $\cos\Theta_{BF}$. This is shown in Figure 7.3(a,b) for both the low and high Q^2 data samples. From the discussion in the introduction, it is clear that we would expect that QPM interactions *or* events with only final state radiation (i.e. e^+e^- like events) would lie at $(E_{z<0} = Q/2, \cos\Theta_{BF} = -1)$ whereas events with an empty current hemisphere and/or with significant initial state QCD radiation would either not appear on this diagram or be spread away from this point. Both the low and high Q^2 data samples show such clustering.

By using a Monte Carlo (LEPTO 6.5), it is possible to see where QPM, BGF and QCDC events lie on the $\cos\Theta_{BF}$ - $E_{z<0}$ plane at both the generated an reconstructed levels. Figure 7.4 shows the distribution of QPM events, Figure 7.5 shows the distribution of BGF events and Figure 7.6 shows the distribution of QCDC events.

The above results motivate a cut (shown as a solid line in Figure 7.3(a,b) joining the points (-1,0) and (0,0.5) in this plane) to remove extreme low energy and off–axis events. This is termed the Breit frame energy flow selection and produces samples of 11,735 events and 1,005 events at low and high Q^2 respectively which might be thought of as being purer in lowest order events and have average multiplicities closer to those of the equivalent e^+e^- results. The average charged multiplicities using the Breit frame energy flow selection are shown as open circles

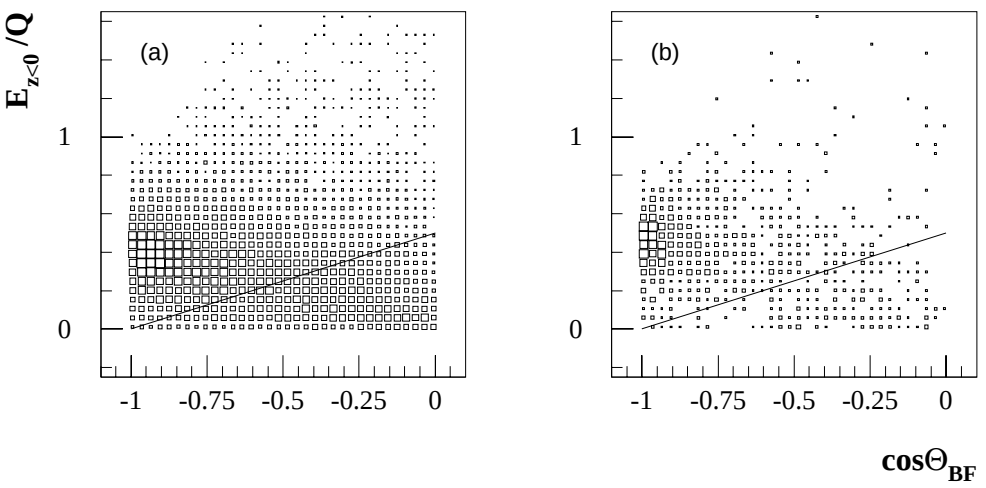

Figure 7.3: *The total energy of the summed calorimeter cluster four–momentum vectors in the current hemisphere of the Breit frame is plotted as a fraction of the event Q against the polar angle of the resultant vector, for (a) the low Q^2 and (b) the high Q^2 data samples. The solid line indicates the Breit frame energy flow selection referred to in the text.*

in Figure 7.7.

7.2.3 Evolution of the Peak position and Width of the Fragmentation Function

When the fragmentation function is plotted as a function of the variable $\xi = \ln(1/x_p)$ the turn-over region is expanded. According to the expectations of the Modified Leading Logarithmic Approximation (MLLA) and Local Parton Hadron Duality (LPHD), $D(\xi)$ is Gaussian in the neighbourhood of the peak [47].

To avoid over-dependence on high momentum (low ξ) and low p_t (high ξ) tracks where most experimental difficulties lie, the fits of this analysis are restricted to the region of ± 1 unit of the dimensionless ξ either side of the mean value. Results of the fits are shown in Figure 7.8 and Figure 7.9.

The evolution of the fragmentation function may then be effectively summarised by the Q, or E^* dependence of the peak and width values as is shown in Fig. 7.10.

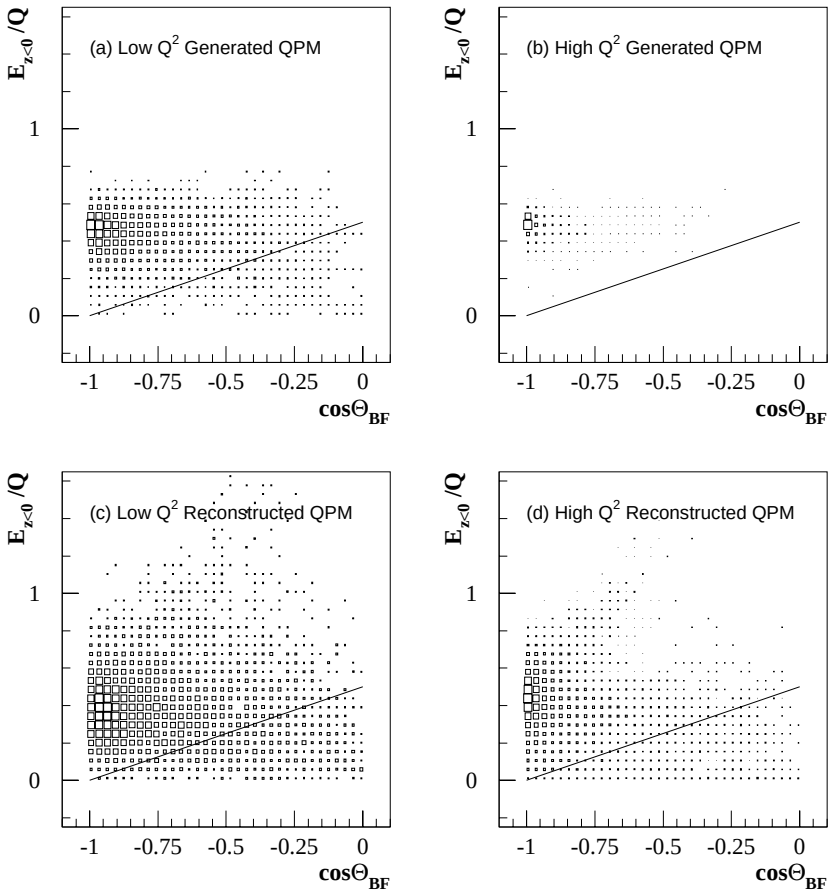

Figure 7.4: *The total energy of the summed generated particle / calorimeter cluster four–momentum vectors in the current hemisphere of the Breit frame is plotted as a fraction of the event Q against the cosine of the polar angle of the resultant vector for QPM events in the LEPTO Monte Carlo at the generated and reconstructed level. The solid line indicates the Breit frame energy flow selection referred to in the text.*

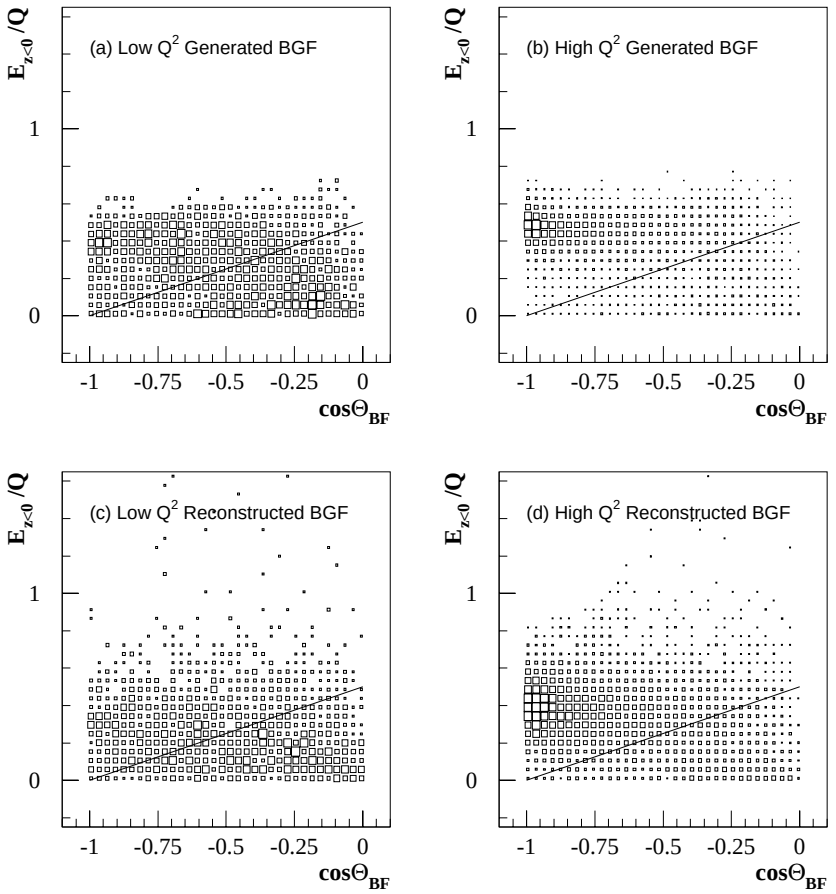

Figure 7.5: *The total energy of the summed generated particle / calorimeter cluster four–momentum vectors in the current hemisphere of the Breit frame is plotted as a fraction of the event Q against the cosine of the polar angle of the resultant vector for BGF events in the LEPTO Monte Carlo at the generated and reconstructed level. The solid line indicates the Breit frame energy flow selection referred to in the text.*

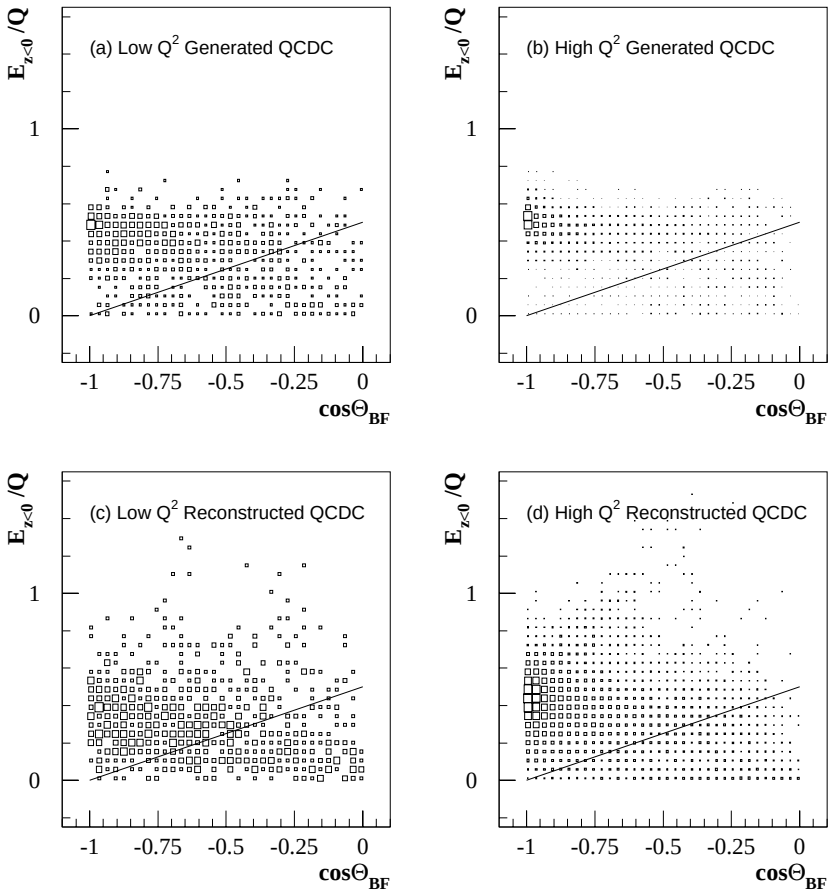

Figure 7.6: *The total energy of the summed generated particle / calorimeter cluster four–momentum vectors in the current hemisphere of the Breit frame is plotted as a fraction of the event Q against the cosine of the polar angle of the resultant vector for QCDC events in the LEPTO Monte Carlo at the generated and reconstructed level. The solid line indicates the Breit frame energy flow selection referred to in the text.*

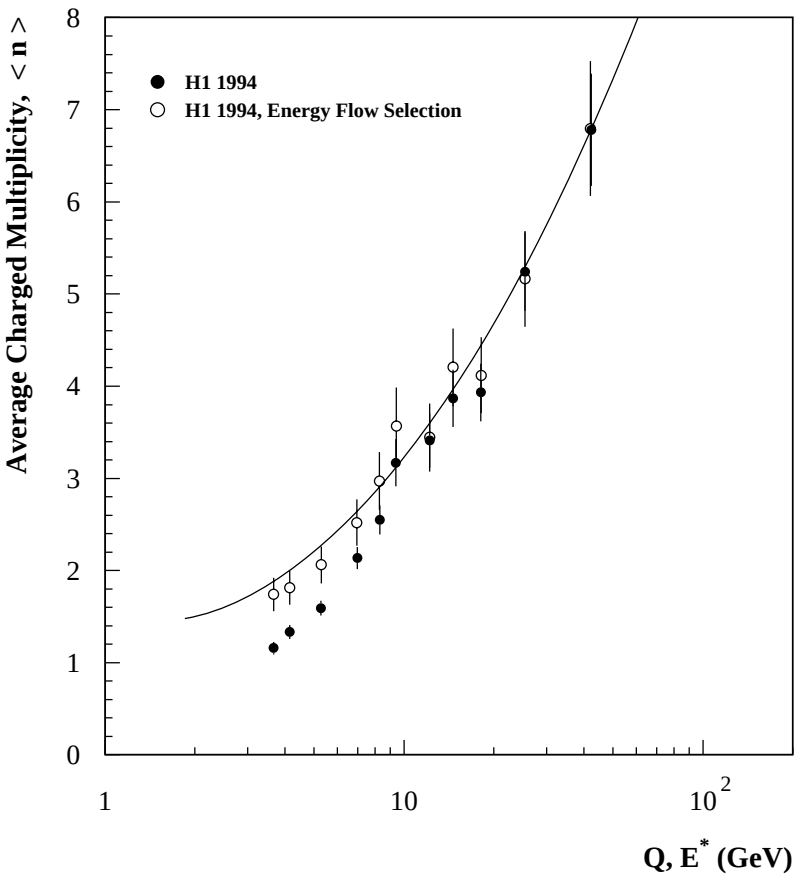

Figure 7.7: *Average charged multiplicity in the current hemisphere of the Breit frame as a function of Q before (solid circles) and after (open circles) the Breit frame energy flow selection.*

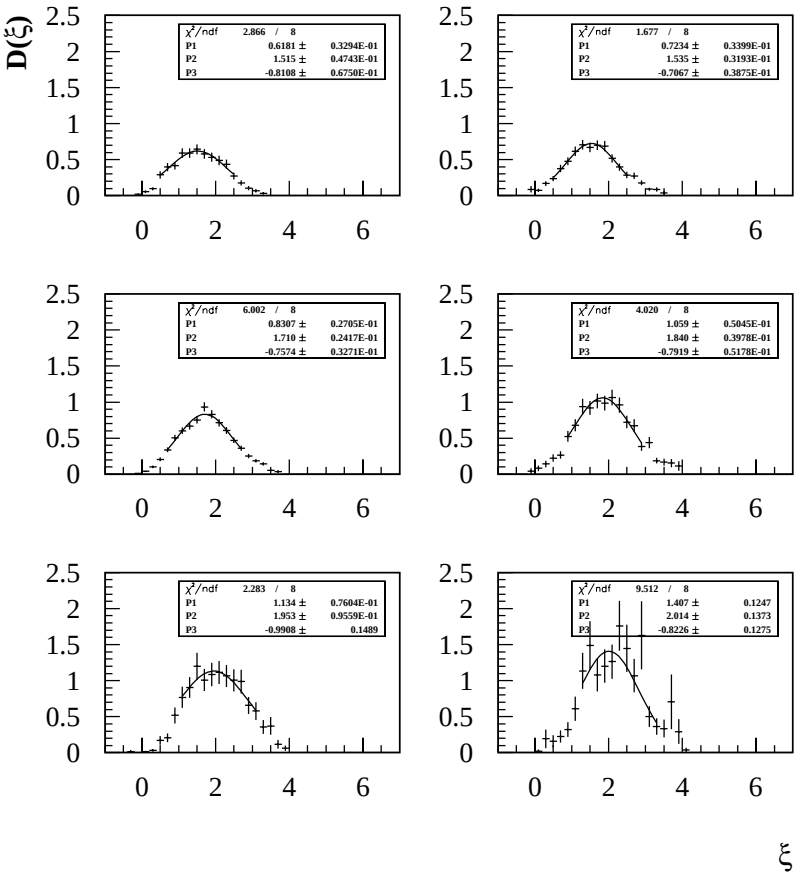

Figure 7.8: *ξ distributions for each Q^2 interval in the low Q^2 data sample. Each distribution has been fitted with a Gaussian over the interval of $\pm$ 1 unit in ξ about the statistical mean.*

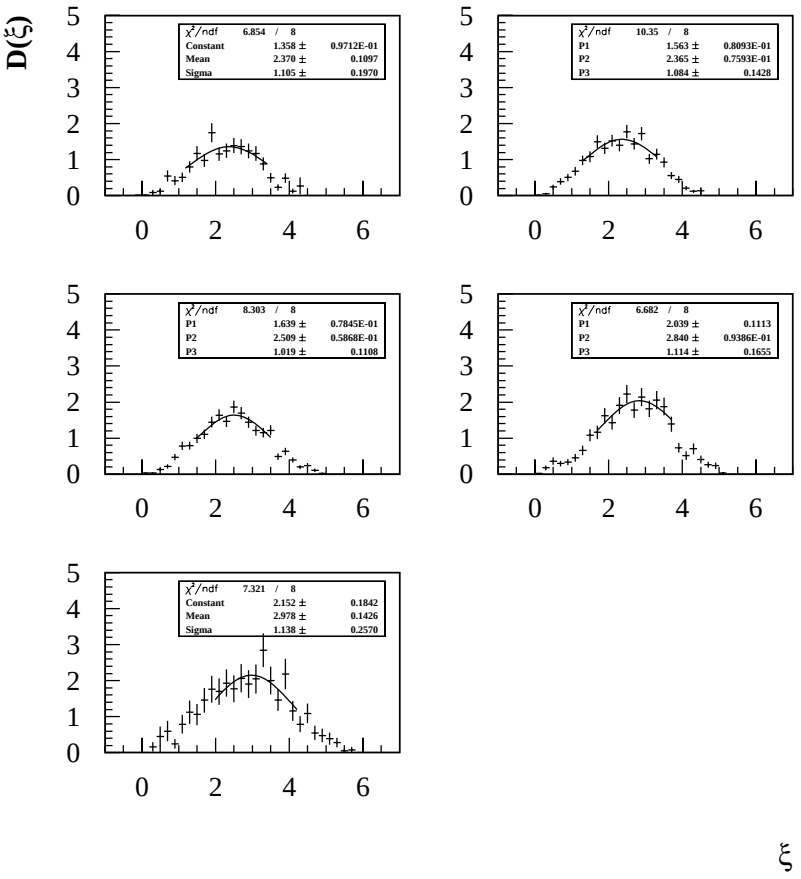

Figure 7.9: *ξ distributions for each Q^2 interval in the high Q^2 data sample. Each distribution has been fitted with a Gaussian over the interval of $\pm$ 1 unit in ξ about the statistical mean.*

The results are compatible with those published earlier [46] which had considerably lower precision, as well as with those of an analysis [55] by the ZEUS collaboration and with various e^+e^- experiments, where the relevant evolution variable is the centre of mass energy, E^*.

With the further assumption of gluon coherence, MLLA/LPHD predicts [47] the dependence of the evolution of the peak and width of the distribution on the dimensionless variable $Y = \ln(Q/2\Lambda_{\mathit{eff}})$, where Λ_{eff} sets the scale of the mass of the final state fragmented hadrons. The prediction gives the peak, ξ_{peak} and the width, ξ_{width}, of the Gaussian approximation to be

$$\xi_{peak} = 0.5Y + c_2\sqrt{Y} + \mathcal{K}$$

$$\xi_{width} = \sqrt{Y^{\frac{3}{2}}/2c_1}$$

where c_1, c_2 are constants dependent only on the number of colours and flavours within QCD and $\mathcal{K}$ contains higher order corrections.

The result of a simultaneous fit to the peak and width values obtained from the H1 1994 data alone is shown as a solid line in Figure 7.10 and yields the values:

$$\Lambda_{\mathit{eff}} = 0.20 \pm 0.02 \text{ GeV}$$

$$\mathcal{K} = -0.43 \pm 0.06$$

with a χ^2/dof of 0.49 in agreement with the values $\Lambda_{\mathit{eff}} = 0.21 \pm 0.02$ GeV and $\mathcal{K} = -0.32 \pm 0.06$ obtained in an analysis [48] of the ξ_{peak} evolution of combined e^+e^- data.

It is interesting to note that using the Breit frame energy flow selection yields insignificant changes to the peak and width of the fragmentation function.

7.3 Comparison to Monte Carlo

As the MLLA fit to both ξ_{peak} and ξ_{width} approximates a straight line, the comparison data/monte-carlo was done by comparing a straight line fit to the monte-carlo

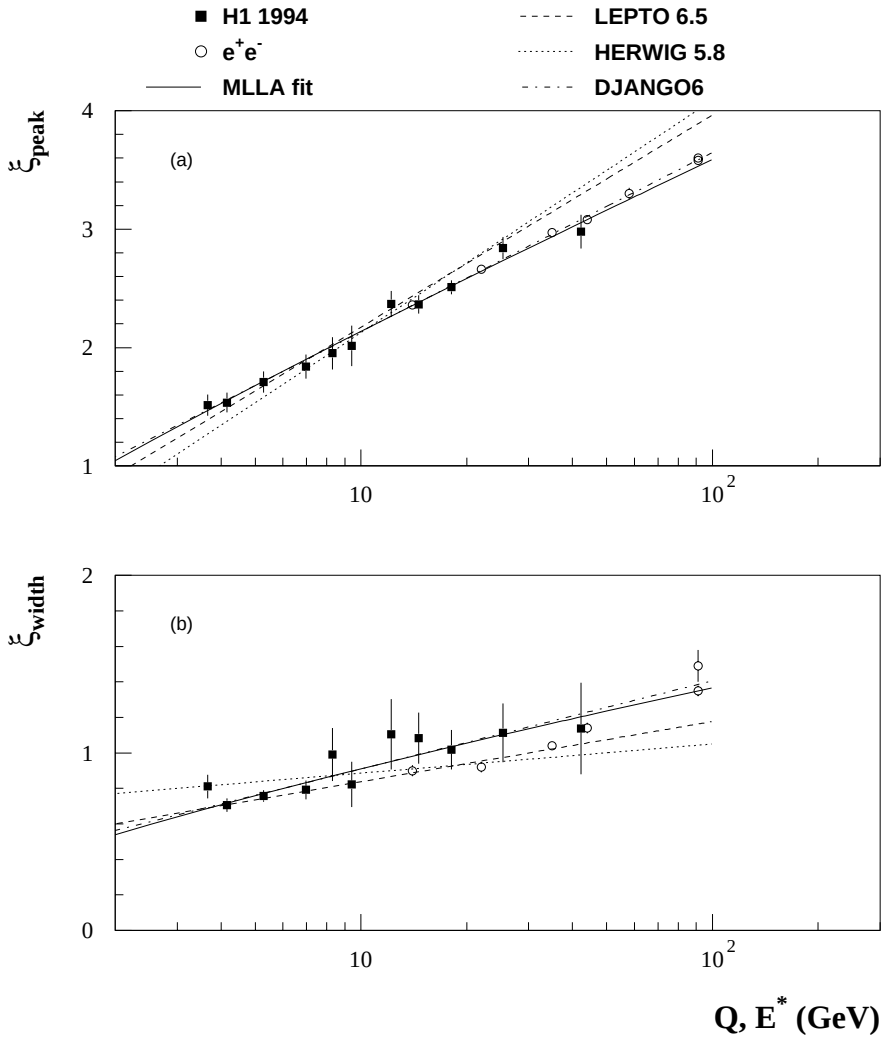

Figure 7.10: *H1 results showing the evolution of (a) the peak and (b) the width of the fragmentation function as a function of Q compared with e^+e^- results (open symbols) as a function of the centre of mass energy, E^*. The solid line is a fit to MLLA expectations.*

Parameter	Number of Flavours			
	2	3	4	5
H1 Fit				
Λ_{eff}	0.21 ± 0.02	0.20 ± 0.02	0.19 ± 0.02	0.17 ± 0.02
$\mathcal{K}$	-0.35 ± 0.06	-0.43 ± 0.06	-0.52 ± 0.07	-0.63 ± 0.07
OPAL Fit				
Λ_{eff}		0.21 ± 0.02		
$\mathcal{K}$		-0.32 ± 0.06		

Table 7.1: *Results of the MLLA fit assuming 3 colours and 2-5 flavours.*

Peak Position				
Dataset	Gradient	Intercept	χ^2/dof	χ^2/dof (data)
H1 1994	0.66 ± 0.04	0.61 ± 0.10	0.40	–
LEPTO 6.5	0.78 ± 0.01	0.38 ± 0.01	1.44	1.77
HERWIG	0.85 ± 0.01	0.16 ± 0.02	3.79	2.96
DJANGO	0.66 ± 0.03	0.62 ± 0.06	0.63	0.41

Table 7.2: *Results of straight line fit to peak positions.*

Width				
Dataset	Gradient	Intercept	χ^2/dof	χ^2/dof (data)
H1 1994	0.20 ± 0.04	0.44 ± 0.07	0.67	–
LEPTO 6.5	0.15 ± 0.01	0.50 ± 0.02	2.47	0.96
HERWIG	0.07 ± 0.01	0.72 ± 0.03	3.12	2.40
DJANGO	0.22 ± 0.05	0.42 ± 0.09	0.41	1.17

Table 7.3: *Results of straight line fit to widths.*

peaks and widths with those obtained from data. The fit was of the form

$$y = a\ln(Q) + c \tag{7.3}$$

The results of the fit (which was done with statistical and systematic errors added in quadrature on the data) for data and monte-carlo are shown in Table 7.2 (peak position) and Table 7.3 (widths). Three different monte-carlos were used in the comparison:

- DJANGO6 [53]. DJANGO simulates deep inelastic lepton proton scattering including both QED and QCD radiative effects. Ariadne [36] was implemented for the QCD cascade. Hadronization is performed using the LUND string model.
- LEPTO 6.5 [9]. LEPTO uses first order QCD matrix elements for gluon radiation and boson-gluon fusion with the QCD cascade treated using parton showers. Hadronization is performed using the LUND string model.
- HERWIG 5.7 [32]. HERWIG implements matrix elements with a parton shower. Hadronization is performed by a cluster hadronization model [39].

It is clear (from both tables and Figure 7.10) that DJANGO6 [53] best describes the data.

7.4 Systematic Uncertainties

The following systematic checks were performed:

- The measured electron energy was varied by altering the electromagnetic scale factors in the BEMC and LAr to investigate the effect of calibration uncertainty.
- Uncertainty in the selection of the Breit frame current hemisphere by selecting $\pm\sigma$ at the reconstructed level of the resolution in $cos\theta_B$.

- Monte Carlo model used for acceptance corrections to the data.
- Size of the Gaussian fitting interval about the mean of ξ.
- Transverse momentum cut on tracks.

7.4.1 Electromagnetic Energy Scale

The measurement of the electron energy directly affects the boost to the Breit frame as the kinematic variables are determined from the scattered electron. The electromagnetic energy scale is known to an accuracy of $\pm 1\%$ in the BEMC and $\pm 3\%$ in the LAr. Scale factors are applied to data in order to test the effects of the uncertainty in the energy measurement. For the low Q^2 sample, there is no change to the peak or width, but there is a 4% change to the multiplicity. For the high Q^2 sample, there is no change to the peak or width, but there is a 7% change to the multiplicity.

7.4.2 Resolution in $cos\theta_B$

The selection of the Breit frame current hemisphere ($cos\theta_B < 0$), was varied by $\pm 1\sigma$ of the resolution in $cos\theta_B$. For both data sets, there was no effect on the peak or the width. The change in the multiplicity was less than 1%.

7.4.3 Data Corrections

By default, the DJANGO Monte Carlo is used with and without initial state QED radiation to obtain the acceptance correction function. As there are no other models which simulate QED radiation available, the systematic uncertainty was obtained by comparing the correction function obtained from a MEPS Monte Carlo with the correction function obtained from a HERWIG Monte Carlo. Both the peak and the multiplicity of the low and high Q^2 samples yielded a 2% uncertainty. There was no effect on the width measurements.

7.4.4 Fitting Interval of ξ

The Gaussian fits to the fragmentation function were varied by fitting to ± 1.2 and ± 1.4 about the statistical mean of $D(\xi)$. The changes to the peak and width are small and have not been included in the systematic error.

7.4.5 Transverse Momentum Cut

The lower limit of the transverse momentum (p_t) of tracks in this analysis was changed from 0.15 GeV to 0.2 GeV. The uncertainty in the peak, width and average charged multiplicity was less than 1% and has not been included in the systematic error.

7.5 Summary

A 1993 analysis [46, 51] of fragmentation functions in the Breit frame of reference has been repeated with the much higher statistics of 1994 data and the two were found to be in good agreement. The 1994 analysis has been expanded to show fragmentation function scaling violations.

Q^2 Range	1/N d$n^{\pm}$/dx_p ($\pm$ stat $\pm$ sys)		
(GeV^2)	$0.02 < x_p < 0.05$	$0.05 < x_p < 0.1$	$0.1 < x_p < 0.2$
12-15	$1.25 \pm 0.36 \pm 0.06$	$2.88 \pm 0.32 \pm 0.16$	$3.61 \pm 0.25 \pm 0.16$
15-20	$1.64 \pm 0.34 \pm 0.07$	$3.44 \pm 0.31 \pm 0.19$	$4.26 \pm 0.26 \pm 0.19$
20-40	$3.02 \pm 0.30 \pm 0.14$	$5.39 \pm 0.30 \pm 0.26$	$5.85 \pm 0.23 \pm 0.26$
40-60	$6.08 \pm 0.73 \pm 0.27$	$9.08 \pm 0.66 \pm 0.32$	$7.07 \pm 0.41 \pm 0.32$
60-80	$9.66 \pm 1.45 \pm 0.43$	$13.31 \pm 1.24 \pm 0.35$	$7.85 \pm 0.65 \pm 0.35$
80-100	$12.76 \pm 2.34 \pm 0.57$	$18.73 \pm 2.48 \pm 0.37$	$8.32 \pm 0.95 \pm 0.37$
100-175	$21.55 \pm 2.25 \pm 1.57$	$20.76 \pm 1.79 \pm 0.64$	$8.71 \pm 0.80 \pm 0.64$
175-250	$26.94 \pm 1.92 \pm 1.97$	$23.27 \pm 1.40 \pm 0.75$	$10.29 \pm 0.65 \pm 0.75$
250-450	$31.16 \pm 1.93 \pm 2.27$	$21.83 \pm 1.21 \pm 0.69$	$9.48 \pm 0.56 \pm 0.69$
450-1000	$51.56 \pm 3.33 \pm 3.76$	$27.00 \pm 1.78 \pm 0.83$	$11.33 \pm 0.84 \pm 0.83$
1000-8000	$72.64 \pm 6.41 \pm 5.30$	$32.40 \pm 3.38 \pm 0.87$	$11.91 \pm 1.50 \pm 0.87$

Table 7.4: *1/N $dn^{\pm}/dx_p$ for the x_p and Q^2 intervals shown.*

Q^2 Range	1/N d$n^{\pm}$/dx_p ($\pm$ stat $\pm$ sys)	
(GeV^2)	$0.2 < x_p < 0.3$	$0.3 < x_p < 0.4$
12-15	$2.53 \pm 0.20 \pm 0.11$	$1.71 \pm 0.17 \pm 0.08$
15-20	$2.89 \pm 0.21 \pm 0.13$	$1.67 \pm 0.16 \pm 0.08$
20-40	$3.00 \pm 0.15 \pm 0.13$	$1.71 \pm 0.12 \pm 0.08$
40-60	$3.84 \pm 0.31 \pm 0.17$	$1.79 \pm 0.20 \pm 0.08$
60-80	$4.94 \pm 0.58 \pm 0.22$	$1.98 \pm 0.33 \pm 0.09$
80-100	$5.60 \pm 0.94 \pm 0.25$	$1.44 \pm 0.37 \pm 0.06$
100-175	$4.66 \pm 0.61 \pm 0.34$	$1.99 \pm 0.45 \pm 0.15$
175-250	$4.12 \pm 0.41 \pm 0.30$	$1.93 \pm 0.30 \pm 0.14$
250-450	$3.76 \pm 0.36 \pm 0.27$	$1.99 \pm 0.26 \pm 0.15$
450-1000	$3.36 \pm 0.42 \pm 0.25$	$1.20 \pm 0.25 \pm 0.09$
1000-8000	$4.16 \pm 0.83 \pm 0.30$	$1.62 \pm 0.55 \pm 0.12$

Table 7.5: *1/N $dn^{\pm}/dx_p$ for the x_p and Q^2 intervals shown.*

Q^2 Range	1/N d$n^{\pm}$/dx_p ($\pm$ stat $\pm$ sys)	
(GeV^2)	$0.4 < x_p < 0.5$	$0.5 < x_p < 0.7$
12-15	$0.92 \pm 0.12 \pm 0.04$	$0.46 \pm 0.06 \pm 0.02$
15-20	$0.96 \pm 0.11 \pm 0.04$	$0.46 \pm 0.06 \pm 0.02$
20-40	$1.03 \pm 0.09 \pm 0.05$	$0.32 \pm 0.03 \pm 0.01$
40-60	$1.11 \pm 0.17 \pm 0.05$	$0.36 \pm 0.07 \pm 0.02$
60-80	$0.70 \pm 0.18 \pm 0.03$	$0.22 \pm 0.06 \pm 0.01$
80-100	$0.61 \pm 0.21 \pm 0.03$	$0.30 \pm 0.11 \pm 0.01$
100-175	$1.30 \pm 0.34 \pm 0.10$	$0.28 \pm 0.11 \pm 0.02$
175-250	$1.04 \pm 0.20 \pm 0.08$	$0.42 \pm 0.10 \pm 0.03$
250-450	$0.90 \pm 0.19 \pm 0.07$	$0.24 \pm 0.06 \pm 0.02$
450-1000	$0.88 \pm 0.23 \pm 0.06$	$0.53 \pm 0.12 \pm 0.04$
1000-8000	$1.19 \pm 0.54 \pm 0.09$	$0.34 \pm 0.15 \pm 0.02$

Table 7.6: *1/N $dn^{\pm}/dx_p$ for the x_p and Q^2 intervals shown.*

Q^2 Interval	No selection	Energy flow selection
(GeV^2)	$< n_{ch} > \pm$ stat $\pm$ sys	$< n_{ch} > \pm$ stat $\pm$ sys
12-15	$1.16 \pm 0.04 \pm 0.05$	$1.74 \pm 0.08 \pm 0.05$
15-20	$1.33 \pm 0.04 \pm 0.06$	$1.81 \pm 0.07 \pm 0.06$
20-15	$1.59 \pm 0.03 \pm 0.07$	$2.06 \pm 0.05 \pm 0.07$
40-15	$2.14 \pm 0.07 \pm 0.10$	$2.52 \pm 0.09 \pm 0.10$
60-15	$2.55 \pm 0.11 \pm 0.11$	$2.97 \pm 0.14 \pm 0.11$
80-100	$3.17 \pm 0.21 \pm 0.14$	$3.57 \pm 0.25 \pm 0.14$
100-175	$3.41 \pm 0.16 \pm 0.25$	$3.44 \pm 0.18 \pm 0.25$
175-250	$3.87 \pm 0.13 \pm 0.28$	$4.21 \pm 0.15 \pm 0.28$
250-450	$3.93 \pm 0.12 \pm 0.29$	$4.12 \pm 0.13 \pm 0.29$
450-1000	$5.24 \pm 0.19 \pm 0.38$	$5.16 \pm 0.19 \pm 0.38$
1000-8000	$6.78 \pm 0.36 \pm 0.49$	$6.80 \pm 0.36 \pm 0.49$

Table 7.7: *Average charged track multiplicity for the Q^2 intervals given with and without the Breit frame energy flow selection. The individual systematic errors have been added in quadrature.*

Data Set	Mean	Width	χ^2/dof
TASSO 14 GeV	2.36 $\pm$ 0.02	0.90 $\pm$ 0.03	4.0/8
TASSO 22 GeV	2.66 $\pm$ 0.02	0.92 $\pm$ 0.03	5.6/8
TASSO 35 GeV	2.97 $\pm$ 0.01	1.04 $\pm$ 0.02	28.6/8
TASSO 44 GeV	3.08 $\pm$ 0.02	1.14 $\pm$ 0.03	12.6/8
OPAL 91 GeV	3.58 $\pm$ 0.01	1.35 $\pm$ 0.03	19.6/17

Table 7.8: *Results of fits done to the TASSO and OPAL data using a simple Gaussian.*

Q^2 Interval	No selection	
(GeV^2)	Peak $\pm$ stat $\pm$ sys	Width $\pm$ stat $\pm$ sys
12-15	$1.52 \pm 0.05 \pm 0.08$	$0.81 \pm 0.07 \pm 0.00$
15-20	$1.53 \pm 0.03 \pm 0.08$	$0.71 \pm 0.04 \pm 0.00$
20-15	$1.71 \pm 0.02 \pm 0.09$	$0.76 \pm 0.03 \pm 0.00$
40-15	$1.84 \pm 0.04 \pm 0.09$	$0.79 \pm 0.05 \pm 0.00$
60-15	$1.95 \pm 0.10 \pm 0.10$	$0.99 \pm 0.15 \pm 0.00$
80-100	$2.01 \pm 0.14 \pm 0.00$	$0.82 \pm 0.13 \pm 0.00$
100-175	$2.37 \pm 0.11 \pm 0.00$	$1.11 \pm 0.20 \pm 0.00$
175-250	$2.36 \pm 0.08 \pm 0.00$	$1.08 \pm 0.14 \pm 0.00$
250-450	$2.51 \pm 0.06 \pm 0.00$	$1.02 \pm 0.11 \pm 0.00$
450-1000	$2.84 \pm 0.09 \pm 0.00$	$1.11 \pm 0.17 \pm 0.00$
1000-8000	$2.98 \pm 0.14 \pm 0.00$	$1.14 \pm 0.26 \pm 0.00$

Table 7.9: *The peak and width of the fragmentation function for the Q^2 intervals given without the Breit frame energy flow selection. The individual systematic errors have been added in quadrature.*

Q^2 Interval	Energy flow selection	
(GeV^2)	Peak $\pm$ stat $\pm$ sys	Width $\pm$ stat $\pm$ sys
12-15	$1.53 \pm 0.06 \pm 0.08$	$0.78 \pm 0.08 \pm 0.00$
15-20	$1.50 \pm 0.03 \pm 0.08$	$0.69 \pm 0.04 \pm 0.00$
20-15	$1.69 \pm 0.03 \pm 0.09$	$0.76 \pm 0.04 \pm 0.00$
40-15	$1.82 \pm 0.04 \pm 0.09$	$0.78 \pm 0.05 \pm 0.00$
60-15	$1.95 \pm 0.09 \pm 0.10$	$0.94 \pm 0.13 \pm 0.00$
80-100	$2.06 \pm 0.08 \pm 0.10$	$0.76 \pm 0.08 \pm 0.00$
100-175	$2.23 \pm 0.17 \pm 0.00$	$1.21 \pm 0.33 \pm 0.00$
175-250	$2.40 \pm 0.08 \pm 0.00$	$1.04 \pm 0.14 \pm 0.00$
250-450	$2.47 \pm 0.07 \pm 0.00$	$1.07 \pm 0.14 \pm 0.00$
450-1000	$2.87 \pm 0.13 \pm 0.00$	$1.23 \pm 0.23 \pm 0.00$
1000-8000	$3.02 \pm 0.46 \pm 0.00$	$2.04 \pm 1.32 \pm 0.00$

Table 7.10: *The peak and width of the fragmentation function for the Q^2 intervals given with the Breit frame energy flow selection. The individual systematic errors have been added in quadrature.*

Chapter 8

Conclusions

Scaled momentum distributions of charged particles in the current hemisphere of the Breit frame have been measured and compared with results from e^+e^- experiments.

The properties of the fragmentation function vary as a function of Q and are close to fragmentation function properties in e^+e^- which vary as a function of $\sqrt{s_{ee}}$.

The average charged multiplicity has been compared to multiplicities from one half the hemisphere of e^+e^- events. The multiplicities agree at high Q^2, with a strong disagreement at low Q^2. The disagreement at low Q^2 is due to the higher order QCD processes (such as BGF) which have no analogue in e^+e^- interactions.

The predicted behaviour of the peak and width of the evolving fragmentation function in the MLLA were used to fit the data. The two free parameters were found to be $\Lambda_{\mathit{eff}} = 0.20 \pm 0.02$ and $\mathcal{K} = -0.43 \pm 0.06$, consistent with the predictions of the MLLA and the assumption of LPHD.

Scaling violations of the *ep* fragmentation function in the current region of the Breit frame were measured and shown to be in good agreement with scaling violations from e^+e^- experiments.

The fragmentation properties of the struck quark in the current hemisphere of

the Breit frame in DIS were found to be very similar to the properties of those pair produced in e^+e^- experiments which provides evidence for the universality of quark fragmentation.

Bibliography

[1] D.H. Perkins, "Introduction to High Energy Physics", Addison-Wesley (1986).

[2] R.N. Cahn and G. Goldhaber, "The Experimental Foundations of Particle Physics", Cambridge University Press (1989) chapter 8.

[3] HERA, A Proposal for a Large Electron Proton Colliding Beam Facility at DESY, DESY HERA 81-10 (1981).

[4] H1 Collaboration, Technical Proposal for the H1 Detector (1986); H1 Collaboration, The H1 Detector at HERA, DESY 93-103 (1993), Updated version: DESY H1-96-01 (1996)

[5] ZEUS Collaboration, The ZEUS Detector, Technical Proposal (1986); ZEUS Collaboration, The ZEUS Detector, Status Report (1989).

[6] HERMES Collaboration, A proposal to measure the spin-dependent structure functions of the neutron and proton at HERA (1990).

[7] W. Hoffmann, 'An Experiment to Study CP Violation in the B System Using an Internal Target at the HERA Proton Ring', DESY-PRC 94/02 (1994).

[8] Proceedings of the Workshop 'Physics at HERA', edited by W.Buchmuller and G. Ingleman, Hamburg, Germany, Vol. 1 (1992).

[9] Proceedings of the Workshop 'Physics at HERA', edited by W.Buchmuller and G. Ingleman, Hamburg, Germany, Vol. 3 (1992).

[10] H1 Collaboration, Track Finding and Fitting in the H1 Forward Track Detector, DESY 95-132 (1995)

[11] T. Ahmed et al., H1 Collaboration, Phys. Lett. B299 (1993) 385.

[12] M. Goldberg, 'Energy Calibration and Reconstruction in BEMC', H1 note H1-05/93-292 (1993).

[13] H. Bethe, and W. Heitler, Proc. Roy. Soc. A146 (1934) 83.

[14] J. Heatherington, ToF - The Time of Flight Device for H1, Thesis submitted to the University of London.

[15] R. J. Ellison, H1 internal note H1-11/90-157, November 1990.
W. J. Haynes, Rutherford Appleton Laboratory preprint RAL-92-048, August 1992.
J. C. Bizot et al., H1 internal note H1-09/92-240, September 1992.
E. Elsen, H1 internal note H1-01/93-262, January 1993.

[16] G. Bernardi et al., Guide to the Simulation Program H1SIM, H1 document.

[17] H. Albrecht et al., H1PHAN - H1 physics analysis programm, H1 document (1991).

[18] S. Egli et at., Guide to the Simulation Program H1SIM, H1 document (1991).

[19] R. Brun et al., GEANT long writeup, CERN Program Library, W5103 (1989).

[20] H1 Collaboration, I. Abt et al., Phys. Lett. 444B (1995) 195.

[21] H1 Collaboration, S. Aid et al., Phys. Lett. 470B (1996) 3.

[22] H1 Collaboration, T. Ahmed et al., Nucl. Phys. 439B (1995) 471.

[23] ZEUS Collaboration, M. Derrick et al., Zeit. Phys. C65 (1995) 379.

[24] Yu.L. Dokshitzer, Sov. Phys. JETP 46 (1997) 641; V.N. Gribov and L.N. Lipatov, Sov. J. Nucl. Phys. 15 (1972) 438, 675; G. Altarelli and G. Parisi, Nucl. Phys. B 126 (1997) 298.

[25] E.A. Kuraev, L.N. Lipatov and V.S Fadin, Sov. Phys. JETP 45 (1977) 199; Y.Y. Balitsky and L.N. Lipatov, Sov. J. Nucl. Phys. 28 (1978) 822.

[26] H1 Collaboration, T. Ahmed et al., Nucl. Phys. 429B (1994) 477.

[27] J. B. Dainton invited talk "Summary Talk", at the IoP Half Day Meeting "New Light on the Pomeron", Imperial College, London, UK, June 1995.

[28] R.P.Feynman, R.D.Field, Nucl. Phys. 136B (1978) 1

[29] Physical Review D (Particles and Fields), 1 July 1996, Part I. Review of Particle Physics.

[30] B.Andersson, G.Gustafson, G.Ingleman and T.Sjöstrand, Phys. Rep. 97 (1983) 31; T.Sjöstrand, Nucl. Phys. 248B (1984) 469; T.Sjöstrand, Computer Phys. Comm. 39 (1986) 347; T.Sjöstrand, and M.Bengtsson, Computer Phys. Comm. 43 (1987) 367.

[31] G.Altarelli and G.Parisi, Nucl. Phys. 126B (1977) 298

[32] G. Marchesini et al., Comput. Phys. Commun. 67 (1989) 13.

[33] G. Gustafson, Phys. Lett. 175B (1986) 453, G. Gustafson, U. Pettersson, Nucl. Phys. 306B (1988) 746, B. Andersson, G. Gustafson, L. Lönnblad, U. Pettersson, Zeit. Phys. C43 (1989) 625, B. Andersson, G. Gustafson, L. Lönnblad, Nucl. Phys. 339B (1990) 393.

[34] OPAL Collaboration, M.Z. Akrawy et al., Zeit. Phys. C47 (1990) 505.

[35] Rapidity gaps and other final state properties in the colour dipole model for deep inelastic scattering, CERN-TH.7307/94, June 1994, submitted to Z. Phys. C.

[36] L. Lönnblad, Comput. Phys. Commun. 71 (1992) 15

[37] T. Sjöstrand, PYTHIA 5.7 and JETSET 7.4 physics and manual, CERN-TH.7112/93, Dec. 1993.

[38] CERN 89-08, Vol. 3 (1989) 159.

[39] B.R. Webber, Nucl. Phys. (1984) 492.

[40] U. Bassler and G. Bernardi, On the Kinematic Reconstruction of Deep Inelestic Scattering at HERA: the Σ Method, DESY 94-231 (1994)

[41] D. Kant, D. Cussans, private communication.

[42] H1 Collaboration, S. Aid et al., Zeit. Phys. C72 (1996) 573.

[43] G. Thompson, D. Kant, Comparing Multiplicities in the Breit frame and the Hadronic CMS, H1 Note, H1-08/95-452, August 29, 1995.

[44] E.J.Weinberg et al., Particles and Fields, Phys. Rev. D54 (1996) 177

[45] K. H. Streng, T. F. Walsh and P.M. Zerwas, Zeit. Phys. C2(1979)237.

[46] H1 Collaboration, S. Aid et al., Nucl. Phys. 445B (1995) 3.

[47] Yu.L. Dokshitzer, V.A. Khoze, A.H. Mueller and S.I. Troyan, "Basics of Perturbative QCD" Editions Frontières (1991); Ya.I. Azimov, Yu.L. Dokshitzer, V.A. Khoze, and S.I. Troyan, Zeit. Phys. C31 (1986) 213, Zeit. Phys. C27 (1985) 65; L.V. Gribov, Yu.L. Dokshitzer, V.A. Khoze, and S.I. Troyan, Phys. Lett. 202B (1988) 276.

[48] OPAL Collaboration, M.Z. Akrawy et al., Phys. Lett. 247B (1990) 617.

[49] OPAL collaboration, P.D. Acton et al., Zeit. Phys. C53 (1992) 539.

[50] D. Kant, private communication.

[51] D. Kant, University of London thesis, also published by the Rutherford Appleton laboratory as RAL-TH-96-008.

[52] TASSO Collaboration, W. Braunschweig et al., Zeit. Phys. C47 (1990) 187, Phys. Lett. 311B (1993) 408; DELPHI Collaboration, P. Abreu et al., Phys. Lett. 311B (1993) 408; OPAL Collaboration, G. Alexander et al., Zeit. Phys. C72 (1996) 191.

[53] G.A. Schuler and H. Spiesberger, Proceedings of the Workshop: Physics at HERA, vol. 3 eds. W. Buchmüller, G. Ingelman, DESY (1992) 1419.

[54] A.Basetto, Nucl. Phys. 202B (1982) 493.

[55] ZEUS Collaboration, M. Derrick et al., Zeit. Phys. C67 (1995) 93.

[56] D. Graudenz, CERN-TH/96-52.

[57] D. Graudenz, CERN-TH/96-155; D. Graudenz, private communication.

[58] R. Baier and K. Fey, Z. Phys. C2 (1979) 339; G. Curci, W. Furmanski and R. Petronzio, Nucl. Phys. B175 (1980) 27.

[59] Scaling Violations of the Proton Structure Function F_2 at Small x, Phys. Lett. B321(1994)161, DESY-93-146.